Title

Integrated Photonic Devices for Spectroscopy and Biosensing

Author

Amin, Md Nafiz

Publication Date

2024

UNIVERSITY OF CALIFORNIA
SANTA CRUZ

INTEGRATED PHOTONIC DEVICES FOR SPECTROSCOPY AND BIOSENSING

A dissertation submitted in partial satisfaction
of the requirements for the degree of

DOCTOR OF PHILOSOPHY

in

ELECTRICAL AND
COMPUTER ENGINEERING

by

Md Nafiz Amin

December 2024

The dissertation of Md Nafiz Amin
is approved:

Professor Holger Schmidt, Chair

Professor Marco Rolandi

Professor Nobuhiko Kobayashi

Peter Biehl

Vice Provost and Dean of Graduate Studies

Table of Contents

List of Figures

List of Tables

Abstract

Md Nafiz Amin

Integrated photonic devices for spectroscopy and biosensing

The past few decades have seen an increasing demand for miniaturized photonic technologies for guiding, manipulating, and analyzing light in various integrated research and commercial applications, such as telecommunications, observational astronomy, and disease diagnostics. Two application areas where photonic integration continues to lead to promising innovations are on-chip single particle biosensors and next generation spectroscopic platforms. On one hand, different integrated photonic technologies have shown great potential in point-of-care biosensing by implementing a variety of sensitive schemes in lab-on-chip platforms. On the other hand, spectral analysis has been crucial to many breakthrough innovations and discoveries, leading to significant advances in developing miniaturized spectroscopy platforms. However, several challenges remain in realizing fully integrated, compact, simple, and cost-effective photonic platforms in both these applications.

In the context of pathogen sensing, liquid-core antiresonant reflecting optical waveguide (LC-ARROW)-based optofluidic biosensor platforms have demonstrated promising capabilities of detecting individual pathogens (e.g. nucleic acids, proteins, virus) from femtoliter sample volumes using different kinds of planar, single or multi-spot photonic excitation waveguides, such as single-mode, Y-split or multi-mode interference (MMI) waveguides. Additionally, the last excitation approach has also

demonstrated multiplexed screening of different pathogens in the same sample using spectrally dependent multi-spot excitation. The planar excitation methods, however, face several limitations, including stable fiber-to-device coupling, spectral dependence of waveguides, and high-quality fabrication requirements. The first part of this thesis discusses the development of two different free-space, fiber-free, top-down excitation schemes. The first scheme involves excitation with a focused beam through a slit pattern milled into an opaque aluminum film covering the top surface of the LC-ARROW channel. Comparable performances for single bead fluorescence detection between this top-down multispot excitation and the planar, MMI waveguide based excitation is observed. This top-down approach also demonstrates encoded, multiplexed fluorescence detection from micro-particles with two lasers. A second top-down illumination scheme that images the spot pattern from a planar Y-split waveguide directly onto the detection device for high-fidelity fluorescence detection is also reported. This approach circumvents the need for an opaque cover and produces a further 2.7× improvement in signal-to-noise ratio compared to the first scheme.

Advancements in integrated photonic spectrometers are just as crucial, offering transformative ideas in fields such as biosensing, astrophotonic integration, and environmental monitoring. The second part of this thesis introduces the idea of an integrated photonic spectrometer based on top-down imaging of an MMI waveguide combined with convolutional neural network (CNN) analysis. By capturing the wavelength-sensitive interference patterns using a top mounted camera and using CNN analysis trained on the spectra generated by known, tunable sources, this spectrometer

achieves highly accurate performances in the visible and near-infrared wavelength ranges. A spectral resolution of 0.05 nm is reported in the near-infrared wavelengths, and accurate narrowband and broadband spectral reconstruction in both spectral ranges are demonstrated. The compact MMI spectrometer's capabilities are further highlighted through a 4x4 arrayed configuration on the same chip, which significantly reduces the data acquisition time and shows the scalability of this approach for simultaneous multi-target observations. A key demonstration of its applications potential is the spectral analysis of the solar spectrum, where the spectrometer successfully reconstructs the solar spectrum based on training for gas dips using a tunable laser. Next, the ongoing efforts of MMI spectrometer integration into the 3 meter Shane telescope in San Jose, California, followed by the discussion of the key challenges and potential way forward is discussed. The last major focus of this work is on improving the spectrometer’s performance in low-light conditions. Enhancing signal detection for sub-nanowatt input power levels reduces the need for expensive photodetectors, especially in applications such as astronomy or molecular spectroscopy. Selective roughening of the waveguide surface via plasma etching can enhance sensitivity and dynamic range of the MMI spectrometers by 15 dB, enabling the analysis of input test light levels as low as 300 picowatts, and also resulting in a measured scattering coefficient of 1.109 cm^{-1} from the etched section. It is also observed that the performance of the MMI spectrometers in such low-light applications improves with the selection of MMI pattern sections with highest pattern variations for imaging. These results highlight the

potential of the MMI spectrometer for high-performance spectroscopy across disciplines.

Acknowledgements

Graduate school is often compared to a marathon, but I prefer to liken it to a long backpacking trip. In a race, the ultimate goal is to win, while the backpacking journey, at least in my mind, is more about the learning experience (often not enjoyable) and figuring out how to get from destination A to B. The most rewarding part is meeting people and gathering valuable lessons and memories along the way. I owe thanks to many individuals who helped me navigate the unknowns and make this research journey possible over the past few years.

First, I extend my deepest gratitude to my Ph.D. supervisor and research mentor, Professor Holger Schmidt. From him, I have learned not only about photonics research but also about professional project management and the discipline required in research. I began this journey as a new student in a new country, with little idea of what lay ahead. Professor Schmidt's unwavering support and belief in my ability to succeed have continuously inspired me to push the boundaries of my research and expand my knowledge along the way.

I would also like to thank the collaborating researchers who contributed significantly to various aspects of my research, whether through active experimentation or insightful suggestions. My thanks to Professor Aaron Hawkins and his research group at BYU for bringing the biosensor and spectrometer devices into the physical world through their fabrication expertise. I'm also grateful to Professor Kevin Bundy and his group for introducing me to the exciting realm of astrophotonics and facilitating our astronomy experiments over the years. Additionally, I am deeply indebted to Dr. Tom Yuzvinsky for his support during challenging times in our research, especially for his expertise with the SEM and AFM machines.

I have had the honor of working with some of the brightest minds and most wonderful individuals in the Applied Optics group throughout my time here. My thanks to Mahmud, Gopi, Jen, Mike, Lexa, and Cassidy for helping me find my footing in research and for teaching me the basics of experiments during my early days. I am also grateful to Vahid, Sampad, Tyler, and Zoe for their assistance, collaboration, and discussions in nearly all of my projects. Special thanks to Sujung, Abir, Ravipa, and Helio for their assistance and sharing many fond memories. I am incredibly thankful to my friends, both here in the United States and back in Bangladesh, for their support, encouragement, and help throughout this journey. Special thanks to Asif, Samir, and Zubayer, who often came through during tough times. I am also grateful to the Bangladeshi student community at UCSC for bringing a little piece of home to me and making my time here more vibrant.

My journey would not have been possible without the love, support and sacrifices of my family. The have always believed in me, standing by me throughout the difficult times. My younger brother, Dhrubo, has been there for our family when I was busy in research. My father and my mother both have made significant professional and personal sacrifices to raise me to the individual I am today. Their unwavering love and support from thousands of miles away still keeps me going. And finally, to the love of my life and my home, Marzia- you have sacrificed so much to be here with me. I owe a part of my journey, and myself, to you.

Chapter 1: Introduction

The manipulation and analysis of light play a critical role in many major scientific discoveries and technological innovations. It enables probing into the fundamental properties of matter, enabling the understanding of the universe from the cosmological scale down to the quantum mechanical scale. Light manipulation also plays a crucial role in biological sciences through fundamental observational techniques like microscopy and fluorescence imaging, as well as by allowing scientists to observe cellular structures and track molecular interactions through spectroscopy. Specifically, since the invention of optical fibers and lasers in the last century, different light-guiding, sensing, and source systems have transformed almost every discipline and commercial industry by improving data transmission, imaging, and precision measurements. Two notable areas of interest in this publication are disease diagnostics and astronomical observations.

The exponential growth of the semiconductor industry over the last few decades has led to tremendous advancements in micro and nanofabrication technologies. In the recent past, the photonics industry has only started to leverage this advancement in high-volume manufacturing, resulting in the era of miniaturized, high-performance active and passive components and integrated photonic circuits (PIC). We have seen the planar waveguides, on-chip lasers, ultra-sensitive photodetectors, and many more photonic concepts realized into scalable technologies. Many of these inventions have already revolutionized data communications and diagnostic applications. The emerging era of artificial intelligence is expected to further enhance the capabilities of integrated photonic elements in terms of design and performance optimization, leading to smarter, faster, and more adaptive novel photonic applications.

There is an ever-growing need to detect pathogens and diagnose potential diseases with reliable precision and sensitivity. Moreover, rapid and low-cost diagnosis schemes are becoming increasingly important in mitigating infectious disease outbreaks. As we have seen during the Covid-19 pandemic, the SARS-Cov-2 virus can transmit easily, spike the lung cells and compromise lung functionalities within a timeframe of hours [1]. Many of the current gold standard techniques, such as amplification-based diagnosis, e.g., RT-PCR, qT-PCR have long processing times, and both techniques are expensive in terms of cost and chemical reagents [2]. On the other side, the most common rapid antigen testing approaches, i.e., enzyme-linked immunoabsorbent assays (ELISAs) [3] or chemiluminescence assays (CLIAs) [4], work only at high enough clinical concentrations.

One key approach to photonic biomedical diagnostic platforms is based on optofluidics [5][6]. It integrates fluidic flow in micro and nano-scale channels with photonic elements on the same chip, thus enabling the interaction of light with different individual pathogen entities, e.g. virus, nucleic acids, protein antibodies at a clinical concentration level. Optofluidic biosensors are a class of diagnostic platforms that offer an answer to many of these problems. By integrating fluidic flow in micro- and nano-scale channels with photonic elements, an optofluidic biosensor enables precise interactions between light and various pathogen entities, such as viruses, nucleic acids, and protein antibodies, even at clinical concentration levels. As discussed in chapter 2, anti-resonant optical waveguide (ARROW) based biosensors have been among the most prominent optofluidic biosensors over the last few years [7]. This technology has enabled light guiding inside a low refractive index liquid-core channel, thus, in turn, enabling the rapid, fluorescence-based detection of nanoscale pathogens using fiber-coupled, planar excitation waveguides. The most significant advantage of such a compact platform will be the ability for low-cost mass fabrication. The silicon-based LC-ARROW devices are fabricated using standard semiconductor microfabrication processes and can be commercially produced while consistently maintaining desired benchmarks. Moreover, multiplexed screening of biomolecules from the same femtoliter sample volume has been demonstrated on the ARROW platform by integrating wavelength-sensitive multi-spot excitation using a multimode interference (MMI) waveguide [8][9]. This approach has really opened the potential pathways to a high-performance differential screening platform to fight future infectious diseases at the early stages of an outbreak.

The first part of this PhD thesis focuses on developing free-space, top-down excitation schemes in the ARROW optofluidic platforms, as discussed in chapter 3. A fiber-coupled planar waveguide excitation makes the practical field application of optofluidic biosensors challenging since all healthcare settings are not expected to have dedicated fiber-coupled, design-specific lasers that require occasional optical maintenance. My top-down design proposes a fiber-free alternative scheme with high detection sensitivity at any excitation wavelength. I also demonstrate a second top-down excitation scheme using simple photonic elements for spatial shaping of the excitation beam. Both approaches can be promising options for integration into more complex lab-on-chip architectures.

Similar to the diversified implementations in medical diagnostics, integrated photonic sensors have shown the potential to develop a new generation of spectrometer platforms [10]. Arguably, optical spectroscopy is one of modern technology's most crucial analysis methods for enabling material characterization for different applications. Almost all traditional benchtop spectrometers available in today's world depend on either of the two fundamental physical phenomena, namely the dispersion of light from a prism or a grating or the interference effect between two beams with slightly different path lengths, as discussed in chapter 4. While effective and high precision, these classical approaches fall short in several demands from today's application needs [11][12]. Because of the inherent path dependence, these technologies are not scalable to chip-scale in a simple format, and arrayed implementation for mass deployment becomes challenging as each spectrometer needs a dedicated detector. The prohibitive cost of these conventional units increases the cost-per-spectrum of most high-precision applications, such as observational astronomy. Considering these limitations, the last decade has seen a drive to develop integrated spectrometers powered by photonic elements [10][13][14]. The delicate wavelength sensitivity of the photonic waveguides also makes them promising candidates for many novel spectroscopic analysis applications, as discussed in chapter 5. In particular, several promising fiber-based or planar-format photonic spectrometers have been demonstrated based on image analysis techniques [15][16]. However, most of these ideas have yet to fully leverage the power of advanced learning algorithms and rely on developing sensitive image calibration systems and very specific photonic design architectures.

Starting in chapter 6, the second part of this thesis focuses on the development of on-chip spectrometers based on planar multi-mode waveguides. This simple photonic element has been extensively used in data communications and biosensing applications to implement wavelength division multiplexing strategy. Here, the extreme wavelength sensitivity of this device is harnessed to perform spectral analysis of an unknown test signal using neural network techniques. High-resolution performance and broadband spectral reconstruction are demonstrated in the visible and near-infrared wavelength ranges. At its very core, this image-to-spectral mapping strategy relies on convolutional neural network-based training strategy, which is laid out in chapter 7. Chapter 8 focuses on proof-of-concept applications of the MMI spectrometers. Arrayed MMI waveguide spectrometer realization is demonstrated, followed by the analysis of the solar spectrum using a small telescope and a tunable laser source. In the near future, the MMI spectrometer aims to be used as an integrated astrophotonic element at the 3-meter Shane Telescope at Lick Observatory, California. The current efforts of this instrumentation project and the key challenges are also highlighted. Observational astronomy is inherently a low-light discipline. As a result, characterization and enhancement of the low-light performance of the MMI spectrometer is of paramount importance. We demonstrate a signal enhancement technique for the spectrometer using plasma etching in chapter 9. It is also observed in this study that available pattern density on certain regions of the MMI waveguide starts to become a crucial factor for low-light applications. In Chapter 10, the conclusion summarizes the key findings and outlines the future prospects for the work presented in this publication. The author hopes that the findings and insights from this work will benefit future research endeavors.

Chapter 2: Background of ultrasensitive detection in ARROW devices

2.1. Optical waveguides

An optical waveguide is a physical structure of two or more materials that can confine and guide light through it, predominantly through the mechanism of total internal reflection (TIR). It is the fundamental building block of many optical communication and sensing systems [17][18]. The simplest form of optical waveguide is a dielectric 2D slab waveguide, and the core properties of waveguide propagation in integrated photonic circuits can be easily explained through it.

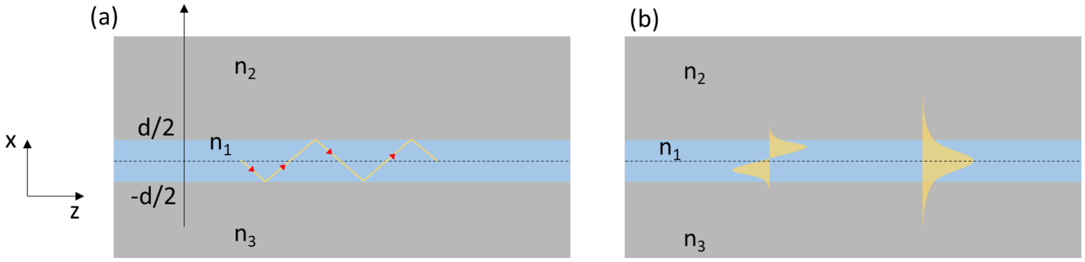

Fig 2.1 (a) Schematic representation of light ray propagation through a 2D asymmetric slab waveguide (b) Field distribution of symmetric m=0 and anti-symmetric m=1 mode inside the waveguide.

Fig. 2.1(a) shows the schematic diagram of an asymmetric three-layer planar waveguide. The refractive index profile of the structure can be described as:

$$\begin{aligned} n(x) &= n_1, \quad |x| < \frac{d}{2} \\ &= n_2, \quad x > d/2 \\ &= n_3, \quad x < -d/2 \end{aligned} \tag{2.1}$$

In order to achieve confined mode propagation by means of TIR, as shown by ray optics propagation in the Fig. 2.1(a), the necessary condition is $n_1 > n_2, n_3$. The case of $n_2 = n_3$ is a symmetric waveguide. The simplest practical example of such a structure would be a thin glass layer immersed in air or any other fluid with a relatively lower index of refraction. For such a combination of isotropic and non-magnetic materials and monochromatic light propagation with a time harmonic variation exp(-iωt), Maxwell's equations in the three layers can be written as:

$$\nabla \times \boldsymbol{H} = -i\omega\epsilon_0 n_i^2 \boldsymbol{E} \tag{2.2}$$

$$\nabla \times \boldsymbol{E} = i\omega\mu\boldsymbol{H} \tag{2.3}$$

$$\nabla . \boldsymbol{E} = 0 \tag{2.4}$$

$$\nabla . \boldsymbol{H} = 0 \tag{2.5}$$

Where n_i is the refractive index in the layer i. By applying the curl operator to equation 2.3, we can substitute the ***H*** field from equation 2.3. Further upon using the vector identity $\nabla\times\nabla\times\boldsymbol{E} = \nabla(\nabla.\boldsymbol{E}) - \nabla^2\boldsymbol{E}$ and using equations 2.2 and 2.4, we finally get:

$$\nabla^2\boldsymbol{E} = -\omega^2\mu\epsilon_0 n_i^2 \boldsymbol{E}$$

$$\text{Or, } \nabla^2\boldsymbol{E} + k_0^2 n_i^2 \boldsymbol{E} = 0 \tag{2.6}$$

Where $k_0 = \omega\sqrt{\mu\epsilon_0} = \frac{\omega}{c}$ is the free-space wave-number. Considering a homogeneous structure along the direction of propagation (z-axis), the solution fields of the above differential equation can be expressed as:

$$\boldsymbol{E}(x,z) = \boldsymbol{E}(x) exp[-i\beta z] \tag{2.7}$$

Here, β is the propagation constant in the z-axis. This allows us to write equation 2.6 as:

$$\frac{d^2\boldsymbol{E}(x)}{dx} + (k_0^2 n_i^2 - \beta^2)\boldsymbol{E}(x) = 0 \tag{2.8}$$

This is known as Hemholtz equation [19]. The eigenvalues from equation 2.8 determine the discrete β values, which can be further expressed as $\beta = k_0 n_{eff}$, where n_{eff} is the effective index of a particular field distribution called a "mode". The propagation constant β or the effective index n_{eff} determines whether the field of a mode has a sinusoidal oscillation or exponential decay in different parts of the waveguide. The field amplitude of the guided modes are sustained within the core region (n_1) and fall off exponentially in the claddings (n_2, n_3), i.e. β must follow the following condition:

$$\frac{n_2\omega}{c}, \frac{n_3\omega}{c} < \beta < \frac{n_1\omega}{c} \tag{2.9}$$

$$\text{Or, } n_2, n_3 < n_{eff} < n_1 \tag{2.10}$$

The field distributions $\boldsymbol{E}_m(x)$ and $\boldsymbol{H}_m(x)$ inside a slab waveguide are the eigenvectors of equation 2.8 corresponding to each β (n_{eff}), where m=0,1,2… is the mode number. Each mode can be expressed as a superposition of Transverse Electric (TE) or Transverse Magnetic (TM) polarized fields. A TE-polarized field is perpendicular to the light ray's plane-of-incidence (here the xz plane) and has only the field components $\boldsymbol{E}_y(x)$, $\boldsymbol{H}_x(x)$, and $\boldsymbol{H}_z(x)$. Similarly, a TM-polarized field only has $\boldsymbol{H}_y(x)$, $\boldsymbol{E}_x(x)$, and $\boldsymbol{E}_z(x)$. If we consider a TE mode as an example, the tangential component of the $\boldsymbol{E}_y$ and $\boldsymbol{H}_z$ must be continuous at the material interfaces to be an acceptable field solution.

Implementing these boundary conditions, the electric field $\boldsymbol{E}_{m,y}(x)$ for the m-th TE mode can be expressed by the set of equations [20]:

$$\begin{aligned} \boldsymbol{E}_{m,y}(x) &= C\left[\cos hx - \tfrac{q}{h}\sin hx\right], \quad |x| \le {}^{d}/_{2} \\ &= C\, exp\left(-q(x - {}^{d}/_{2})\right), \qquad x > {}^{d}/_{2} \qquad (2.11) \\ &= C\left[\cos h\tfrac{d}{2} + \tfrac{q}{h}\sin h\tfrac{d}{2}\right] exp\left(p(x + {}^{d}/_{2})\right), \quad x < -{}^{d}/_{2} \end{aligned}$$

Here, $h = \sqrt{n_1^2\frac{\omega}{c} - \beta^2}$, $q = \sqrt{\beta^2 - n_2^2\frac{\omega}{c}}$, and $p = \sqrt{\beta^2 - n_3^2\frac{\omega}{c}}$. Fig. 2.1(b) shows the electric field profiles of the TE_0 and TE_1 modes inside the structure. Furthermore, by equating the $\boldsymbol{E}_y$ and $\boldsymbol{H}_z$ fields at the boundary regions x=d/2 and x= -d/2, we can write:

$$\tan hd = \frac{h(p+q)}{h^2 - pq} \qquad (2.12)$$

This is the eigenvalue equation for the TE modes and lets us directly calculate the effective indices of the different symmetric and anti-symmetric orthogonal modes

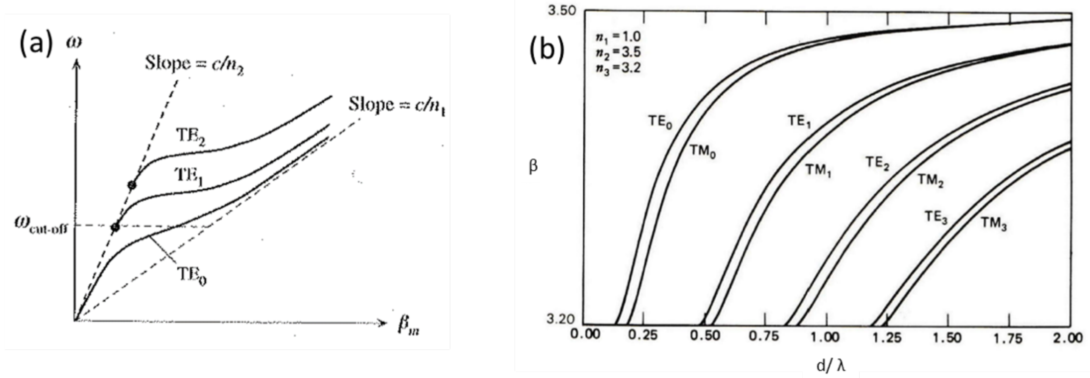

Fig 2.2 (a) Dispersion diagram, ω vs. β of a symmetric slab waveguide (n_2= n_3) for different TE modes. Each propagating mode stops being a confined, guided mode below a certain cut-off frequency (wavelength), after which it becomes leaky (adapted from [21], (b) β vs. d/ λ for the confined modes of GaAs film on AlGaAs substrate (adapted from [22]).

based on the wavelength (frequency) of light, refractive indices in the structure, and the core thickness. The allowed values of β (n_{eff}) can be found from equation 2.12 using graphical or numerical methods. These calculated values can then be used to obtain the modal field in each layer using equation 2.11. For the TM modes, a similar equation as 2.12 to find the propagation constant of the guided modes can be derived by replacing p and q with $\bar{p} = \frac{n_1^2}{n_3^2} p$ and $\bar{q} = \frac{n_1^2}{n_2^2} q$, respectively. Fig. 2.2(a) shows a dispersion relation ω (or λ) vs. β_m for different TE modes inside a symmetric slab waveguide ($n_2 = n_3$) [21]. The light lines with slopes c/n_1 and c/n_2 defines the bounding region for the propagation constant β_m of a confined mode, while each mode (β_m) stops propagating below a certain cut-off frequency $\omega_{cut\text{-}off}$. The value of a propagation constant β also depends on the waveguide thickness. As an example, Fig. 2.2(b) illustrates the change of β for different low-order TE and TM modes for different waveguide thickness d/λ for a thin-film asymmetric slab waveguide with air/GaAs/AlGaAs structure [22]. As evident from Fig. 2.2(b), for a fixed wavelength a waveguide mode only becomes confined above a certain cut-off value of d/λ. At the cut-off thickness for a particular mode β_m, $p = 0$ and $\beta = n_3 \, {}^{\omega}/_{c}$, i.e. the mode spreads to $x = -\infty$ within the substrate. The cut-off thickness d/λ for the TE and TM modes, respectively can be calculated by using the expressions for h, p, and q into equation 2.12 and its TM counterpart, which gives us:

$$\left(\frac{d}{\lambda}\right)_{TE} = \frac{1}{2\pi\sqrt{n_1^2 - n_3^2}}\left[m\pi + \tan^{-1}\left(\frac{n_3^2 - n_2^2}{n_1^2 - n_3^2}\right)^{1/2}\right] \qquad (2.13)$$

$$\left(\frac{d}{\lambda}\right)_{TM} = \frac{1}{2\pi\sqrt{n_1^2 - n_3^2}}\left[m\pi + \tan^{-1}\frac{n_1^2}{n_2^2}\left(\frac{n_3^2 - n_2^2}{n_1^2 - n_3^2}\right)^{1/2}\right] \qquad (2.14)$$

As an example, for an air/SiO_2/SiO_2 rib waveguide with refractive indices n_1= 1.51, n_2=1.00, n_3=1.448, the cut-off thickness at λ=632.8 nm for m=0 fundamental TE mode is d= 175.6 nm. The next mode, m=1 starts to show up at thickness d= 914 nm, defining the single-mode waveguide thickness for this platform. These wavelength-dependent single-mode operation across the visible and NIR wavelengths formulates the core design and operational principles of the single-mode and MMI waveguides on optofluidic biosensor platforms and integrated spectrometers, as described in the later sections, and also in chapter 6.

2.2. Lab-on-a-chip optofluidics for disease biomarkers

The detection of biological entities in the precious volume of a biological fluid sample can be a challenging problem, mainly due to their small size and the presence of a variety of different similar-sized entities [23][24]. Moreover, sensitive detection at an early stage of diagnosis can be particularly difficult because of the low concentration levels of target pathogens [25]. Another challenge is the scalability of the diagnostic platform, which has been a significant concern during the recent Covid-19 global pandemic and can be a major driving factor for the cost of diagnostics [26]. Lab-on-a-chip (LOC) platforms have proven to be one of the most effective approaches for time and cost-effective diagnostics through miniaturization and advanced instrumentation [27][28][29]. One of the most promising LOC technologies is microfluidics, a powerful channel flow-based single-particle analysis assay for detecting individual bioparticles and probing the complex behavior of large biomolecules [30][31]. Integrating multiple functions required for on-chip sample preparation and handling, different microfluidic techniques, e.g., droplet fluidics [32][33], paper-based microfluidics [34], lab-on-a-disk devices [35] can be effective ways to detect and/or manipulate bioparticles for rapid and accurate results. Two major rapidly advancing fabrication technologies, semiconductor fabrication on silicon wafers [36][37][38] and soft polydimethylsiloxane (PDMS) lithography [39][40][41] have enabled quick, low-cost prototyping of different integrated point-of-care platforms.

In the recent years, optofluidic biosensors have achieved significant progress in the development of compact, ultrasensitive LOC platforms for fluorescence-based detection and biochemical analysis of pathogens by combining optics and microfluidics on the same integrated platform [5][42] [43]. Using the interaction of light and individual biomolecules in a small, femto-liter (fL) volume, optofluidic biosensor devices can detect very small disease biomarkers, e.g., DNA, RNA, protein antigens, single viruses from a small sample volume [8] [44] [45]. Moreover, the integration of different passive and active optical components on a biosensing chip opens exciting possibilities for portable, multi-functional detection schemes [46]. From a fundamental design standpoint, the centerpiece of an optofluidic chip is a hollow-core analyte channel that simultaneously works as a liquid-core waveguide to guide the fluorescence signal out of the chip. Most conventional solid-core optical waveguides work based on TIR guiding in a core with a higher refractive index compared to the cladding, as discussed in the previous section. As water (n=1.33) is the primary content in most biofluid samples, TIR is difficult to achieve inside a liquid core-solid cladding waveguide, as most conventional solid materials have higher refractive indices. A few novel ideas have been tried to achieve TIR in a liquid core waveguide, such as solid claddings with low index polymers (Teflon), porous cladding, liquid core-liquid cladding waveguide, each of which comes with their own fabrication and practical application challenges [47].

Light guiding inside a liquid core waveguide can be achieved using another approach named leaky photonic bandgap guiding within a layered medium, or in a special case, through a periodic medium. In a conventional TIR case, the guided light experiences Fresnel reflection from a single dielectric interface where the refractive index is discontinuous. A layered medium may be considered as an array of such dielectric interfaces, where it is possible to achieve extremely high confinement inside the core by the interference of many reflecting waves, even though a single reflection from an individual interface is feeble. Examples of periodic structures could be Bragg waveguides [48] or photonic crystal waveguides [49]. Antiresonant reflecting optical waveguides (ARROWs) also operate based on multilayer thin-film interference principle similar to a Bragg waveguide. However they do not require the cladding layers to be periodic [47][50]. The ARROW layers can be fabricated using common CMOS fabrication techniques [51]. As a result, they are easily integrable into fully planar optofluidic device architecture. So far, different implementations of planar optofluidic biosensors on ARROW platforms has demonstrated single bioparticle detection for different bioassays with high sensitivity [52][53][53][54]. Before further discussing the integration of ARROW as a building block for optofluidic biosensors, the basic guiding principles of ARROW layers is discussed in more detail in the next section.

2.3. ARROW (anti-resonant reflecting optical waveguide)

In an ARROW waveguide, the low-index core is sandwiched between multilayer thin-film stacks, which are designed to act as Fabry-Perot etalons in anti-resonant condition. Fig. 2.3 illustrates a simple ARROW waveguide cross-sectional plane parallel to the direction of light propagation, with a core layer with thickness d_c and refractive index n_c. The multilayer cladding consists of two layers of alternating materials with thicknesses t_1, t_2 and refractive indices n_1, n_2, respectively. We select the materials for different regions such that $n_1 > n_2 > n_c$.After a round-trip, the total transverse phase shift of a propagating light ray through the core region should be an integer multiple of 2π, i.e.:

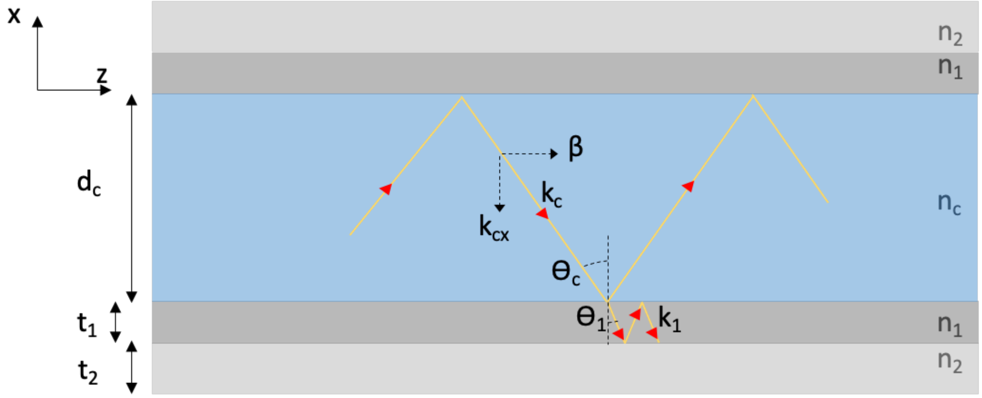

Fig 2.3 ARROW structure cross-sectional overview.

$$2k_{cx}d_c + \emptyset_1 + \emptyset_1 = 2N\pi, \quad \text{N= 0, 1, 2…} \qquad (2.15)$$

Here, $\emptyset_1$ and $\emptyset_2$ are the phase shifts from the reflections of the propagating ray with an angle of incidence θ_c at the two boundaries of the core region. For a TE wave, $\emptyset_1 = \emptyset_2 = 0$, while for a TM wave, both can be 0 (θ_c<Brewster angle) or π (θ_c>Brewster angle). Therefore, equation 2.15 can be written as:

$$2n_c.\frac{2\pi}{\lambda}d_c \cos\theta_c = 2\pi$$

$$\text{Or, } \cos\theta_c = \frac{\lambda}{2n_c d_c} \qquad (2.16)$$

Part of the light in the core region is refracted into the first cladding layer. At the boundary between the core and the first cladding layer, from Snell's law of refraction:

$$\sin\theta_1 = \frac{n_c \sin\theta_c}{n_1} \qquad (2.17)$$

To prevent the transmission of light through the first cladding layer, the light rays in this layer should destructively interfere, i.e. the total transverse phase shift in this layer should be an odd multiple of π. The anti-resonant condition of this layer can be written as:

$$2k_{1x}t_1 + \Psi_1 + \Psi_2 = (2N-1)\pi, \quad \text{N= 0, 1, 2…} \qquad (2.18)$$

Here, k_{1x} is the transverse component of the wave-vector in the first cladding layer and Ψ_1, Ψ_2 are the phase shifts at the two interfaces. Since $n_1 > n_2, n_c$, the total phase shift $\Psi_1 + \Psi_2$ = 2π. Therefore, equation 2.18 can be expressed as:

$$2k_1t_1\cos\theta_1 = (2N-1)\pi, \quad \text{N= 0, 1, 2…} \qquad (2.19)$$

Using equations 2.16 and 2.17 to replace $\cos\theta_1$ in the above equation and using $k_1 = \frac{2\pi}{\lambda}n_1$, the thickness t_1 can be calculated as:

$$t_1 = \frac{(2N-1)\lambda}{4\sqrt{n_1^2-n_c^2+\frac{\lambda}{4d_c^2}}} \tag{2.20}$$

For a large core ($d_c \gg \lambda$), we can approximate $n_1^2 - n_2^2 \gg \frac{\lambda}{4d_c^2}$. Therefore, equation 2.20 can be approximated as:

$$t_1 = \frac{(2N-1)\lambda}{4\sqrt{n_1^2-n_c^2}} \tag{2.21}$$

Similar derivation can be shown for the thickness of the second cladding layer. For a design wavelength λ_D, the general formula to calculate the cladding layers thicknesses in the ARROW waveguide can be written as:

$$t_i = \frac{(2N-1)\lambda_D}{4\sqrt{n_i^2-n_c^2+\frac{\lambda_D}{4d_c^2}}}, \quad \text{i= 1, 2…} \tag{2.22}$$

The liquid-core ARROW waveguides used in the optofluidic biosensor devices in the subsequent sections have d_c= 5 µm, n_c= 1.33, n_1= 2.107 (Ta_2O_5), and n_2= 1.47 (SiO_2), which gives out the thicknesses t_1= 97 nm and t_2= 251 nm for a design wavelength λ_D = 633 nm. It can be shown that the loss characteristics of such a leaky propagation depends on the number of ARROW layers N and the polarization of light, given by [55]:

$$\alpha_{TE,min} = \left(\frac{n_2^2-n_c^2}{n_1^2-n_c^2}\right)^{N/2} \alpha_0,$$

$$\alpha_{TM,min} = \left(\frac{n_1}{n_2}\right)^{2N} \frac{n_1^2}{n_c^2} \alpha_{TE,min}, \qquad (2.23)$$

$$\alpha_0 = \frac{\lambda_D^2 (m+1)^2}{n_c d_c^3 \sqrt{n_1^2 - n_c^2}}$$

where m is the order of the propagating mode. In the next section, we discuss the principle of fluorescence detection from individual micro or nano-scale particles and fluorescence dye molecules on different ARROW-based optofluidic biosensor architectures.

2.4. Particle detection using planar excitation on ARROW devices

In an ARROW-based optofluidic sensing platform, the basic principle is to create fluorescence excitation volumes inside the liquid core ARROW waveguide fabricated

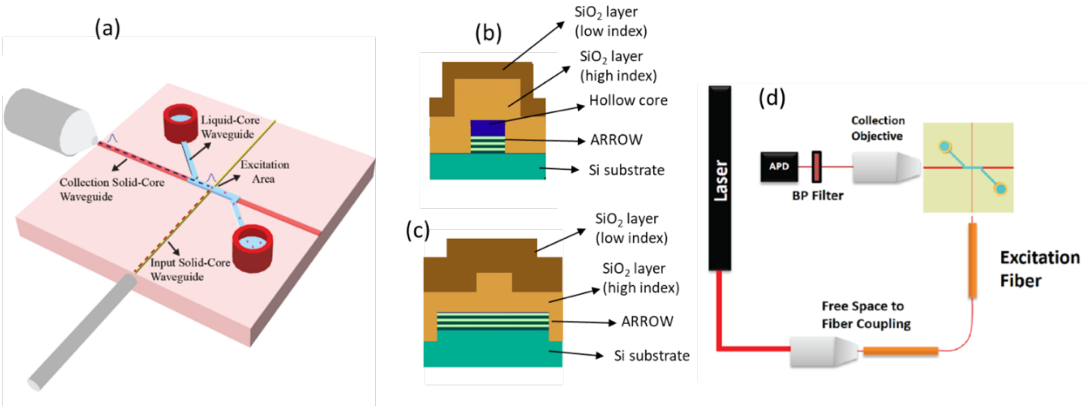

Fig 2.4 (a) Schematic of an early version of ARROW optofluidic chip with orthogonal, single-spot excitation projected onto the liquid core waveguide. The two ends of the liquid core are coupled to solid-core collection waveguides, which collects and carries the fluorescence signal to the edge of the device. (b), (c) Cross-section structures of buried-ridge waveguide designs of liquid core and solid core excitation waveguides on ARROW layers, respectively. (d) A simple experimental setup for fluorescence detection from the optofluidic chip (adapted from [55]).

on a silicon wafer platform. This is done by creating a planar, solid-core waveguide on the same chip which can couple light into the liquid core waveguide, either on the same axis, or in an orthogonal fashion. Fluorescently tagged particles suspended in a liquid medium passes through this excitation volume, and the optical signal generated by these targets couples from the liquid core waveguide into another solid core collection waveguide

In the early stages of the optofluidic chip development, the architecture contained a liquid-core channel, an excitation and a collection waveguide, all on the same axis [56]. This device was able to successfully detect ~490 individual molecules of Alexa 647 dye in an ethylene glycol solution [57]. Later on, an orthogonal architecture was adopted, where an excitation single-mode waveguide lies perpendicular to the liquid core waveguide and the collection waveguide. This architecture is illustrated in Fig. 2.4(a). In this way, the excitation volume at the intersection between the liquid channel and the excitation waveguide came down to femtoliter level. This enabled the sensitive and efficient detection and distinction of single bioparticles in the liquid flow, which follows a Poisson statistical probabilistic distribution inside this excitation volume [58]. Notably, with this early orthogonal design, optofluidic detection of single fluorescently labeled liposomes was reported [52].

The fabrication of an ARROW optofluidic chip follows standard semiconductor fabrication steps [59]. After the plasma enhanced chemical vapor deposition (PECVD) of six Ta_2O_5 and SiO_2 ARROW layers with the design specifications described in section 2.3, a 12 wide and 5 μm tall sacrificial core for the liquid channel was developed using standard SU-8 lithography, followed by the creation of a silicon pedestal for the hollow core using deep reactive ion etching (DRIE) [50][60]. A 6 μm SiO_2 (n=1.51) layer was PECVD grown on this structure to create the shell of the hollow core channel as well the solid-core waveguides in the same fabrication steps. After a second SU-8 lithography step, the 4 μm wide excitation ridge waveguide was created using a selective DRIE step. Finally, the sacrificial core inside the hollow core channel was removed using piranha (H_2SO_4:H_2O_2) etching. In the later designs, a second 6 μm SiO_2 layer (n=1.448) was deposited on top of the first layer to improve the single-mode condition of the excitation waveguide, and make it more durable by reducing water absorption into the core oxide [61][62]. The cross-section of the liquid core and solid-core excitation waveguides on the same ARROW platform with this buried ridge design is shown in Fig. 2.4 (b-c).

The basic experimental setup for fluorescence detection is shown in Fig. 2.4(d). A monochromatic laser source is coupled into a single-mode fiber, which is then butt-coupled into the single-mode excitation waveguide. The choice of the excitation laser wavelength is related to the fluorescent target's excitation and emission spectra. However, in more advanced excitation waveguide designs, such as a multi-mode interference waveguide (discussed in section 2.4.1), it also depends on the excitation waveguide parameters. The fluorescence signal generated by the individual targets couple from the liquid-core waveguide into the collection core waveguide. This is then collected from the collection waveguide facet using an objective lens (NA 0.85, 60x). After passing through a spectral filter that blocks the excitation laser wavelength, the

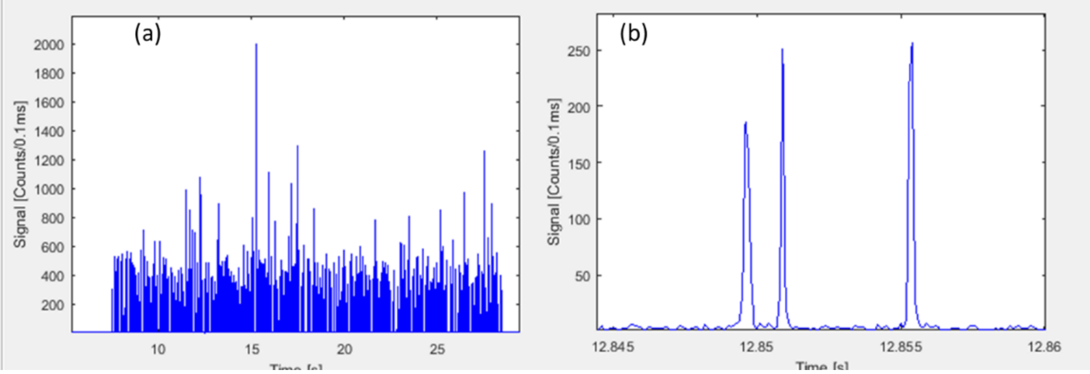

Fig 2.5 (a) Fluorescence signal collected from an optofluidic device sensing experiment by exciting 200 nm fluorescence beads at a sample concentration 1 x 10^7 particles/mL using 633 nm laser light excitation through a single mode-waveguide (b) closer look at the individual signals using a single-mode excitation waveguide.

fluorescence signal is coupled into a larger multi-mode fiber. The fiber delivers the signal into a single photon avalanche diode module (SPCM-AQR-14-FC, Excelitas), which records the arrival time of each photon using a time-correlated single photon counting PCI board (TimeHarp260, Picoquant). The photon timestamps are binned to create a photon count vs. time trace, as shown in Fig. 2.5 (a). Each event (spike) in this trace corresponds to a fluorescently tagged particle.

For excitation using single-mode excitation waveguide, each signal appears to be a single Gaussian peak as seen from the zoomed-in view in Fig. 2.5(b). However, the most matured version of planar optofluidic biosensors incorporated a multi-spot excitation on the liquid channel using a multi-mode interference (MMI) or Y-splitter waveguide, which is discussed in the following section, which would also change the temporal shape of the individual signals.

2.4.1. Multi-spot planar excitation

It has been shown that a multi-spot excitation approach in optofluidic devices enhanced the signal-to-noise ratio (SNR) of the fluorescence detection, ultimately increasing the sensitivity and accuracy of the device [63]. To this end, different integrated multi-spot excitation architectures have successfully demonstrated amplification-free detection of individual biomarkers from a clinically relevant concentration [8][63]. The most notable to mention is the multi-mode interference (MMI) waveguide, a wide planar structure that can support many propagating modes for a chosen wavelength of light. It is commonly used as a passive power-splitting component used in optical communications [64] [65]. As discussed later, in the context of optofluidic biosensing, the MMIs have been popularly used for ultrasensitive detection of different pathogens. Furthermore, the ability to perform simultaneous, multiplexed spectral detection of different pathogen entities using the same excitation volume makes it a powerful biosensing tool.

A brief discussion of the working principle and the design principle of the MMI waveguides for optofluidic biosensor operation is given in this section. In chapter 6, the theory of MMI waveguide propagation will be treated in more detail as a core component of an on-chip integrated spectrometer. When a wide MMI waveguide with width W and length L is coupled with a single mode waveguide, the mode inside the single mode waveguide for a wavelength λ couples into multiple lateral modes in the MMI section. From the ray optics treatment of mode propagation, it can be shown that the maximum number of supported modes m in the MMI section can be calculated using the V-number defined by [21]:

$$V = \frac{W\pi}{\lambda}\sqrt{\left(n_{core}^2 - n_{cladding}^2\right)} \qquad (2.24)$$

$$m \leq (2V - \emptyset)/\pi \qquad (2.25)$$

Here, n_{core} and $n_{cladding}$ are the core and cladding material refractive indices of the MMI waveguide, respectively, and $\emptyset$ is the phase difference acquired at the boundary of the waveguide. These propagating modes interferes with each other to generate wavelength-dependent interference pattern along the waveguide length with multiple self-imaging spots of the input profile at certain distances, as shown in Fig. 2.6(a) [66]. If a liquid core optofluidic channel is placed at this calculated distance from the start of the MMI, this distinct multi-spot excitation pattern can be used to excite the fluorescently tagged particles. The effective width of these mode profiles W_{eff}, also known as the effective waveguide width which takes into account the polarization-dependent lateral penetration depth of the mode fields can be expressed as:

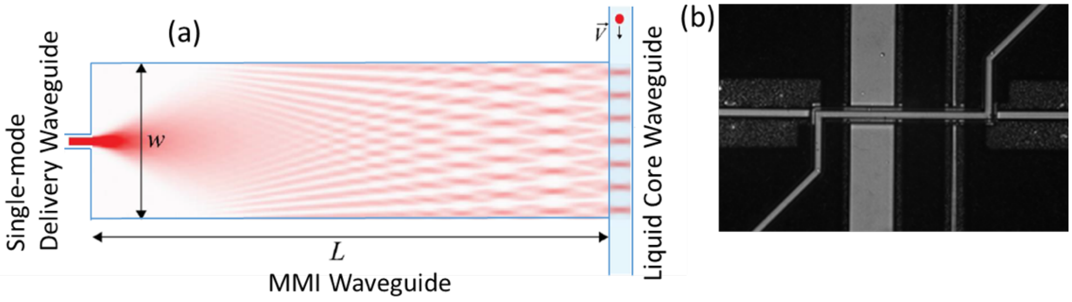

Fig 2.6 (a) Sketch of MMI propagation pattern with the waveguide design parameters projecting onto a liquid core waveguide (adapted from [56]) (b) Microscope image of an optofluidic biosensor with an MMI excitation waveguide as well as a single-mode excitation waveguide intersecting the liquid-core waveguide at different positions.

$$W_{eff} = W + \left(\frac{\lambda}{\pi\sqrt{\left(n_{core}^2 - n_{cladding}^2\right)}} \right) \left(\frac{n_{cladding}}{n_{core}} \right)^{2\sigma} \tag{2.26}$$

Here, σ = 0 or 1 for TE and TM modes, respectively. Furthermore, it can be shown that the beat length L_π of the two lowest order modes (where they go out of phase) can be calculated as:

$$L_\pi \approx \frac{4n_{core}W_{eff}^2}{3\lambda} \tag{2.27}$$

For a symmetric input mode profile, N self-images of the input beam can be obtained at a distance L from the start of the MMI section according to the equation:

$$L = \frac{3pL_\pi}{4N}\text{, p =0, 1, 2…} \tag{2.28}$$

where even and odd multiples of p generate direct and mirrored images of the input field. For p=1 and using equation 2.27, we get:

$$N\lambda = \frac{n_{core}W_{eff}^2}{L} \tag{2.29}$$

Equation 2.29 describes the relations between the key MMI waveguide design parameters and the excitation wavelength. As an example, at an excitation wavelength of 633 nm, a 75 µm wide MMI waveguide with n_{core}=1.51 and $n_{cladding}$=1.44 generates N=7 distinct spots pattern at a distance L= 1975 µm from the beginning of the MMI section.

Due to the transfer of the periodic spatial modulation of the excitation pattern on the temporal fluorescence signal, excitation with an MMI waveguide enables more reliable identification of targets compared to a single peak signal. In previous studies, multi-spot fluorescence excitation has seen 50,000x SNR improvement using a shift-and-multiply algorithm [63] and improved detection accuracy and sensitivity using multi-scale wavelet transform analysis techniques [67]. But, for an optofluidic biosensor, the true power of an MMI waveguide lies in its ability to perform wavelength division multiplexing on the same liquid channel at the same location. An MMI waveguide can be designed to have different number of self-imaging spots from specific wavelengths at a designed waveguide length, where the liquid channel is located. In other words, we can express this condition as:

$$N_1\lambda_1 = N_2\lambda_2 = \frac{n_{core}W_{eff}^2}{L} \tag{2.30}$$

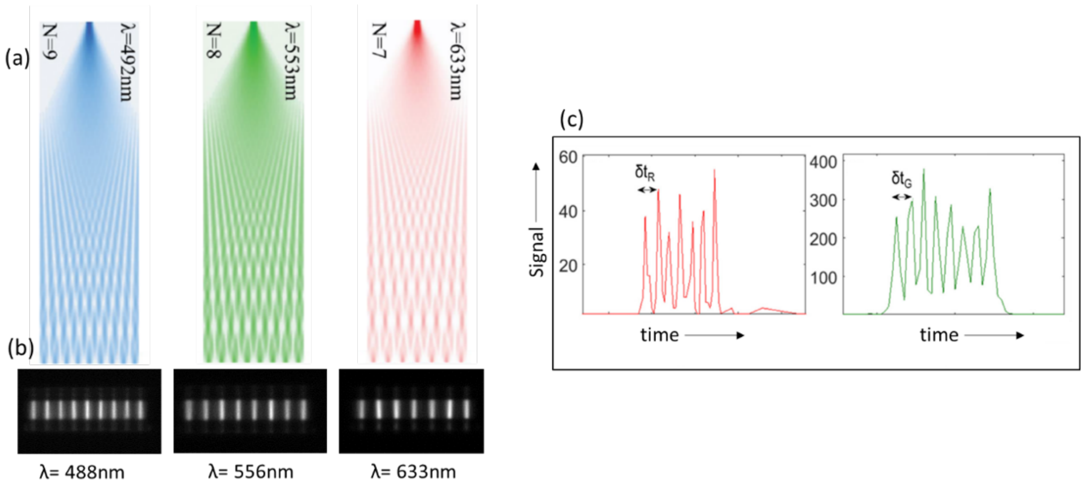

Fig 2.7 (a) Simulated MMI patterns at wavelengths λ= 488, 553, and 633 nm (adapted from [56]) (b) Fluorescence image of the excitation patterns at the above wavelengths projected onto the liquid core waveguide when the channel is filled with quantum dot-DI water solution for visualization. (c) Example of multiplexed detection of multi-peak fluorescence signals generated from labeled single-molecule targets. The 7-peaks signal is from a Zika virus nucleic acid tagged with TYE665 dye excited with a 633 nm laser, and the 8 peaks signal is from a ZIKV monoclonal antibody HM333 functionalized with Cy3 dye excited with a 556 nm laser (adapted from [72]).

Fig. 2.7(a) shows simulation of interference patterns at 492 nm, 553 nm and 633 nm respectively, which forms N= 9, 8, and 7 spots, respectively on the same location. From practical laser considerations, the MMI excitation waveguides on the optofluidic chip are designed to make the same number of spots on the liquid core channel at optimal wavelengths of 488, 556 and 633 nm, respectively [68]. Fig. 2.7(b) shows the periodic spot patterns generated inside the liquid core waveguide, which emits strong fluorescence signals illuminating the entire excitation volume when filled with high concentration quantum dots solution. If a bioparticle is labeled with a fluorescent molecule that exclusively responds to 633 nm excitation, the corresponding

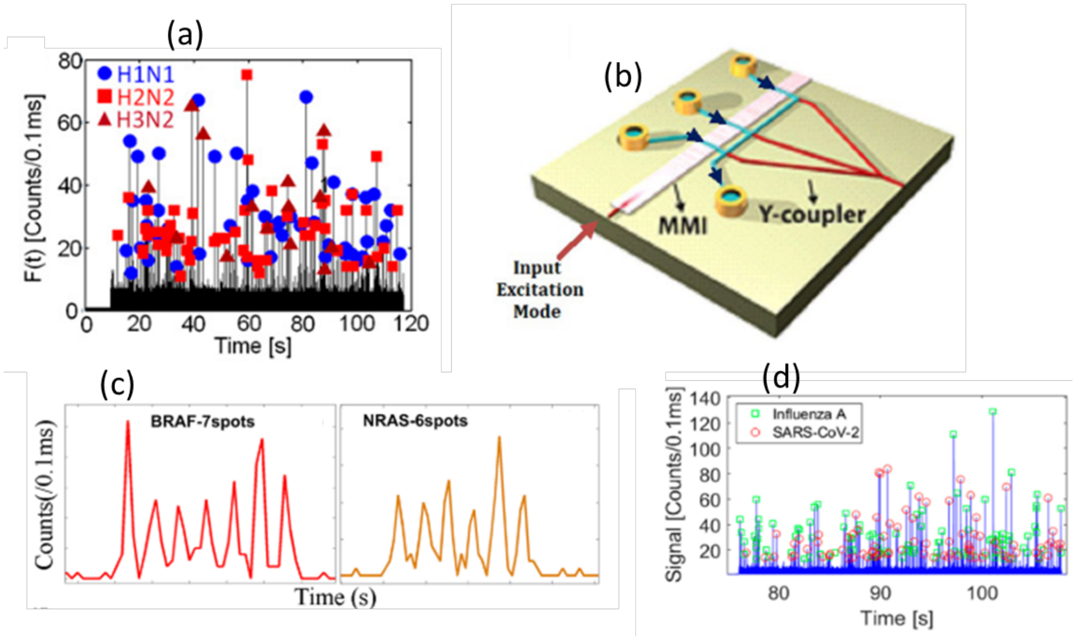

Fig 2.8 Application of multiplexed MMI excitation scheme in different bioassays and optofluidic architectures (a) Identification of different Influenza strains (adapted from [8]) (b)Multiplexed detection on an optofluidic chip with MMI waveguide intersecting 3 separate liquid-core waveguides, and a Y-coupler to combine all the signals (adapted from [70]) (c) Individual fluorescence signals from melanoma biomarkers, mutated cell-free nucleic acids- BRAFV600E and NRAS excited at 633 nm and 745 nm (adapted from [71]) (d) Distinction between single SARS-CoV-2 and influenza A antigens (adapted from [44]).

fluorescence signal will have 7 peaks in it, as shown in Fig. 2.7(c). Similarly, a fluorescent entity that responds only to 556 nm laser will have 8 peaks, and so on. This enables the multiplexed detection of fluorescently labeled pathogens from a mixed environment in the same sample volume.

It is important to note that multiplexed detection does not need to use mutually exclusive excitation, i.e. it is possible to scale up the multiplexing capability by performing combinatorial labeling schemes for different targets using fluorescence labels that can be excited with one or more lasers [69]. Multiplexed detection scheme using MMI waveguide has been successfully used with one or more liquid channels in detecting and identifying a broad range of target biomarkers at clinically relevant concentrations. Some examples (Fig. 2.8) include multiplexed detection of different influenza strains [8] [70], melanoma cancer biomarkers [71], antibiotic-resistance bacterial genes [69], Zika nucleic acid and protein antigens [72], and most recently, SARS-CoV-2 RNA and and antigens [44][45]. Apart from MMI waveguides, planar multi-spot excitation has also been implemented in the optofluidic chip using other types of planar waveguides, for example, a Y-splitter waveguide [45]. For their true implementation as a point-of-care diagnostic tool, multiple real-time data analysis platforms have also been developed [73][74].

While the planar MMI excitation and fluorescent detection on the ARROW platform offer some excellent spectral advantages, it also comes with strict choices on wavelength selection, waveguide design parameters and fiber coupling. In Chapter 3, we discuss a novel, free-space top-down illumination scheme on liquid-core waveguides in an optofluidic chip that can offer the same advantages as an MMI waveguide excitation but with more design and alignment flexibilities.

2.5. Spectrometry on the ARROW platform

Optofluidic devices on ARROW platforms can provide high excitation intensities delivered into a liquid channel using a planar geometry. Therefore, aside from single molecule detection and identification, they can be also very useful in integrated, on-chip molecular spectroscopy applications. One such case is the sensing of inelastic Raman scattering from molecules [75]. When polarized light from a dielectric medium is incident on metallic nanoparticles smaller than the wavelength of light or nanostructured substrates, it induces oscillations of conduction electrons due to absorption, causing a localized surface plasmon resonance vibration at the surface. When a molecule is adsorbed to the metallic nanoparticle, the intrinsically weak electromagnetic Raman signal is greatly amplified, a phenomenon known as Surface Enhanced Raman Scattering (SERS) [76]. The SERS spectra contain information that can work as a vibrational fingerprint of the molecules. This is extensively used for different chemical [77], biosensing [78], and single molecule applications [79]. In ARROW optofluidic platforms, the dependence of SERS signals on the incident irradiation and molecular concentration for rhodamine 6G (R6G) molecules has been previously studied [80].

The ARROW layers in this study consist of alternating SiN/SiO_2 layers surrounding a 12 x 5 μm hollow channel. A 2.47 μm thick SiO_2 cladding covers the top ARROW layers. The liquid-core waveguide in this design is coupled to a 12 x 5 µm solid-core excitation waveguide (Fig. 2.9(a)). Light from a He-Ne laser (λ=632.8 nm) was coupled into a single-mode fiber, which was wound through a polarization controller and butt-coupled to the excitation waveguide. The output light was collected with a 100x, NA= 0.85 collection objective attached to a Raman spectrometer (Jobin Yvon). The sample for this SERS experiment was solutions of R6G molecules with nominal concentrations varying between 0.3 and 30 µM combined with NaCl-induced aggregated silver nanoparticles (1 nM). This solution has been popularly used to provide a good proof-of-concept for SERS detection experiments [80].

The detected SERS time-averaged spectra for a range of excitation input irradiances (2, 5, 19, 22 35, 40 kW/cm^2) are plotted in Fig. 2.9(b). All show the characteristic R6G vibrational peaks with Stokes-shifted wave numbers 1320 (p1), 1370 (p2), and 1520 (p3) cm^{-1} corresponding to the C-O-C and aromatic C-C stretch vibrations, with linearly

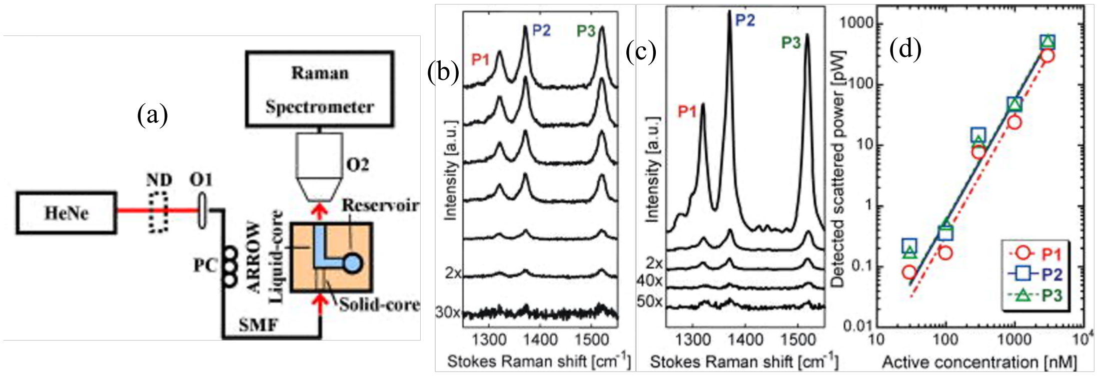

Fig 2.9 SERS signal detection in ARROW optofluidic devices (adapted from [80]) (a) Chip architecture and experimental setup (b) Power dependence of detected SERS signals at 300 nM active R6G concentration. (c) Detected SERS signals at different active concentrations corrected to a nominal input irradiance of 15.2 kW/cm^2 for differing alignment between measurements. (d) SERS signal power vs concentration. Lines: quadratic fits with equation 2.31.

diminishing intensity for lower irradiance levels [80]. Assuming negligible sample absorption and stimulated Raman scattering, the SERS power P_{ds} generated in the chip can be expressed by:

$$P_{ds} = F_{coll} \frac{\lambda_e}{\lambda_s} \kappa e^{-\alpha_1 L_1} \frac{(1-e^{-\alpha_2 L_2})}{\alpha_2 L_2} N^2 \sigma_{SERS} I_i \qquad (2.31)$$

Here, F_{coll} is the angular collection factor, λ_e and λ_s are the excitation wavelength and Stokes-shifted scattered wavelength, respectively, κ is the device coupling coefficient, α_1, α_2 are the solid core and liquid core waveguide loss coefficients, respectively, N is the number of adsorbed molecules (which is typically less than the number of actual molecules in the solution), σ_{SERS} is the effective SERS Raman cross-section, and I_i is the input irradiance. Independent, separately measured values were used for $F_{coll}, \alpha_1, \alpha_2$, and σ_{SERS}, leaving κN^2as the only free fitting parameter [81][57], which is connected to the R6G concentration. The SERS spectra for different concentrations are shown in Fig. 2.9(c) taken using the same liquid channel, by starting with the lowest nominal concentration (0.3 μM) and flushing the channel with water between successive concentrations. Fig. 2.9(d) shows the Raman signal power dependence at different wavelengths as a function of concentration, where the output signal was adjusted to a nominal excitation light output level to correct for differing alignments between measurements. The SERS signals show a quadratic dependence at all but lowest concentrations, where it becomes a linear fit [80]. This behavior is due to the increasing coverage of nanoparticles with R6G molecules, until all binding sites become saturated. Comparison with bulk microscopy SERS measurement shows that the active R6G concentration inside the ARROW is approximately ten times lower than the nominal concentration due to R6G molecule absorption on the SiN walls. The minimum detectable R6G concentration on the ARROW chip is found to be 30 nM, corresponding to approximately 4×10^5 molecules within the excitation volume of 44 picoliters.

The SERS signal detection from R6G molecules in an ARROW waveguide is the first proof-of-concept of spectral analysis on this integrated silicon-based optofluidic platform. The main advantage it offers is the unification of optical and fluidic paths, i.e., the ability to build a planar infrastructure of interconnected solid and liquid core waveguides. For a complete on-chip Raman study, the spectral analysis of the scattered signal should also be performed on the same integrated platform. In Chapter 6, we introduce an MMI waveguide-based integrated spectrometer based on similar material and chip architecture, which has the potential to enable on-chip spectral analysis of the Raman signal on the same chip as the ARROW waveguide and ultimately create a fully integrated, chip-scale spectroscopy platform.

Chapter 3: Top-down excitation in optofluidic biosensors

In the ARROW platforms, the principle of multi-spot or single-spot excitation and detection of individual moving particles is implemented using single-mode, MMI or Y-splitter waveguides, the MMI particularly being the enabler of multiplexed detection. However, the waveguide-based planar excitation approaches discussed in chapter 2 also come with the challenge of efficient coupling of light into the excitation waveguides. This is typically accomplished using edge coupling with a butt-coupled fiber or out-of-plane excitation with a grating coupler [82]. High efficiency in both approaches requires precise alignment, either to the waveguide mode or the grating resonance (incidence angle). Moreover, implementing spectral multiplexing in the MMI waveguide-based ARROW devices places additional constraints on the waveguide dimensions, increasing overall fabrication complexity [83]. In general, wavelength-dependent approaches also perform in a finite operational range. For example- MMI multiplexing using multi-spot excitation patterns maintains certain design wavelengths where they work best [8], while an input grating coupler has a bandwidth-limited coupling efficiency [84].

Free-space, non-planar excitation by directly shining light on the liquid core ARROW (LC-ARROW) waveguide offers an attractive solution to these challenges by eliminating the use of a single-mode fiber input, thus relaxing the alignment tolerances. Non-planar schemes have been relevant in a few other biosensing applications, for example, bulk measurement in plasmonic biosensors, microfluidic devices to modulate the emission signals, and multiplexed detection of spectrally overlapping signals [85]–[87]. In this chapter, we introduce two new techniques for leveraging free-space, multi-spot excitation in ARROW devices with a top-down approach. In the first approach, the LC-ARROW channel is covered with a thin, non-transparent aluminum (Al) film. µm-scale slits are etched into this film to enable multi-spot illumination using a focused laser beam. After investigating the fluorescence excitation capability of this scheme, we compare the signals with planar, MMI waveguide-based excitation. Next, spectrally exclusive multiplexed detection ability is demonstrated using spatially encoded excitation slit patterns to identify particles in a mixed sample. The second technique circumvents the need for the reflective coating by imaging an already patterned beam using a Y-splitter waveguide into multiple confined spots on the liquid core waveguide. Apart from simplifying the fabrication process, this approach also provides flexibility to excite targets anywhere in the liquid channel, offers more efficient delivery of excitation power, and gives the highest signal-to-noise ratio due to highly confined excitation spots.

3.1. Optofluidic device design and reflective film deposition

The ARROW optofluidic platform operation is based on low-loss guiding of fluorescence signals in a 12 µm × 5 µm liquid channel placed over periodic dielectric ARROW layers stacked on a silicon (Si) substrate, before ultimately coupling into a solid core collection waveguide. Using the fabrication processes described in Section 2.5, solid-core excitation and collection waveguides were fabricated either with single

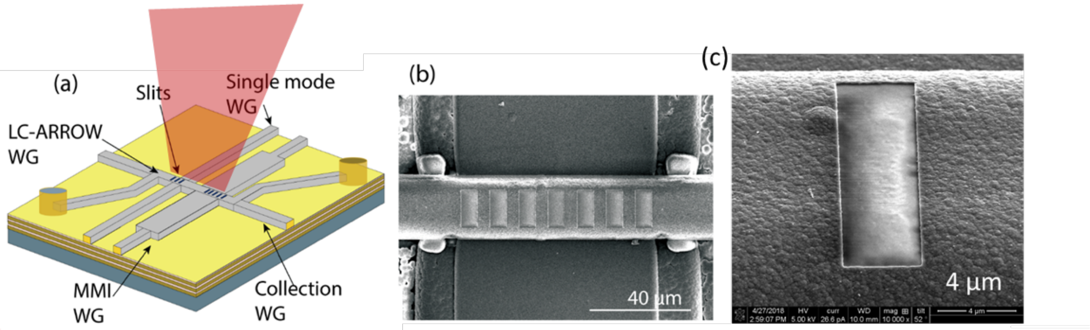

Fig 3.1 (a) Schematic of ARROW optofluidic device with planar waveguides and top-down slit patterns indicated. An elliptically focused laser beam is incident from the top-down on the slits. (b) Top-view SEM image of the metal-coated ARROW channel with milled 7 slits pattern. (c) Magnified view of a slit showing the exposed silicon oxide layer under the metal film.

oxide ridge waveguides [62], [71] (here used for the Y-splitter devices) or with a 6 µm thick high refractive index (1.51) core SiO_2 layer buried into another low refractive index (1.448) SiO_2 cladding layer with 6 µm thickness [61] (used for MMI waveguide devices). The LC-ARROW channel was created using an SU-8 sacrificial core and a wet etching step also described in Section 2.5. Instead of orthogonally intersecting waveguides, a target particle inside the LC-ARROW channel can be excited by a top-down, focused laser beam shaped to approximately match the dimensions of the channel (Fig. 3.1(a)).

In this scheme, the same buried structure as in planar, MMI waveguide excitation is utilized by covering the entire top surface with a 100 nm thin reflecting Al film, which was deposited using e-beam evaporation at a slow rate (<0.05 nm/s) to avoid flaking off. Finally, 4 µm × 15 µm, 100 nm deep light entrance slits with different patterns were milled using gallium (Ga+) focused ion beam (FEI Quanta 3D) with an experimentally set 30 kV, 0.5 nA nominal current and 550 nm nominal depth following

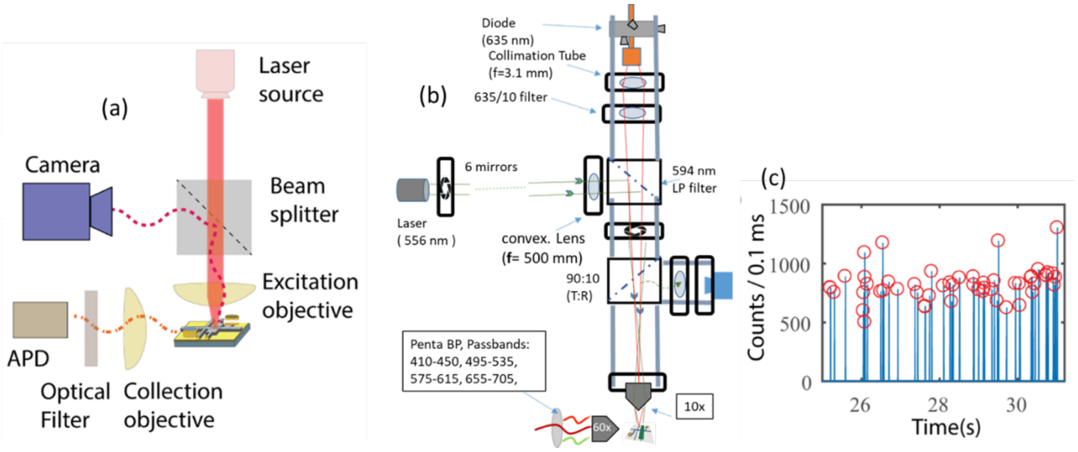

Fig 3.2 (a) Experimental setup for single-color fluorescence excitation and detection. (b) Setup for two-color multiplexed excitation on the same channel. (c) Example of detected signals from individual particles (circled in red) by the APD.

its Si milling protocol (dwell time-1 μs, volume/ dose- 0.15 × 10^{-9} m^3/s). Fig. 3.1(b) shows an SEM image of a 7-slit excitation pattern. Each pattern's dimensions and spacing can be reconfigured based on the application needs. In Fig. 3.1(c), a closer look at an individual slit shows the exposed top oxide under the Al reflecting film.

3.2. Particle detection using top-down excitation on aluminum film-coated biosensors

Fig. 3.2(a) shows the basic experimental setup used for excitation and collection of fluorescence signals from the ARROW devices. A 19 mW, 635 nm laser beam (Thorlabs HL6322G) is incident on the slits after passing through a 90:10 beam splitter and a 10× long working distance objective (Olympus PLN 10x), which also redirects the chip surface reflected image towards an alignment camera. During the multiplexed detection experiment, an additional 556 nm laser beam (SDL-556-030T) was sent through the beam splitter during using a long-pass filter (Fig. 3.2(b)). For the single laser (red) excitation experiment, fluorescence signals from 1 μm diameter (FluoSpheres^{TM}, 625/645 crimson) particles in a negative pressure-driven fluidic flow are collected, filtered, and finally detected by an avalanche photodetector (APD). Fig. 3.2(c) shows an example of data collected by the APD, each spike representing a single particle event.

3.3. Performance comparison with planar, waveguide-based multi-spot excitation

To characterize the optofluidic device performance using focused laser beam excitation, comparative analyses were performed between the top-down and MMI waveguide excitation schemes by exciting 1 μm and 200 nm diameter (FluoSpheres^{TM}, 625/645 crimson) fluorescent polystyrene beads at 10^6 mL^{-1} concentrations inside the

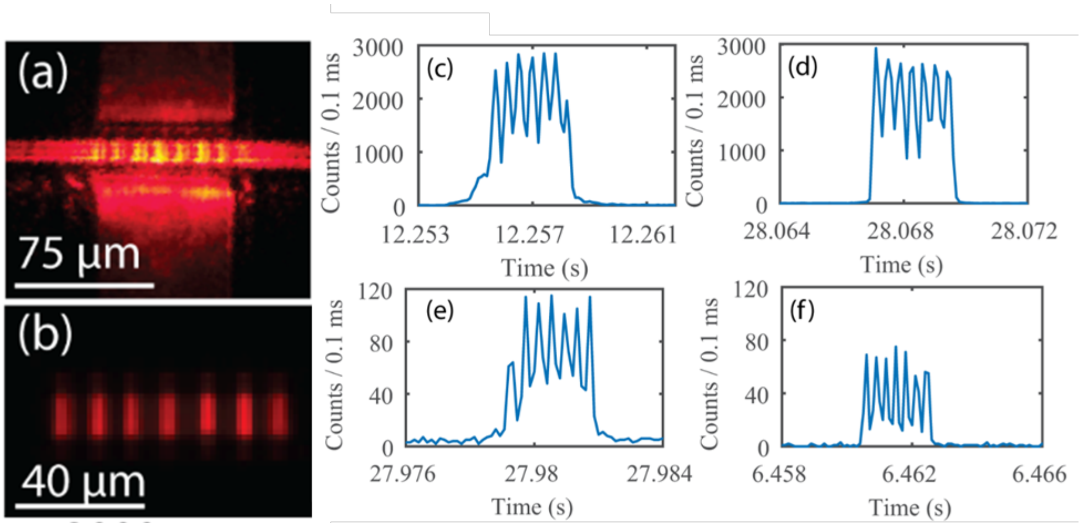

Fig 3.3 (a) Attenuated top-down excitation beam incident on the 7 slits pattern. (b) Top view of the excitation spots inside the LC-ARROW channel from MMI waveguide excitation (colorized image). (c,d) Signal from individual 1 μm beads using top-down and planar MMI excitations, respectively. (e,f) signals from 200 nm beads using top-down and planar MMI excitations, respectively.

same device. A 7-slit pattern (Fig. 3.1(b)) with 11 μm slit- to-slit spacing was milled at exact alignment with the MMI excitation waveguide on the LC-ARROW channel, as shown in Fig. 3.3(a) with an attenuated incident excitation beam. A 75 μm wide MMI waveguide coupled with 633 nm laser light (He-Ne, 5.3 mW) creates a very similar excitation pattern inside the channel, as observed in Fig. 3.3(b) by filling the LC-ARROW channel with high-concentration quantum dot-water solution. Figs. 3.3(c) and 3.3(d) show the fluorescence signals emitted from an individual 1 μm bead using top-down and planar excitation, respectively, and Figs. 3.3(e) and 3.3(f) show the 200 nm bead signals. Signals from the smaller beads appear sharper in both cases due to better spatial resolution.

The comparison between the salient optical parameters of the two excitation schemes is presented in Table 3.1. If the average intensity levels delivered to the LC-ARROW channel by the two schemes are matched, the top-down excitation allows controlling the delivered power level into the channel by varying the slit sizes, thus, in turn allowing more control over the time-domain fluorescence signal properties. A planar excitation approach requires precise alignment between a fiber and the excitation waveguide core to generate high-fidelity spots, but a free-space excitation over an Al-coated pattern provides similar multi-spot excitation volumes inside the LC-ARROW channel, with greater alignment tolerance, as shown in the table.

Table 3.1: Comparison of Excitation Schemes Properties and Detected Signals

Property	**Top-down excitation – Al coated ARROW**	**Planar, MMI waveguide excitation**	**Top-down patterned excitation – uncoated ARROW**
Excitation area (μm^2)	48	11.54	38
Excitation volume (μm^3)	240	138.5	189
Average excitation intensity ($\mu W/\mu m^2$)	11.54	11.31	5.28
Incident power per excitation spot (µW)	553	151	217
Excitation / Source power (%)	19.76	19.9	17.3
Signal mean ± standard deviation, 1 µm beads	2906 ± 295	2816 ± 209	2016 ± 246
Signal / Noise, 1 µm beads	181.6	281.6	504
Signal mean ± standard deviation, 200 nm beads	195 ± 158	161 ± 156	92 ± 92
Signal / Noise, 200 nm beads	12.2	16.1	23

The signal level distributions are very similar for the two schemes as shown in Fig. 3.4(a) and (b), respectively. The mean and standard deviations of these signals are listed in Table 3.1. The fluorescence signal-to-noise ratios (SNR), however, are lower for top-down excitation because of higher background noise level due to the relatively large

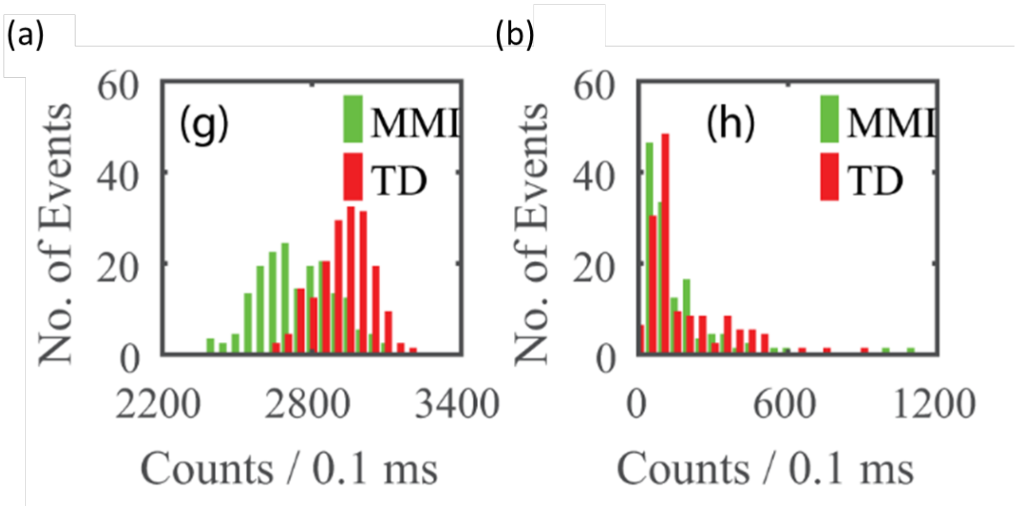

Fig 3.4 (a) Signal distributions from 1 μm beads using top-down (TD) and planar MMI excitations. (b) Signal distributions from 200 nm beads using top-down (TD) and planar MMI excitations.

incident excitation beam. The SNR for the top-down scheme can be further improved by coating the devices with a thicker Al layer using improved thin film deposition processes and patterning the slits [88].

3.4. Multiplexed single-particle Detection using top-down scheme

A key aspect of on-chip bioanalysis techniques is the multiplexed, simultaneous detection of multiple particles using a small sample volume. As illustrated in Fig. 3.5(a), we demonstrate this capability using top-down excitation in ARROW optofluidic biosensors by milling two different slit patterns 120 μm apart on the same LC-ARROW channel. Pattern 1 is a periodic, 5 slit pattern with 10 μm slit-spacing. On the other hand, pattern 2 consists of 3 slits with varying slit-to-slit spacing, i.e., one spacing is doubled to 20 μm to implement a non- periodic modulation. As shown in

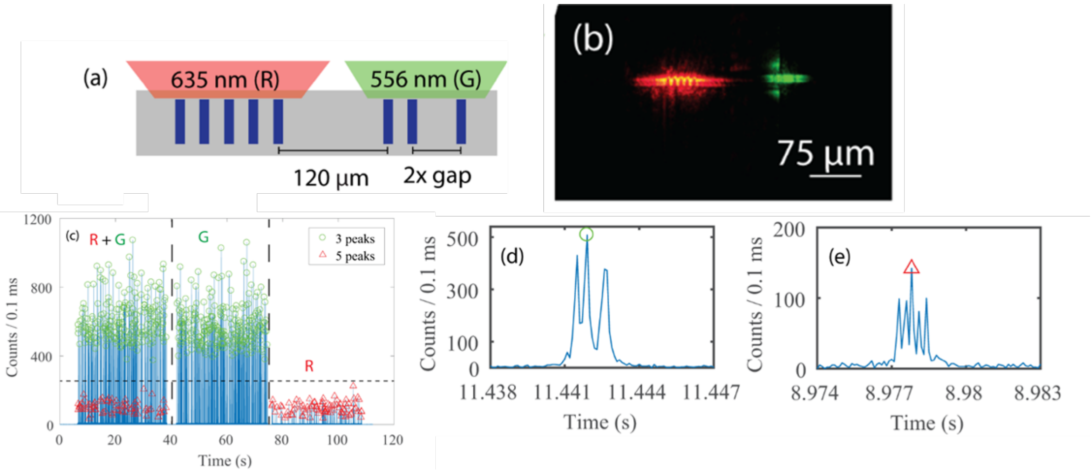

Fig 3.5 (a) Design illustration of 5 slits and 3 slits excitation patterns on the same LC-ARROW channel. (b) Attenuated 635 nm (R) and 556 nm (G) laser beam excitations on the 5 slits and 3 slits patterns, respectively. (c) Multiplexed fluorescence signals from simultaneous and separate excitation with two beams, separated by broken vertical lines. (d, e) Corresponding encoded excitation patterns in the single particle signals from the O and FR beads.

Fig. 3.5(b), patterns 1 and 2 are excited with two spatially separated focused laser beams at 635 nm (R) and 556 nm (G), respectively to identify distinctly labeled particles. Upon simultaneous (R+G) and separate laser excitations (R, G), a 10^6 mL^{-1} mixture of 1 µm fluorescent beads (Bangs Laboratories, 660/690 Flash Red (FR) and FluoSpheres™, 540/560 Orange (O)) emits signals with differing amplitude levels (Fig. 3.5(c)). This occurs due to the difference in laser excitation powers as well as different fluorescent quantum yields of the two beads. The individual signals from single particles reveal their distinct multi- peak signatures corresponding to respective excitation patterns, as shown in Figs. 3.5(d) and 3.5(e) for the green and red laser excitations, respectively.

In order to identify the signals based on their temporal signature, a multiscale signal processing algorithm based on continuous wavelet transform (CWT) was implemented.

More details on this analytical technique can be found in previous works by Ganjalizadeh *et. al* [67]. Briefly, custom defined wavelets (Ψ) matched with each pattern within a range of timescales Δt were correlated with the entire trace $f(u)$ to calculate the CWT coefficients across the time-domain fluorescence trace using the equation:

$$CWT_{f(t,\Delta t)} = \int_{-\infty}^{+\infty} f(u) \frac{1}{\sqrt{\Delta t}} \Psi^* \left(\frac{u-t}{\Delta t}\right) du \tag{3.1}$$

The maximum value of the CWT coefficient identifies the pattern (corresponding to the type of bead) and time-location of the signal. Table 3.2 lists the events statistics obtained from three different fluid samples containing separate as well as mixed flow of the two types of particles by simultaneously exciting with the Red and Green laser. From the separated bead flows, exclusive laser response with correct signal pattern from a particle is observed, which is also verified for single color (R, G) excitations.

Table 3.2: Detection Statistics Using Simultaneous R+G Excitation

Sample beads	**Detected 5 peaks events/ mL (x 10^6)**	**Detected 3 peaks events/ mL (x 10^6)**
FR	1.08	0
O	0	3.3
FR + O	1.10	3.35

The statistics for the mixed particle flow can also be verified using an amplitude-based statistics [89]. As the signal levels from two beads can be clearly separated by the horizontal line in Fig. 3.5(c), an amplitude-based classification of the signals produces the same results. Compared to a 7 and 8-spots periodic MMI excitation as discussed in chapter 2, such an encoded excitation scheme enables multiplexed detection using fewer number of slits over a smaller channel length, and can be very useful in designing ultra-compact biosensor designs for top-down excitation scheme.

3.5. Patterned top-down excitation on uncoated ARROW biosensor

A second approach for achieving free-space excitation in the LC-ARROW waveguides involves directly imaging an excitation pattern onto the detection channel. This method bypasses the need for depositing and patterning an Al layer, offering greater power efficiency by retaining the full incident power within the multi-spot pattern. In this scheme, we employ a 1×4 Y-splitter waveguide chip (Fig. 3.6(a)) to focus its output pattern onto an uncoated ARROW device. As depicted in Fig. 3.6(b), the same spots are imaged using a 10× objective onto a short section of the LC-ARROW channel, enabling multi-spot excitation.

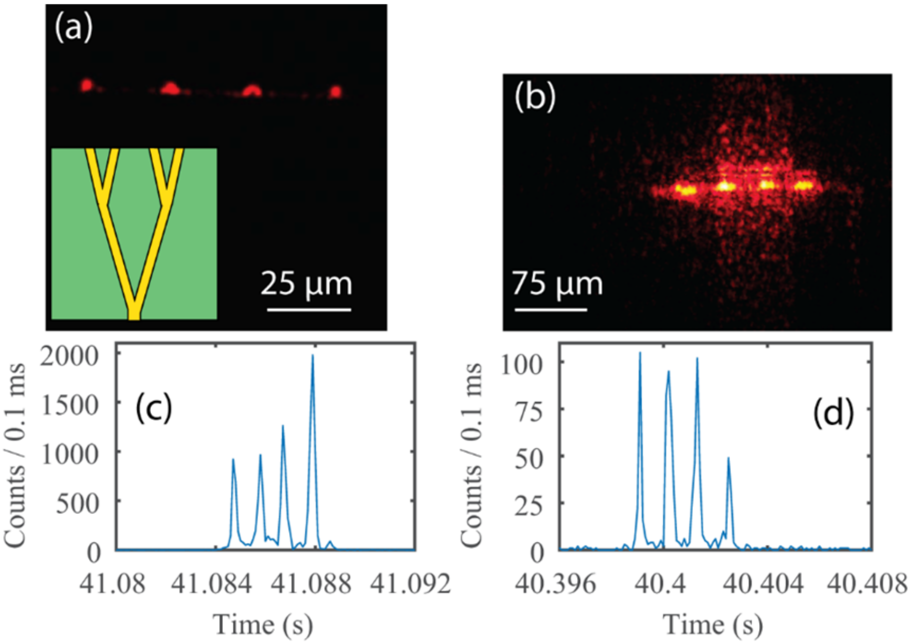

Fig 3.6 (a) Confined spot patterns emitting from a 1 x 4 Y-split waveguide facet. (b) Attenuated 633 nm patterned excitation beam incident on an uncoated ARROW chip. (c, d) Single particle signals from 1 µm and 200 nm beads, respectively using the patterned excitation.

For the sensor performance characterization using patterned excitation, the same samples from section 3.3 were utilized. The results also presented in Table 3.1 for comparison with the other two methods. Due to the laser-to-fiber coupling and other instrumental losses, the excitation intensity was lower, resulting in reduced signal levels compared to the other methods. However, this approach offers a higher SNR because of the highly confined excitation volume, which is an advantage over direct laser beam excitation. The improved confinement also leads to sharper and more distinct signal peaks, as illustrated in Figs. 3.6(c) and 3.6(d) for 1 µm and 200 nm beads, respectively. With an optimized excitation device design, for example, by using an MMI waveguide with the correct length for patterned excitation, this beam-patterning method could also be advantageous for implementing multiplexed detection strategies in optofluidic sensors.

The two free-space, top-down excitation methods discussed in this chapter demonstrate performances comparable to those achieved with a planar, MMI waveguide-based excitation approach. The multiplexing capability is particularly promising for differential screening of pathogens from a mixed sample. Furthermore, top-down multiplexing allows for the transfer of non-periodic spatial encoding to temporal fluorescence signals, enabling the full potential of advanced signal processing techniques. On the other hand, using planar waveguides for beam patterning offers an efficient, all-photonic solution for free-space, multi-spot excitation without the need for complex optical components. These findings highlight exciting new possibilities for ARROW optofluidic platforms in diagnostics and other sensing applications.

Chapter 4: Background of miniaturization of spectrometers

The modern methods of spectral analysis of electromagnetic radiation have their roots in the early days of Newtonian physics. In his book "*Opticks: or, A Treatise of the Reflexions, Inflexions and Colours of Light*" published in 1704, Sir Isaac Newton wrote about the results of his groundbreaking experiments on the fundamental nature of light with theoretical explanations of light dispersion [90]. While ancient civilizations like the Romans and the Egyptians knew how to use a prism to split sunlight in its component colors [91], Newton's works demonstrated that these split colors could be recombined to generate white light, and the prism does not create or alter the colors but merely separates the inherent components of the white light. In 1814, Joseph von Fraunhofer made a significant leap forward by demonstrating the dispersion of light using finely spaced slits instead of a prism, which laid the foundation for the field of modern spectrometers [92]. Since then, optical spectrometers have served as one of the most important instruments to date for major scientific inquiries, materials characterizations, and chemical analysis.

One key area of inquiry is astronomy, where spectral analysis studies the composition and motion of celestial objects, such as through Doppler shift analysis of exoplanets [93], or analysis of the absorption lines in the spectra of stars [94]. Biochemical analysis and medical diagnostics are another broad field that extensively employs different spectral techniques. One major category of biochemical analysis involves studying the continuous spectra from samples to study the properties like molecular bond structures, vibrational modes, enzyme kinetics, and so on. Examples of this type include fluorescence spectroscopy [95], Raman spectroscopy [96], UV-Vis absorption spectroscopy [97], and circular dichroism spectroscopy [98]. Another category involves imaging or detection of different biomolecular entities using distinct and discretely colored labels. A few examples of this category include fluorescence imaging of cells [99] as well as different biomarker detection techniques, such as barcode assays [100], antibody labeling [9], and nucleic acid labeling [101]. Other major application areas encompass material characterization [102], pharmaceutical drug development [103], quality control [104], environmental monitoring [105], food and crop monitoring [106][107], forensic analysis [108], clean energy research [109], and more. Broadly speaking, spectroscopy influences virtually every industry and field of intellectual inquiry.

Most commercially available spectrometers in the market rely on either of the two core technologies. The first kind employs a dispersive element, such as a grating or a prism, to spatially separate the wavelengths of incoming light and project them onto an array of sensors while the light is guided to and from the dispersive element by a series of mirrors. With the recent advancements in high-precision optics fabrication and detector technologies, dispersion-based spectrometers can reach ultrahigh resolution and have broad spectral ranges. In the dispersive instrument, each wavelength across the spectrum of interest is measured individually as the grating scans, and the subsequent data post-processing is relatively straightforward. The second category of spectrometers is based on the interferometric principle of light waves, where the incoming beam splits into two slightly different optical paths, followed by their recombination and formation of wavelength and path-dependent interference patterns on the detector. In this principle, the interferometer does not separate energy into individual frequency components. Rather, each point in an interferogram contains information from each wavelength, giving this approach the multiplexing or Fellgett advantage [110]. The post-processing in these techniques involves Fourier transform of the interferogram to get the frequency domain spectrum. The most popular implementations of this concept include Fourier Transform Infra-red (FTIR) Spectroscopy, Mach-Zender interferometer, and Fabry-Perot interferometer. In the next section, we take a closer look at the general working principle and the key performance parameters of each of these traditional spectrometers, before addressing the limitations imposed by each of the fundamental principles and engineering challenges.

In section 4.2, we introduce the rapidly growing field of integrated spectrometers powered by the recent advances in nano and micro-photonics, high-precision lithography, and computational techniques. Their growth has also been fueled by the growing need for portable, compact, lab-on-a-chip spectral analysis devices, where factors such as size, cost, power consumption etc. becomes as important as the core spectrometer performances. Beyond the straightforward miniaturization of conventional spectrometers, the past two decades have witnessed the emergence of novel photonics and MEMS-based integrated systems with ultracompact footprints, enabling spectral analysis in a wide range of scientific research and commercial platforms that were previously inaccessible.

4.1. Performance limit of different traditional spectrometers

In order to discuss the limitations and the practical challenges involved with the two conventional types of spectrometers, it is important to discuss their basic working principles. Dispersion-based spectrometers generate spectra by linearly dispersing the incoming radiation into its frequency or spectral components using common dispersive elements, such as prisms and gratings. Dispersive spectrometers can be further classified into two types: monochromators and spectrographs. A monochromator uses a single detector, narrow input and output slits, and a rotating dispersive element allowing the user to observe over a narrow wavelength range. Fig. 4.1(a) shows a monochromator's basic architecture, consisting of a reflection grating in a Czerny-Turner configuration [111]. On the other hand, a spectrograph uses an array of detector

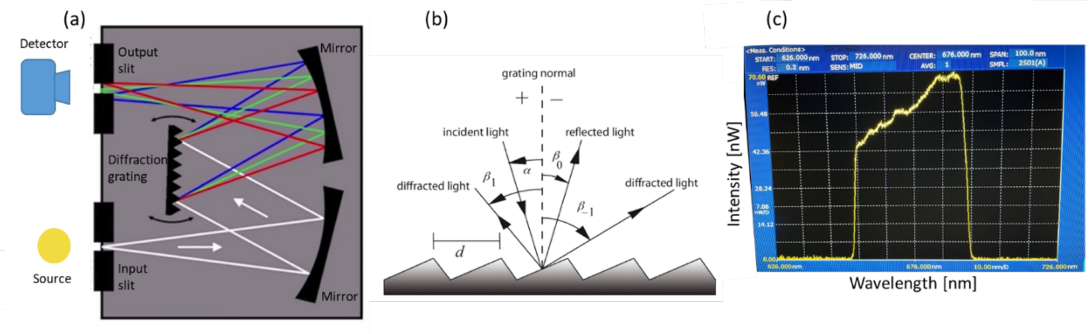

Fig 4.1 (a) Schematic of a reflecting dispersion grating-based monochromator in a Czerny-Turner configuration (adapted from nireos.com). (b) Ray diagram of a ruled grating showing the principal rays of incidence, reflection, and different orders of diffraction (adapted from newport.com). (c) Example intensity vs wavelength spectrum obtained from an optical spectrum analyzer (or, a spectrograph).

elements and a stationary dispersive element. The output slit is removed, and a spectral trace over a wide range of wavelengths is obtained simultaneously.

The most common dispersive element used in a monochromator or spectrometer is a diffraction grating, which can come in different types, including transmissive, reflective, ruled, holographic [112], etc. The different designs and working principles of the gratings, e.g., plane, concave, blazed [113], echelle [114], apodized [115], and so on, can also affect the efficiency and resolving power of the instrument. For a monochromator, a linearly wavelength-dispersed image of the input slit is formed at the output slit using different optical elements. The grating disperses the incoming light into its constituent wavelengths following the grating equation:

$$\frac{m\lambda}{d} = \sin\alpha + \sin\beta_m \tag{4.1}$$

Here, m = 0, ±1, ±2... is the diffraction order, d is the groove spacing of the grating α and β_m are the incident and m^{th} order diffraction angles, respectively, as shown in Fig. 4.1(b), respectively. Numerous optical configurations have been proposed to achieve the imaging, including the most popular Czerny-Turner configuration as mentioned above. In this case, input light is focused onto the input slit and then collimated by a curved mirror before hitting the reflective grating. A second focusing mirror translates the directions of the linearly dispersed wavelengths of light into different positions focused on the exit slit, ultimately generating a spectrum shown with an example in Fig. 4.1(c). The resolution of a spectrometer is defined as its ability to resolve two closely separated peaks in a spectrum, which is often expressed in terms of the resolving power:

$$R = \lambda/d\lambda \tag{4.2}$$

One of the most important factors affecting the resolution of a monochromator is its reciprocal linear dispersion, which represents the difference in wavelength per unit length in the image focal plane (output slit). Mathematically, this can be represented as:

$$D = d\lambda/dx \tag{4.3}$$

Besides the groove density and dispersion order of the grating, D also depends on the focal length of the instrument, i.e. the distance between the output slit (focal plane) and the second mirror. Apart from this, several other factors, e.g., slit width, detector pixel size, and optical aberration, also affect the resolution performance of a monochromator. While the advances in grating fabrication and detector technologies mean significant performance improvement for modern dispersion spectrometers, several fundamental limitations also become evident from the above analysis. First, the wavelength resolution scales inversely with the focal length, leading to a bulky instrument. For the same reason, the sampling interval between the wavelength data points depends on the position and pixel size of the detector, which can cause a significant cost increase. Second, since each point in the linearly dispersed output corresponds to a wavelength, the scanning process gets slower for increasing bandwidth with the same resolution settings. The trade-off between the choices resolution and bandwidth becomes important during every acquisition. Third, for high-resolution measurements, higher-order diffraction from a grating is generally preferred over the lower orders since there is finer spacing between wavelengths. This creates a compromise between grating dispersion and efficiency, since the low orders diffractions carry more power. Moreover, based on the choice of the grating design, it can produce unwanted overlap between high diffraction orders, leading to stray light or ghost images that can interfere with the measurement and degrade the quality of the spectrum. Fourth, misalignment of optical components, such as input fiber or the detector position, can result in decreased accuracy. For this reason, gas-lamp tubes, such as Mercury or Argon lamps, are often dedicatedly used in commercial spectrum analyzers as known reference sources for calibration and re-alignment. These sources require high arc current and special environmental handling. Fifth, the grating dispersion is not linear across the wavelength range, meaning that different wavelengths are dispersed at different rates. This can complicate data analysis and may require additional correction factors. Sixth, in case of broadband sources, the chromatic and spherical aberration of the optical elements and the spectral dependence of their reflectance also need additional correction factors.

An interferometric spectrometer's working principle is fundamentally different than a dispersion spectrometer and can be best explained by an FTIR spectrometer. Typically, it is based on the Michelson Interferometer experimental setup [116], an example shown in Fig. 4.2a. It consists of a beam splitter, a fixed mirror, a movable mirror that translates back on forth along the optical path, and a detector. Light from the source is

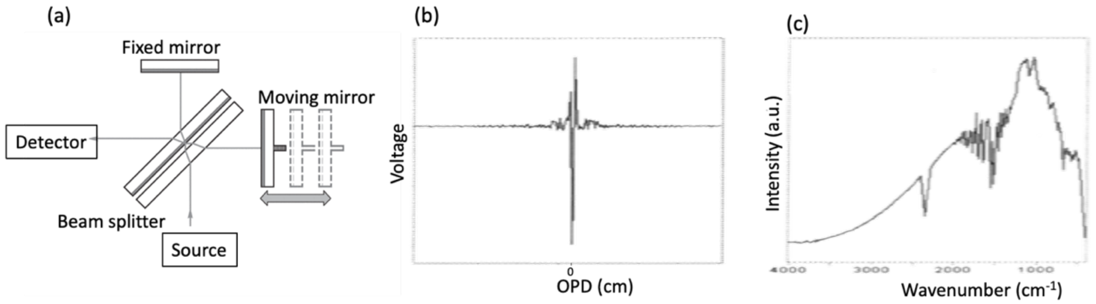

Fig 4.2 Schematic of a generic Michelson interferometer-based spectrometer (adapted from newport.com) (b). Example interferogram of a broadband source. The movable mirror can move both forward and backward from its zero path difference (ZPD) position, i.e., a double-sided interferogram. The big spike in the center is a classic signature of a broadband source, which comes from all wavelengths being in-phase at ZPD. (c) Spectrum generated from the Fast Fourier transform of the interferogram (b, c adapted from [117]).

split into two beams by the beam splitter; one beam is transmitted to the fixed mirror, and the other beam reflects off the beam splitter towards the moving mirror. After the reflections, both beams recombine at the beam splitter and travel onto the detector.

The moving mirror oscillates at a constant velocity, optionally timed using a laser beam frequency. The recombined beam is detected synchronously with the motion of the mirror. If the distance traveled by the two recombined beams is the same, the situation is defined as zero path difference (ZPD) [117]. But, as the movable mirror constantly moves closer to or further away from the beam splitter compared to its counterpart, the light beam reflecting off this movable mirror travels a different distance, i.e., a longer or shorter path than the other beam. If the displacement of the movable mirror away from the ZPD is denoted by Δ, the optical path difference (OPD) between the two beams is $2\Delta n$ (which can be further multiplied by 2, 4… or high numbers, depending on the number of used reflectors), with n as the refractive index of the medium filling the interferometer arms.

The raw FTIR data consists of a (signal, OPD) values pair. When the OPD is a multiple of the wavelength, i.e., OPD$= N\lambda$ (N=0,1,2…), constructive interference occurs between the two waves to generate a maximum signal intensity. Conversely, destructive interference results when the OPD$= (N + {}^{1}/{}_{2})\lambda$ (N=0,1,2…), resulting in a minimum signal intensity. The back-and-forth movement of the mirror between these two situations generates a cosine signal wave against the distance, known as the interferogram. Fig. 4.2b shows a typical example of an interferogram of a broadband source. In the case of FTIR spectroscopy, once an interferogram is collected, it is converted to a spectrum through a Fast Fourier Transform (FFT) algorithm [118]. This results in a signal intensity vs wavenumber ν (= wavelength^{-1}) plot as shown in Fig. 4.2c, representing a typical spectral acquisition process output. This output can be further converted to a wavelength spectrum by calibrating against a known laser source, typically accomplished using a He-Ne laser with free-space wavelength= 632.8 nm whose interferogram is monitored by an oscilloscope [119]. What is observed is a sinusoidal signal oscillating about an average value called the "zero level". A high-precision electronic circuit produces a voltage pulse when the He-Ne reference sinusoid crosses zero level, triggering a sampling of the spectrum. According to the Nyquist-Shannon sampling theorem, the maximum frequency that can be perfectly reconstructed from this sampling is half the sampling beam, i.e., the He-Ne frequency [120]. Thus, the minimum measurable wavelength is twice the wavelength of the reference laser.

In an FTIR scan, the detector measures the interferogram at discrete OPD data points as the moving mirror is translated in steps. Thus, a high-resolution scan requires more OPD data points. For example, let's consider two adjacent wavenumbers $\nu_1 = {}^{1}/_{\lambda_1}$ and $\nu_2 = {}^{1}/_{\lambda_2}$ that need to be resolved. For a maximum path difference d, they will have n and n+1 cycles, respectively. This can be written as:

$$d = n\lambda_1 = (n+1)\,\lambda_2$$

$$\nu_2 - \nu_1 = {}^{1}/_{d} \tag{4.4}$$

Thus, the resolution limit has an inverse relationship with the maximum OPD of the instrument. Since one OPD data point is equivalent to a single snap of the entire spectrum, an interferometric spectrometer is significantly faster than a dispersion spectrometer, where each data point represents one wavelength point (Fellgett's advantage). Moreover, unlike a dispersion-based spectrometer, the detector here simultaneously receives all the wavelength components of the input light, thus increasing the instrument's signal-to-noise ratio (Jacquinot's advantage). On the other hand, several limitations of an interferometric spectrometer become evident from the above discussions. Just as in a dispersion spectrometer, to increase the resolution, the physical size of the interferometric instrument needs to be increasingly larger. Second, high precision of the mechanical movement and very stable orientation of the moving mirror need to be ensured during sub-micron translations, which is very challenging. Third, a dedicated monochromatic laser source works as the trigger pulse for the interferogram data recording, effectively increasing the overall scheme's cost. Fourth, atmospheric elements, e.g. CO_2 and water vapor can interfere with IR-range measurements if the spectrometer is not properly purged with dry air or nitrogen.

Apart from technique-specific limitations of the dispersion and interferometric spectrometer approaches, a bulky commercial spectrometer built on either of these principles has some common limitations. To achieve high-resolution and stable performance, the optomechanical components, i.e., the grating rotation stage or the moving mirror translation stage, need to have high precision and be maintained at good operating conditions in various environments, increasing the overall cost of the instrument. Moreover, the wavelength separation element at the core of this spectrometer, i.e., a grating or an interferometer, can analyze only one source at a time. This poses additional challenges in scenarios where simultaneous and frequent analysis of a host of sources is required. Examples include astronomical observations in large ground-based telescopes where observation time is precious, or an environmental continuous CO_2 monitoring process that needs frequent statistical average readouts with high precision. Because of the bulky size and high cost of these spectrometers, their arrayed implementation to analyze multiple sources is also not a viable option, as each package will need dedicated movable optical elements and detectors. Many rapidly growing application spaces, e.g., handheld or smartphone-based devices, desire a spectrometric solution with a reduced physical footprint, cost, and power consumption, even with slight compromises in performance. In the next section, we discuss the different photonic approaches to developing a smaller, simpler spectrometer that has the potential to circumvent many of these problems.

4.2. Recent efforts in miniaturization of spectrometers

Arguably, the miniaturization of optical spectrometers is entering a golden age [10]. Since the early 1990s, a wide variety of miniaturized spectrometer systems have emerged. The early efforts focused on miniaturizing conventional technology and innovations involving more compact optics and packaging [121][122]. But in the last two decades, a wide variety of integrated spectrometers have also been demonstrated, involving diverse architectures, material platforms, and computational schemes [15], [123]–[125]. Like the generic classification of the benchtop spectrometers discussed in section 4.2, these integrated spectrometers can be grouped under two large umbrellas

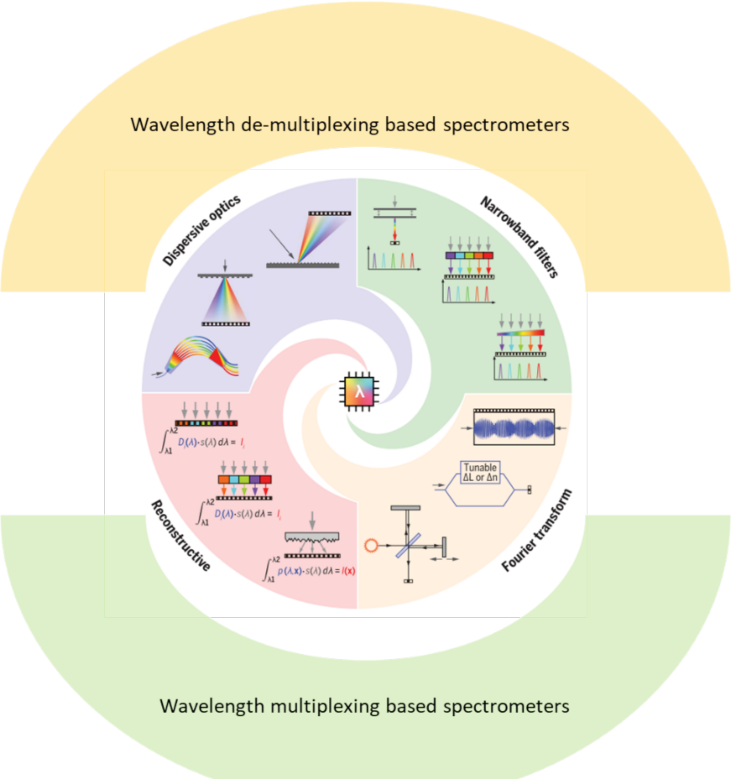

Fig 4.3 Classification of miniaturized spectrometer schemes with few examples (adapted and modified from [10]).

based on the nature of their fundamental technology: wavelength de-multiplexing (WdM) based, and wavelength multiplexing (WM) based spectrometers [12].

The WdM spectrometers split the incident signals' spectra, either spatially or temporally into separate channels, similar to a dispersion-based spectrometer (Fig. 4.3). Two more technology-specific categories can be found in these types of spectrometers. In one type, the separation of wavelengths is implemented using dispersive structures and optics, in which different wavelengths propagate in slightly different paths and arrive at spatially or temporally separated detectors. In the other type, WdM spectrometers can be implemented by using an array of narrowband filter elements or a single tunable narrowband filter, whose spectral responses separate the spectral contents of the input light.

The WM spectrometers do not disperse or filter the lights into separable channels; they typically modulate the overall signal pattern based on the entire spectrum and interaction between the different spectral components. The output is reconstructed by signal processing using specific algorithms. Depending on the modulation technology and postprocessing type, they can be further divided into Fourier Transform (FT) micro-spectrometers and reconstructive spectrometers. Similar to the bulky interferometers, the FT micro-spectrometers tune the optical path difference (OPD) among the spectral components of the incident light to obtain an interferogram, typically using a photonic or piezo-electric element, and convert the signal to a spectrum by performing a Fourier transform. The other type of spectrometer, i.e., the reconstructive spectrometer, has emerged as a new paradigm of spectral analysis and has received the biggest attention, resulting in a broad range of physical implementations. Here, spectral analysis is based on the computational analysis of wavelength-sensitive images or optoelectronic signals to extract spectral information. The image-generating micro or nano-scale features are often engineered with keeping commercial fabrication processes in mind. Such systems can also harness the development of continuously improving signal processing techniques, such as compressive sensing, transfer matrix calculation, and advanced machine learning techniques. In the following sections, we discuss each of these four classes of technologies in more detail.

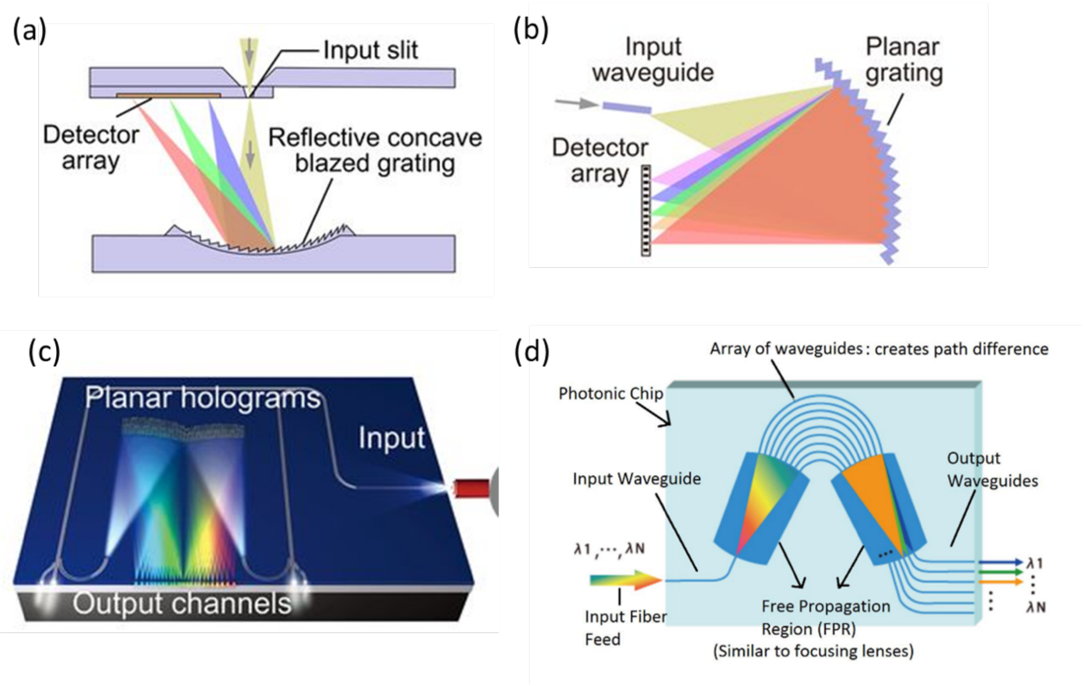

Fig 4.4 (a) Miniaturized dispersion spectrometer using a concave grating (adapted from [131]). (b) Dispersion spectrometer using a planar echelle grating an input waveguide (adapted from [134]). (c) Spectrometer using holographic diffractive elements and delivery waveguides (adapted from [129]). (d) Arrayed waveguide grating architecture (adapted from [141]).

4.2.1. Miniaturized spectrometers with dispersive optical elements

Advancements in fabrication technologies have enabled the scaling down of the components of dispersion grating or prism-based spectrometers on silicon photonics platforms. Thus, this most straightforward, dispersion-based approach has been implemented in numerous platforms with centimeter-scale footprints [126]–[128].

As the system footprint decreases, several factors must be considered. Similar to a benchtop dispersion spectrometer, the separation of wavelengths at the detector plane depends on the distance dispersed light travels. As such, for a given grating and detector array, the resolution of is proportional to the optical path length. As the device footprint gets smaller, one way to improve the resolution is to increase the detector's pixel density in the plane. However, this can pose additional challenges in terms of maintaining detector quality and alignment. Moreover, the resolution is also dependent on the collimating and focusing components to image the input slit onto the detector plane, increasing the device footprint even further. One workaround is to use a planar concave grating (PCG) as shown in Fig. 4.4(a), which can circumvent the need for complex collimation optics and multiple reflective components [129][130]. Commercial miniaturized spectrometers based on this design have achieved a resolution of ~10 nm with a footprint of 2 cm [131]. As alternatives to PCGs, planar echelle gratings as in Fig. 4.4(b) [132]–[134], meta-lenses [135] and hybrid grating-Fresnel lenses [136], Bragg reflectors [137], photonic crystal reflectors [138] have been demonstrated as diffractive components in an on-chip spectrometer. Planar slab waveguides have also been proposed to substitute the free-space optics [139][129], as shown with an example in Fig. 4.4(c).

Another alternative approach to create path-dependent dispersion effects using slab waveguide sections is the arrayed waveguide grating (AWG) [140][128]. AWGs use varying lengths of waveguides to create path delays, as shown in Fig. 4.4(d) [141]. Light enters from a single-mode input waveguide into a free propagation region and gets distributed among the imbalanced arrayed waveguides through in-plane diffraction. This is then captured preserving the phase front into a waveguide array, where each waveguide of the array is incrementally longer than the next one creating a phase graduation across the waveguides, similar to a dispersion grating. The waveguide modes then enter a second free propagation region where each wavelength of light constructively interferes, creating a horizontally dispersed spectrum at the output. The spectral resolution depends on the waveguide delay lengths and the number of waveguides., which also relates directly to the Free Spectral Range (FSR) or bandwidth of the AWG [142][143]. Compared to PCGs, an AWG is relatively simpler in design but still has a larger footprint as it has two free propagation regions and a waveguide array. It is also more susceptible to fabrication errors that results in phase errors, which is why AWGs typically exhibit stronger channel crosstalk than PCGs [12]. The main limitation lies in the relatively short waveguide propagation paths, the most crucial factor toward achieving high resolution. As a result, the resolution so far has been typically limited to a few nm [144][145].

4.2.2. Arrayed or tunable filter elements for spectroscopy

Narrowband filters can accomplish another form of WdM-based response by selectively transmitting light with specific wavelengths. In these systems, light passes through a single tunable filter [146] or through an array of multiple unique narrowband filters, each mounted on a dedicated detector. Examples of the second implementations include different types of passive resonant filters, e.g., ring resonators [147], Fabry-Perot etalons [148], photonic crystal cavities [149], and Bragg gratings [150], ARROW filters [151] each of which can produce extremely narrow linewidth. Such narrowband filter arrays have the advantages of single-shot measurement (fast measurement), while the resolution can easily reach ~10 pm resolution [146]. However, the static nature of their wavelength response makes the impractical for many applications where high or low-resolution spectral analysis of the same target depends on the task, such as

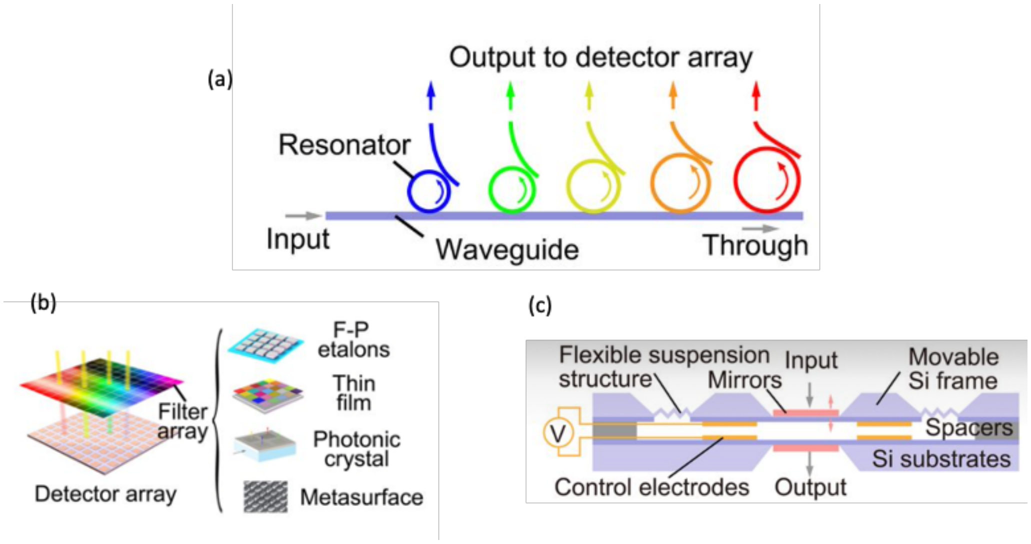

Fig 4.5 (a) Waveguide microring resonator filter array-based spectrometer. (b)Typical configurations of a tunable Fabry-Perot filter spectrometer. (c) Spectrometer based on filter array implementations. Adapted from [10].

astronomy. Also, these elements are sensitive to fabrication errors, and the performance can significantly degrade, similar to the dispersive elements.

Another unique advantage of a narrowband filter-based spectrometer lies in the tunability of its operation wavelength of operation. Examples of such filters include acousto-optic tunable filter (AOTF) [152], liquid-crystal tunable filter (LCTF) [153], and tunable microring resonators [154]. In these elements, the spectral response of transmission can be dynamically controlled by applying an electric voltage or an acoustic modulation signal that induces wavelength-dependent path lengths or polarization splitting. Tunable Fabry-Perot filters can be another promising MEMS-compatible prospect [155]. However, for filters with very narrow linewidth, tuning the wavelength for a broad optical range will require significant power consumption, and the operation is generally limited to a relatively small free spectral range (FSR).

4.2.3. Fourier Transform micro-spectrometers

The different forms of integrated Fourier Transform micro-spectrometers share the same basic idea as the conventional counterpart as discussed in section 4.1, i.e., to modulate the incident light via tuning the wavelength-sensitive optical path difference (OPD) to obtain the interferograms and obtain a spectrum in post-processing Fourier

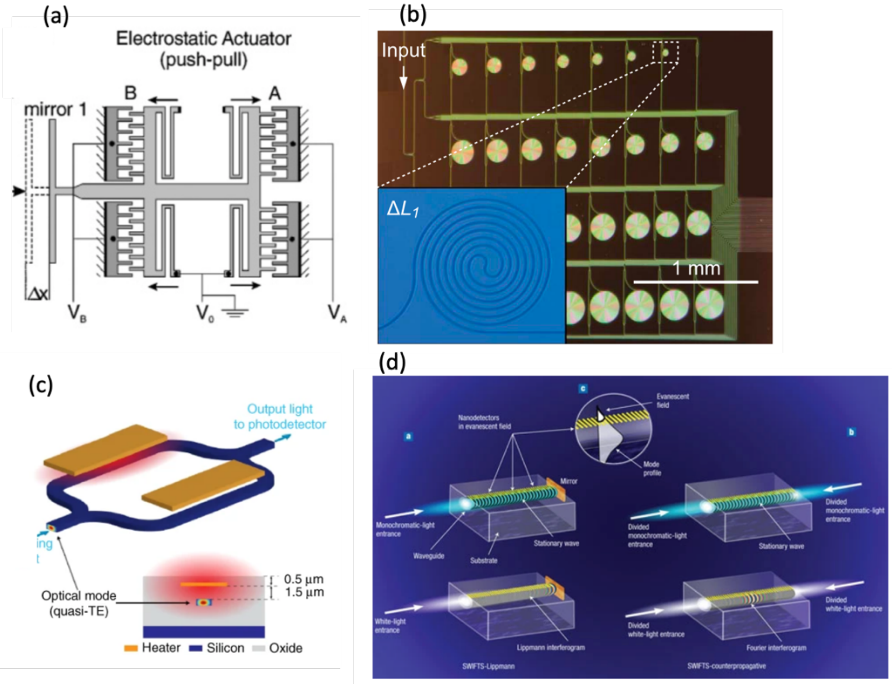

Fig 4.6 (a) A scanning-mirror FTS with an electrostatic comb drive actuator (adapted from [156]). (b)A spatially heterodyne FTS based on MZI arrays with spiral waveguides to increase the OPD (adapted from [157]). (c) Schematic representation of a temporal heterodyne FTS with OPD tuned in the time domain (adapted from [161]) (d) Stationary wave FTS in Lippmann configuration. Forward and backward propagating waves and the near field detection of an interferogram using nanoribbons (adapted from [166]).

Transform (FT). The key difference is the method of creating the OPD. The early versions of FT micro-spectrometers involved moving micro-sized mirrors with MEMS-based electric actuators, e.g. electrostatic comb actuators (Fig. 4.6(a)) [156]. As of the late 2000s, waveguide-based FT spectrometers based around Mach-Zehnder interferometers (MZIs) started being popularly used to induce the OPD among the interfering light paths [157]. Inside a single basic MZI component, light is split into at least two unidirectional pathways (waveguides) toward a single detector.

Some of these systems are based around spatial arrays of multiple imbalanced MZIs each inducing a progressively increasing amount of OPD through the subsequent paths before falling onto an array of detectors (channels) at the output, as shown by an example of a cluster of spirally coiled waveguides in Fig. 4.6(b) [158]. This group of FT spectrometers is termed as spatial heterodyne FT spectrometers (SHFTS) [159][160]. While such systems have demonstrated very high spectral resolution, they suffer from a similar problem as the bulky spectrometers, i.e., the resolution and bandwidth compromise with a reduced number of channels and the maximum OPD. On the other hand, temporal heterodyne FTS (THFTS) is more analogous to conventional free-space FTS as the OPDs are continuously modulated in the time domain, and the resulting interferogram is recorded using a single detector. The popular approach to modulating the OPD has been through thermo-optical modulation of the waveguide refractive index, for example, using embedded micro-heaters (Fig. 4.6(c)) [161][162]. Similar but faster temporal modulation can be achieved using electro-optic modulation in waveguides with certain material platforms (e.g., $LiNbO_3$) [163][164]. An alternative temporal modulation approach is a digital FT spectrometer, which uses a photonic switching circuit to dynamically change path and divert the signal along paths of different lengths [165].

A third variant of the FT micro-spectrometer systems is the stationary wave integrated FT spectrometer (SWIFTS). In this architecture, a standing wave is set up within a single-mode waveguide through the interference between two counterpropagating waves (in a Lippmann configuration, the standing wave is created by placing a mirror at one end of the waveguide) [166]–[168]. In contrast to the previously mentioned FT micro-spectrometers, where the interferogram is collected by one or more channels at the end of the path, here, a spatial interferogram is produced along the waveguide. This is collected by depositing metallic nanoribbons on top of the waveguide to sample the evanescent field of the standing wave (Fig. 4.6(d)).

4.2.4. Reconstructive spectrometers

Over the last 15 years, a new class of spectral analysis technology referred to as "reconstructive spectrometers" has pushed the boundaries of integrated spectrometer technologies with tremendous promise. The generic implementation, as the name suggests, involves imaging or recording signals from a photodetector array of the wavelength-sensitive light response of a photonic microstructure, developing a calibration matrix, and computationally reconstructing a test spectrum using matrix

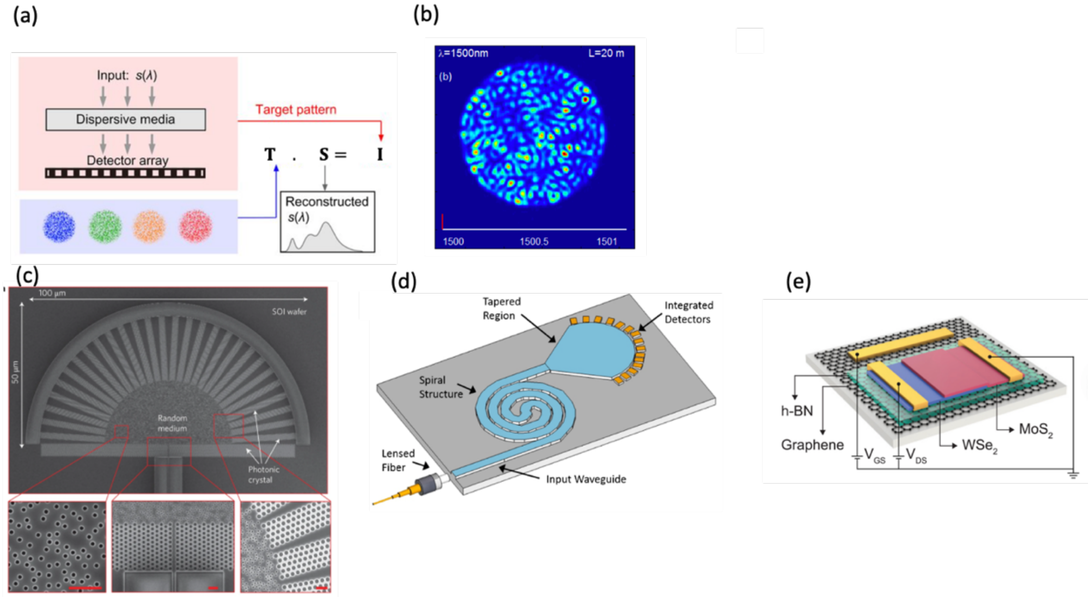

Fig 4.7 (a) Operational principle of a reconstructive spectrometer (adapted and modified from [10]). (b) Multimode fiber-based speckle spectrometer (adapted from [172]). (c)Integrated spectrometer based on a disordered photonic chip (adapted from [15]). (d) Spectrometer based on evanescently coupled spiral waveguide (adapted from [179]). (e) Integrated spectrometer with integrated 2D vdW junction-based spectrally tunable detector (adapted from [184]).

inversion and subsequent advanced optimization. More specifically, it is a complex spectral-to-spatial mapping approach that distinguishes the wavelengths by creating a signature spatial pattern (either 1D or 2D) in the spatial domain for each monochromatic wavelength, as illustrated in Fig. 4.7(a). The mapping device is typically a confined, dispersive propagation medium, for example, a multimode fiber (MMF) [169]. A polychromatic input light has multiple interfering fiber modes for each constituent wavelength, effectively creating a spectral encoding from the speckle pattern at the fiber facet.

The mathematical formulation of the spectral reconstruction, often known as the "Transfer Matrix" algorithm, has its roots in the image processing techniques of early 2000s known as compressed sensing [170]. The idea was first applied in the context of spectral reconstruction in an implementation using a photonic bandgap Bragg fiber [171]. For a spectral flux density of interest $S(\lambda)$, the flattened output intensity distribution recorded vector across the detector array, $I(x)$ can be expressed as:

$$I(x) = \int_{\lambda_2}^{\lambda_1} F(x,\lambda)A(\lambda)S(\lambda)d\lambda \tag{4.5}$$

Here, x denotes a position on the detector array, $F(x,\lambda)$ is the position-dependent spectral response of the dispersive medium (for example, an MMF output speckle pattern), and $A(\lambda)$ is the spectral sensitivity of the detector array. These two terms can be recorded and mapped as a single transfer matrix of the overall system, $T(x,\lambda) = F(x,\lambda)A(\lambda)$. The discrete, simplified form of equation 4.5 can be written as:

$$\mathbf{I} = \mathbf{T} \, . \, \mathbf{S} \tag{4.6}$$

where **I** is the N x 1intensity vector of the N spatial output channels, **S** is the M x 1 spectral intensity vector discretized in M spectral channels, and **T** is a N x M matrix. Each column of T represents the discretized intensity vector produced by a monochromatic light, represented by an **S** vector with a single non-zero element, i.e. only one active spectral channel. In the calibration process, **T** is created by recording the intensity vectors across a range of wavelengths at discrete steps. The dissimilarity between two consecutive patterns determines the resolving power of these type of spectrometers [172]. The reconstruction process of an unknown spectral vector from an intensity distribution involves calculating the inverse matrix $\mathbf{T}^{-1}$ and plugging it in the formula $\mathbf{S} = \mathbf{T}^{-1}.\mathbf{I}$. The tricky part in the process is performing the matrix inversion of **T**, which is typically ill-conditioned in the presence of experimental and background noise and can be a computationally expensive process for a large array of intensity vectors. Typically, inversion is performed using a truncated singular value decomposition process which suppresses the small eigenvalues and corresponding eigenvectors representing the noise elements [172]. The final spectrum is obtained by further nonlinear optimization to minimize the error $||\mathbf{I} - \mathbf{T}.\mathbf{S}||^2$ using different techniques [173][174].

This matrix-based spectral reconstruction approach has been successfully implemented to develop high-resolution, broadband fiber-based spectrometers based on different fiber designs (Fig. 4.7(b)) [174]–[177]. Meanwhile, different chip-based integrated spectrometer architectures have also been proposed. A few examples include disordered photonic chip [15], spiral waveguide [178], evanescently coupled waveguides [179], dispersive hole array [180], cascaded MZIs [181], and mutually coupled MZIs - microring resonators [182], some of which are shown in Figs. 4.7(c-d). Thanks to the advanced fabrication technologies, the spectral resolution limit on the integrated platforms has been pushed to little as 0.01 nm [179]. However, both implementations suffer from temperature variations, as a slight shift in any of the monochromatic wavelength responses due to temperature change can corrupt the entire calibration process. Furthermore, the elements of $\mathbf{T}$ depend not only on the position or wavelength of light but also on the input light's polarization and spatial profile. Moreover, the computational cost scales poorly with fiber resolution or increased bandwidth, as a system with an increasing number of variables and linear equations needs to be simultaneously solved. On the plus side, the use of a silicon photonics platform enables mass production for the integrated devices.

Another recent class of reconstructive spectrometers tailors the spectral response of the individual photodetectors, either by engineering the detectors directly or by placing filtering elements in front of the detectors [10]. In other words, the discretized signals from the detector array are represented as $\mathbf{P} = \mathbf{D}.\mathbf{S}$,where each row of $\mathbf{D}$ corresponds to a detector's response. This allows the possibility of utilizing nanostructured elements that works both as a detector and a wavelength-sensitive filter. Examples of this type (Fig. 4.7(e)) include a composition-gradient alloyed semiconductor nanowire [183], 2D material-based van der Waals junction [184], plasmon-tunable graphene photodetectors [185], and transmission cavity with an organic absorption layer [186].

Almost all the miniaturized spectrometer platforms discussed in this chapter have been developed with the requirements of various application scenarios in mind, where portability, cost, robustness, stability, speed, etc., become important metrics of operation. In the next chapter, applications of miniaturized spectrometers around three key disciplines are discussed, along with the potential future directions of the deployment efforts.

Chapter 5: Applications of miniaturized spectrometers

The different kinds of rapidly developing miniaturized and integrated spectrometers discussed in the last chapter offer great potential for large-scale industrial production and integration into more complex analysis schemes. A 2020 study showed that the market value of chip-scale spectrometers is projected to increase market volume from 2 million USD in 2019 to over 1.6 billion USD by 2024 [187]. Many of these implementations are compatible with the existing semiconductor fabrication frameworks and favorable to integrate seamlessly into public consumer products, such as smartphone integration [188][189], healthcare monitoring [190][191] etc. The current general focus has still been on integration into the research and industrial analysis processes, e.g., astronomical observations, biomedical point-of-care diagnosis, chemical analysis in agriculture, environmental monitoring, mineralogy, metallurgical hyperspectral imaging, forensic analysis- and the list could go on. The ever-decreasing footprints and low power consumption of these spectrometers, combined with the advances in computational algorithms and internet-of-things technologies, can potentially revolutionize each of these areas in the near future.

In the following sections, we focus on three key application areas where integrated spectrometers are replacing bulky benchtop spectrometers at a rapid pace while offering newer functionalities and advantages. The first field is astronomical observations, which have relied on spectral analysis for centuries to achieve major scientific discoveries. The second area involves instrumentation of biomedical measurements, i.e., on-chip sample analysis, biomarker detection, disease prevention, and long-term monitoring strategies. The final focus area is chemical sensing, which covers various applications starting from industrial materials analysis to metrology. While the discussion aims to highlight the important factors for consideration and establish and compare the key spectrometer metrics for these applications with different implementation examples, it only covers a fraction of the rapidly growing spectroscopy technological innovations and their applicabilities.

5.1. Applications in astronomy

Spectroscopy has been a critical tool in astronomy in the development of different observational techniques and advanced component analysis. Examples include analyzing the compositions and movements of extraterrestrial objects of interest, such as Doppler shift analysis of exoplanets [93][192], measuring the intergalactic distance and expansion from the stellar redshift [193], understanding the origin of the universe from the cosmic background radiation [194], and exploring deep space for extraterrestrial life or habitability of different planetary systems [195]. Presently, the need for advancements in astronomical spectroscopy is pressing with the advancements in very large telescopes (VLTs) and extremely large telescope (ELTs) systems. For example, in the next decade, multi-object spectrographs, such as DESI, the Subaru telescope's prime focus spectrograph, and the Keck-FOBOS are bringing multiplexing of up to 5000 fibers to 4-10m telescopes to simultaneously analyze 10^7 different spectra from as many targets across the sky [196][197]. Walking into the era of “big data astronomy”, the need for large-scale spectral analysis is expected to grow, necessitating instrumentation that can deliver 10^9 spectra in the coming years [198]. Aside from the promising results shown by the recent deployments of miniaturized spectrometers, the astronomy community has also started to recognize the potential of astrophotonic

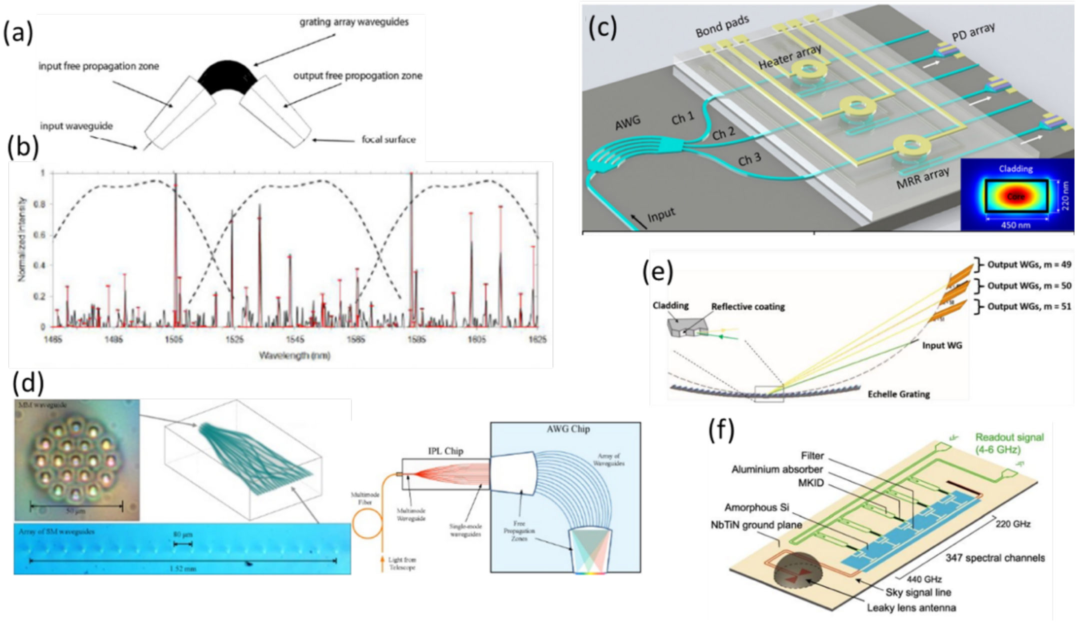

Fig 5.1 (a) Schematic of the AWG chip inside an integrated photonic spectrograph (IPS) mounted at the focal plane of a telescope (b) The night sky OH spectrum (solid black lines) using the Anglo-Australian Telescope IRIS2 spectrograph as a cross-disperser for the IPS in a, superimposed with the theoretical positions and strengths of the OH lines (red), and the diffraction efficiency envelop of the IPS for each order (dashed lines) (a,b adapted from [203]) (c) Schematic illustration of a PIC spectrometer with AWG and microring resonator combination on SOI platform. The insert shows the modal profile of a single-mode waveguide (adapted from [154]). (d) Left: Micrograph of the multimode side of an integrated photonic lantern (IPL), center: illustration of the photonic lantern structure, bottom: micrograph of the SM waveguide facets array, right: final integrated spectrograph assembly with the combination of the IPL with an AWG (adapted from [201]). (e) Schematic of a photonic echelle grating spectrograph (adapted from [220]). (f) Chip design of DESHIMA 2.0 integrated superconducting THz spectrograph at the ASTE telescope (adapted from [222]).

technologies and, in turn, the integrated spectrometers in solving these challenges [199].

Arrayed Waveguide gratings (AWGs) were originally invented for wavelength-division multiplexing (WDM) applications in telecommunications but subsequently has shown the most successful usability in preliminary testing in astronomical spectroscopy [200][201][202]. The first on-sky demonstration of the AWG was achieved at the Sliding Spring Observatory, Australia by Cvetojevic *et al.* [203] (Fig. 5.1(a-b)). One of the key science goals for AWG implementations in astronomy is the study of faint sources with large redshifts to probe the first billion year of the universe [128]. The main criteria involving this study is high resolving power R $(= \lambda/\delta\lambda)$ of ~1500 or more in the H band and spectral bandwidth coverage in the J (1100-1400 nm) and H (1500-1800 nm) bands [204][205][206]. Gatkine *et al.* have demonstrated astronomical AWG implementations in the Si_3N_4 waveguide platform with R~1300 with 23% overall throughput and low-crosstalk (-17 dB) between channels [141][128], while Stoll *et al.* have proposed $GeSiO_2$ -based AWGs with R~19,600 [145]. On-chip schemes like these are extremely compact and easily stackable to create an IFU (integral field unit) or multi-object spectrograph [207][208]. Achieving a high-performance photonic spectrograph requires an on-chip separation of the overlapping spectral orders of the AWG. One solution is to use AWG in combination with microring resonators (MRRs) as filters to separate the spectral orders, as shown in a few recent implementations [209][154] (Fig. 5.1(c)). The major limitations on performance of the AWGs is set by the size of its free propagation regions and the number of array waveguide elements that can be stacked on a small footprint device to achieve higher resolution [210]. Besides, the different forms of waveguide losses, e.g. coupling loss, sidewall scattering loss, bending loss etc. can affect the throughput performance [141].

In conventional methods, light at the telescope focal plane is collected using large multimode fibers which can support a large number of modes and introduce modal noise. A multimode to single-mode conversion is a necessary prerequisite to achieve the best performance out of the spectrographs such as the AWGs. A solution is to utilize a photonic lantern, which can efficiently convert the N-modes of a multimode fiber into N individual single-mode cores [211][212][213]. Apart from mode conversion, the lantern device can also be leveraged for advanced spectral and modal filtering operations, such as realizing a complex spectral filter with inscribed fiber Bragg gratings (FBGs) that could suppress the telluric OH emission [214][215][216], adaptive coupling of the brightest instantaneous MMF modes from a noisy wavefront for injection into photonic devices [217], or reformatting of the entrance slit of the spectrograph [218]. On-chip photonic lanterns have also been successfully integrated with an AWG to make an all-photonic device [201][219], as shown in Fig. 5.1(d).

Apart from the AWGs, photonic echelle grating (PEG) is another photonic technology solution well suited for low-throughput astronomy applications [220] (Fig. 5.1(e)), but the fabrication can be a complex, multi-step process due to the reflective surfaces [132]. Beyond these matured technologies in visible and NIR wavelength ranges, chip-scale integrated superconducting spectrometers (ISS) based on the combination of on-chip diffraction grating, filtering circuit and embedded antennas have been demonstrated for

THz astronomical observations in the ASTE 10 meter telescope [221][222]. Besides the AWG and the photonic lantern technologies, novel astrophotonic manipulation of light i.e. guiding, filtering, beam combining [223], dispersion engineering, on-chip wavefront sensing [224], integrated detectors etc. are continuously transforming the spectral analysis modalities at the telescopes around the world.

5.2. Lab-on-a-chip applications

The sensing of biomarkers and chemical composition analysis of biological samples, such as blood, breath, sweat, saliva, and urine, is of great importance for biomedical diagnosis [225][226]. For example, the detection of the glucose concentration in blood or saliva can provide diagnostic or monitoring information for diabetes. These measurements are commonly achieved by NIR spectroscopy techniques as the range contains prominent vibrational signatures of -CH, -NH, and -OH etc. functional groups. As a result, NIR spectroscopy with portable or handheld devices has gradually become a research hotspot, showing promising prospects for in-vivo biomedical sensing [227][228].

Modern challenges in bioanalysis, such as the need for automation, high throughput, small volume handling, and disposability etc. are increasingly being addressed by Lab-on-a-Chip (LOC) systems. These miniaturized laboratory platforms utilize microfluidic channels to manage tiny sample volumes and can be produced as cost-effective, disposable units [229][230]. Furthermore, LOC technology enables the integration of

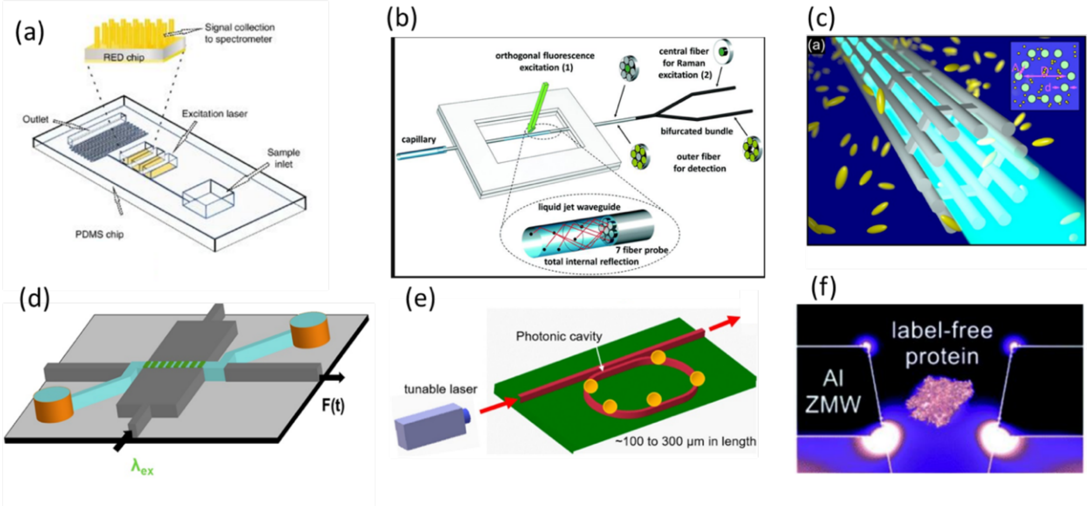

Fig 5.2 (a) PDMS LOC platform with SERS activated surface for brain injury biomarker detection from blood (adapted from [232]) (b) liquid-jet waveguide optofluidic LOC platform for fluorescence & Raman excitation (adapted from [234]). (c) Illustration of optofluidic light cage used for absorption spectroscopy (gray: dielectric strands and supports, blue: water, yellow ellipsoids: dye molecules, light cyan: light). The inset on the top shows the cross section of the structure including the relevant parameters (adapted from [235]). (d) Spectrally sensitive single-particle detection of SERS-CoV-2 antigen on a hollow core optofluidic chip (adapted from [9]) (e) On-chip photonic cavity with micro-racetrack resonator for aerosol spectroscopy (adapted from [239]). (f) Ultraviolet plasmonic enhancement of single protein autofluorescence in an aluminum zero-mode waveguide (adapted from [243]).

laboratory protocols and analytical methods into a single, compact cartridge. A few significant spectral analysis techniques integrated with Lab-on-a-Chip (LOC) systems include optical detection (UV/Vis mass spectroscopy) [231], Raman spectroscopy [232], nuclear magnetic resonance [233], and electrochemical detection [234]. The Raman spectroscopy on ARROW-based optofluidic LOC systems introduced in chapter 2 is a good example of improving signal-to-noise ratio in a confined liquid volume. However, Raman scattering is an inherently weak process with low scattering yield [235]. Therefore, different integration schemes between optofluidic device architectures and surface enhanced Raman spectroscopy (SERS) surfaces have been demonstrated [236] [237]. Recently, a PDMS-based optofluidic chip with a SERS-active substrate made of electro-hydro dynamically fabricated sub-micrometer pillars covered with a nanometric gold layer has been demonstrated the detection of picomolar concentration of N-acetyl aspartate (NAA), S100B protein, and glial–fibrillary acidic protein (GFAP), three indicative biomarkers with strong correlation to traumatic brain injury (TBI) [238].

Apart from Raman spectrosscopy, optofluidic LOC systems have also shown promising results in the domain of other bulk spectroscopic measurement modalities by integrating different on-chip optical and photonic elements with other sample processing and manipulation units. For example, a PDMS-based photonic LOC (PhLOC) integrated biconvex microlenses using soft lithography techniques to perform UV/Vis colorimetry, fluorimetry, and dispersion/scattering measurements on the same platform to measure the concentration of fluroesecent analytes [239]. Another LOC platform with liquid micro-jet waveguide has also demonstrated multifunctional (fluorescence, Raman) spectroscopic analysis of ethanol and spectrum-based concentration measurement of eosin Y solutions in water [240]. Another hollow core waveguide-based optofluidic light cage structure has shown promising prospects in absorption spectroscopy [241].

The aforementioned spectral analysis techniques involve analyzing continuous spectra that interact with the biosample. Another class of spectral analysis involves the detection of distinct and discretely labeled bioparticles in a multiplexed assay. In these cases, integrated photonic components on the LOC platform perform spectrally sensitive light guiding and signal manipulation. Examples of this category include fluorescence or Raman imaging of cells [242][243] and molecular biomarker detection techniques, e.g. barcode assays [100], nucleic acid labeling [101], and antibody labeling [9]. Optical micro-ring resonators have also demonstrated single-particle sensitive absorption spectroscopy by utilizing the temperature-sensitive whispering gallery modes due to focused laser excitation [244]. Recently, a photonic cavity enhanced silicon nitride (Si_3N_4) racetrack ring resonator-based sensor has detected single entities of N-methyl aniline-based aerosol particles in the NIR range using on-chip, cavity-enhanced spectroscopy [245]. Plasmonic nanocavities can also confine visible and near-infrared light to subwavelength volumes to locally amplify optical field intensity by several orders of magnitude [246]. Leveraging this, label-free autofluorescence and SERS spectroscopy performed on plasmonic nanocavities has been demonstrated to enable single-molecule sensitivity [247][248][249].

5.3. Chemical sensing applications

Aside from the two major application areas discussed above, integrated photonic spectrometers have become increasingly popular in different chemical sensing applications mainly due to their miniaturized size and potential for low-cost production. Some noteworthy disciplines include environmental monitoring, food and agricultural analysis, public health, pharmaceutical drug development, industrial process control, defense applications.

In the wake of global warming and ever changing climate patterns, environmental monitoring is of utmost importance for any major technological innovation. Some of the powerful spectroscopy techniques, e.g. emission and absorption spectroscopy of gases [250], multispectral imaging [251], laser induced breakdown spectroscopy [252], fluorescence Lidar [253] have been the key monitoring strategies for ozone layer observation, cloud and rain analysis, greenhouse gas measurement, air-quality indexing, oceanographic studies and most other forms of climate and weather monitoring. Spectroscopic analysis techniques are equally valuable in wildlife, marine and microbial biodiversity monitoring. As found in the HITRAN database [254], the absorption spectra of several gases in the UV-Vis-NIR range can be exploited using integrated photonics materials. Currently, two fundamental photonic absorption measurement techniques exist [255]. The first approach is using a tunable, narrow-linewidth laser and a broadband photodetector. This method can target narrow absorption lines in gases. A simple diode laser typically has a linewidth of a few MHz, while an absorption linewidth of ammonia at room temperature is on the order of 10 GHz [256], and it is possible to use a single detector with a small dark current. The second approach is using a broadband source and a spectrometer to measure the whole spectrum simultaneously. This approach is more common in the measurement of a wide observation bandwidth with large absorption dips. Frequency combs and mode-locked lasers feature very well defined emission lines over a wide wavelength span, and can be considered an optical ruler for both these approaches [257]. Several on-chip frequency combs have been demonstrated with promising performance, and can be potential candidates for gas sensing [258][259].

In case of gas absorption spectroscopy, the interaction of a gas sample and light need long path lengths for a detectable change in spectrum. In such waveguide-based sensors, the guided light penetrates the evanescent field outside the waveguide core and probes a sample close to the waveguide surface. Molecules present within the evanescent field will absorb light or generate Raman scattered light that will couple

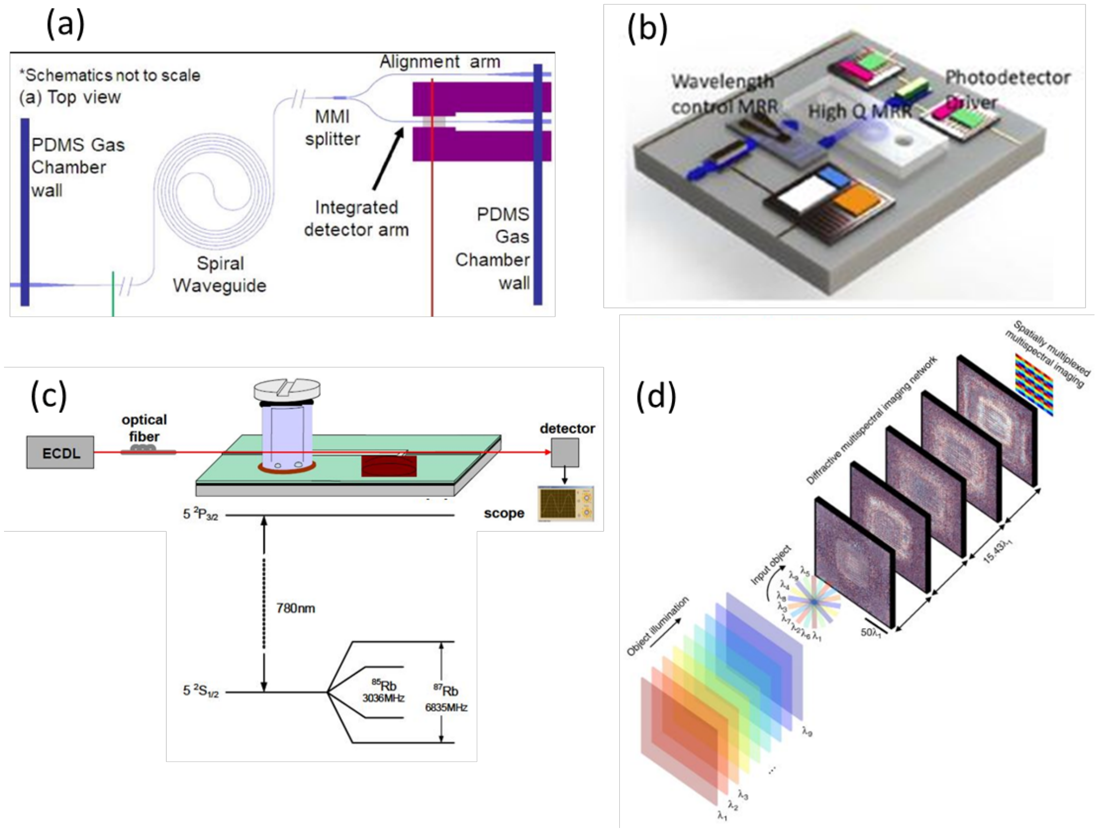

Fig 5.3 (a) Top view of an integrated gas sensor with a spiral chalcogenide (GeSbS) waveguide as the sensing element and a PbTe detector integrated directly underneath the waveguide (adapted from [255]) (b) CO_2 gas sensors based on microring resonator (adapted from [257]). (c) Rubidium spectroscopy on a chip. Top panel: experimental setup, Bottom panel: hyperfine electronic energy level splitting of rubidium D2 line.(adapted from [258]). (d) Multispectral imaging of an object based on diffractive optical network (adapted from [259]).

back into the waveguide modes. The respective interaction pathways give rise to analytical techniques such as waveguide-enhanced absorption or Raman spectroscopy [260]. Such a scheme bears an inherent challenge for PIC-based small footprint spectrometers. One common approach is to have folded or spiral waveguide to increase the interaction between the gas and the waveguide (Fig. 5.3(a)) [261]. Another idea is cavity-enhanced spectroscopy [262][263], where the resonance wavelength inside a high-Q resonator is sensitive to the presence of trace gases and modulations in the optical path length (Fig. 5.3(b)). A related promising potential application is on-chip Rubidium (Rb) vapor atomic spectroscopy in a vapor cell integrated with photonic waveguides (Fig. 5.3(c)). This has been previously demonstrated on hollow core ARROW waveguide platforms discussed in chapter 2 [264]. Alkali metals with hyperfine energy level splits, such as rubidium (Rb), sodium (Na) or cesium (Cs) have narrow spectral features on the order of the natural atomic (MHz) linewidth. This can be used as reference wavelength for important applications, such as stabilizing the emission frequency of a semiconductor laser by sending part of the laser beam through an atomic vapor cell and using the transmitted intensity as a feedback signal for the laser diode. Alternatively, these features are used as the reference standards in atomic clocks.

Another miniaturized technology used in a wide range of applications is multi or hyperspectral imaging, a technique that captures image data at specific wavelengths across the electromagnetic spectrum. Unlike conventional RGB camera, which captures images using three primary color bands (R, G, and B), multispectral imaging captures data across multiple specific wavelengths using spatially and spectrally tunable filters (Fig. 5.3(d)) [265]. These filters can be developed using different integrated photonic, plasmonic, or chemical filter schemes. Specifically, various integrated filter schemes and diffractive surfaces based on thin-film Fabry-Perot (FP) cavity [266], photonic crystals [267], waveguide resonators [268], and metasurfaces [269] have been exploited. These techniques are advantageous as they require minimal chemical sample handling and can leverage low-cost CMOS fabrication. However, the spectral imaging technique does pose several limitations. In most common forms of these implementations, there is often a trade-off between spatial (pixel size) and spectral resolution and similar to the reconstructive spectrometers discussed in chapter 4, multispectral imaging filters too require constant calibration in order to maintain their efficiency.

Based on the discussions in chapters 4 and 5, we will introduce a novel, high-performance integrated photonic spectrometer that based on the combination of multi-mode interference waveguide (MMI) propagation pattern with advanced machine learning analysis in chapter 6. Moving onward, we also demonstrate the astronomical application of the proposed spectrometer for spectral analysis using the solar spectrum.

Chapter 6: Multi-mode Interference (MMI) waveguide-based integrated spectrometer

In this chapter, we introduce the concept and implementation of a reconstructive integrated spectrometer for high-performance applications. It is based on imaging the wavelength-dependent light propagation patterns in multi-mode interference (MMI) waveguides as described in chapter 2 [66][8], followed by the analysis of the spectral content of these images with suitable machine learning (ML) techniques. This spectrometer scheme can be implemented in any integrated photonic format with wide latitude in device materials, dimensions, fabrication processes, and targeted spectral range. The reliance on post-imaging, ML-based analysis allows for strongly relaxed design tolerances, thus ensuring low complexity and cost. We demonstrate highly accurate spectral reconstruction of both narrow and broadband spectra in both the visible and near-IR range with a spectral resolution of $\Delta\lambda$= 0.05 nm and resolving power =$\lambda/\Delta\lambda$= 16,000. Furthermore, it is well suited for integration into a larger, more complex analytical systems in a diverse category of applications, for example, the astronomical spectroscopy or lab-on-chip applications as discussed in chapter 5. In chapter 8, the advantages and future potential of the MMI spectrometer are discussed with three application cases with a focus on astrophotonic instrumentation. These representative implementations highlight the versatility of the MMI spectrometer approach and point to its high customizability for many application settings.

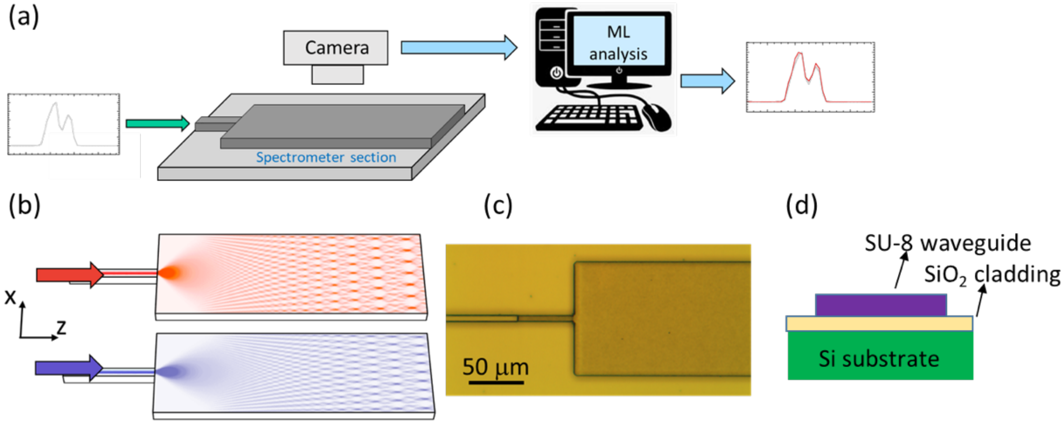

Fig 6.1 (a) Schematic overview of the multi-mode interference (MMI) spectrometer scheme. A continuous or discrete spectral signal is coupled into a chip with a MMI waveguide. The wavelength-dependent propagation patterns in the MMI waveguide section is imaged by a camera, and analyzed by a machine learning algorithm to reconstruct the spectrum. (b) Visual representation of the MMI propagation patterns at two different wavelengths. (c) Microscope image of SU-8 waveguide on silicon. (d) Cross-sectional view of the MMI waveguide.

6.1. MMI spectrometer working principle

The integrated MMI spectrometer consists of two components: a photonic chip to visualize a spectrum-dependent propagation pattern and a machine learning process for spectral reconstruction from the acquired image. The concept and its incorporation into a complete workflow are shown in Fig. 6.1(a). The spectrum to be analyzed is fed into a single mode waveguide on a chip, monolithically fabricated with the MMI waveguide. Light from remote sources can be coupled into the chip via free space optics or an optical fiber, and we used the latter arrangement for the lab experiments. The light then enters the wider MMI waveguide section in which the light propagation pattern varies strongly with wavelength. The pattern is imaged with a camera that is placed over the chip. Another alternative is to image the facet of the MMI waveguide, which would mean a smaller spatial dimension compared to the top imaging. The recorded waveguide pattern image is subsequently translated into a spectrum by a machine learning algorithm that can be chosen depending on the particular application. In this work, we discuss the use of a convolutional neural network (CNN) for analysis of both narrow and broadband continuous spectra.

Fig. 6.1(b) illustrates the physical concept behind the MMI spectrometer. A single-mode input waveguide sustains a input single lateral mode with a profile given by $\Psi_0(x)$. At z=0 (the start of the MMI section), the single-mode waveguide expands into a wider MMI waveguide section, which supports multiple lateral modes $\Psi_m(x)$. The input field is distributed among the multiple mode with amplitude coefficients c_m given by:

$$c_m \propto \Psi_0(x)\Psi_m(x)dx \tag{6.1}$$

With β_m as the propagation constant of the m^th^ mode, the overall field at a distance z inside the MMI waveguide can be represented as the combination of all modes as:

$$\Psi(x,z) = \sum_m c_m \, \Psi_m(x).\, e^{-i\beta_m z} \tag{6.2}$$

As the wave travels inside the waveguide, the phase relation between these modes keeps varying, resulting in a characteristic interference pattern. This pattern is dependent on the wavelength of light through the propagation constants β_m and the lateral wavenumbers $k_{x,y}$, which enable the extraction of wavelength information from this pattern. This MMI waveguide interference pattern, and its eventual self-imaging has been used extensively for generating multi-spot excitation patterns in lab-on-chip optofluidic biosensors [270][44][70], and as a component in optical communications

[64], as already discussed in chapter 2. Simulations of these patterns for two representative wavelengths are shown in Fig. 6.1(b) and illustrate how spectral information is mapped deterministically into the spatial domain.

It is important to note that spectral analysis is not carried out in analytic fashion, i.e. by directly calculating the input spectrum from the observed scattered interference pattern using equation (6.2) as this would require precise knowledge of and control over all fabrication and material parameters. Instead, we use machine learning algorithms that pick up on differences between patterns and that can be trained with signals at known wavelengths. Consequently, our fabrication tolerances are very relaxed, i.e. high accuracy for waveguide height, width, and etch depth is not required, minimizing the complexity of this approach and making it easy to implement in different waveguide systems. A closer look at the pattern evolution in the images acquired from a real MMI waveguide with slight shifts in wavelength is provided in chapter 7, along with a detailed description of the neural network analysis process.

A silicon wafer-based spectrometer chip was developed to implement this principle using SU-8 polymer waveguides on silicon dioxide. Fig. 6.1(c) shows a microscope image with a top-down view of the intersection area between the input and MMI waveguide sections. A cross-sectional view of the MMI waveguide is illustrated in Fig. 6.1(d). Both waveguides are fabricated in the same lithography step and have a height of 5 μm. The input waveguide is 4 μm wide while the MMI spectrometer section is 100 μm wide. To facilitate efficient out-of-plane scattering of light out of the MMI waveguide for easy observation from the top, we performed oxygen plasma etch on the

MMI section to create a rough top surface with “nanograss” features (more on this in chapter 9).

6.1.1. Waveguide fabrication

The SU-8 waveguides were fabricated by our collaborators at Brigham Young University (BYU) by growing a 6 µm layer of plasma enhanced chemical vapor deposited (PECVD) silicon dioxide (refractive index=1.51) on silicon wafers, followed by the spinning of a 5 µm layer of SU8-10 photoresist and soft baking at a ramped temperature from 65°C to 95°C. The wafer was then exposed to 365 nm UV photolithography, followed by a similar baking step and finally the development of the initial waveguide structure. For surface roughening, a 300 nm aluminum layer was deposited over the sample in an electron beam deposition chamber. Then AZ3330 photoresist was applied to the wafer and baked at 90°C for 7 minutes. Afterwards, it underwent photolithographic UV exposure with 465 nm light for 60 seconds. The mask in this step exposes the aluminum covering the surface areas on the SU-8 to be converted to nanograss. Exposed aluminum was removed in aluminum etchant at 50° C, and the AZ3330 photoresist was removed in acetone and isopropanol. The wafer then underwent O_2 plasma etching at 100 Watts for 8 minutes. This step results in the creation of the etched nanograss structure that induces the top surface scattering from of the waveguides. Finally, the wafer was again treated in aluminum etchant to get the final structure.

6.2. Operation and data acquisition

For spectral computation of continuous spectra, we use convolutional neural networks (CNNs), a special class of supervised learning technique to analyze the MMI images taken at different wavelengths. A detail description of the CNN architecture is discussed in chapter 7. As a general operational scheme, first, we collect many MMI images by varying the wavelength of the input light with single-peak spectra by shifting a tunable laser wavelength across an operational bandwidth. In each case, the actual spectrum of a particular input light is also recorded using a spectrum analyzer, thus creating an initial "input image-output spectra" dataset. Afterwards, a larger, broadband dataset with linear combinations of the single-color images is generated, which is used for the training and testing of the CNN model for both narrowband and broadband detections. This represents the very basic concept of MMI-based spectroscopy in which the spatial information within an MMI waveguide is mapped into 1D spectral information.

The performance of the MMI spectrometer chip was first tested in the infrared wavelength range around 800 nm. This regime is particularly attractive for many astronomy applications as discussed in chapter 5, and allowed us to explore the performance limit of the current device. Afterwards, we also performed similar performance assessments in the visible wavelength range with different training and test laser sources and found comparable performance. In the following sections, detailed discussion of the optical setup and the spectral reconstruction results are discussed.

6.2.1. Optical setups for training using tunable near-infrared (NIR) and visible lasers

For the NIR wavelength range operations, the data acquisition setup involves a single-mode fiber chip butt-coupled into an MMI waveguide to get the input light into the chip, as illustrated in Fig. 6.2(a). The generated MMI pattern is then captured using an Olympus PLN 10x objective and projected on a sCMOS sensor (Andor Zyla). The

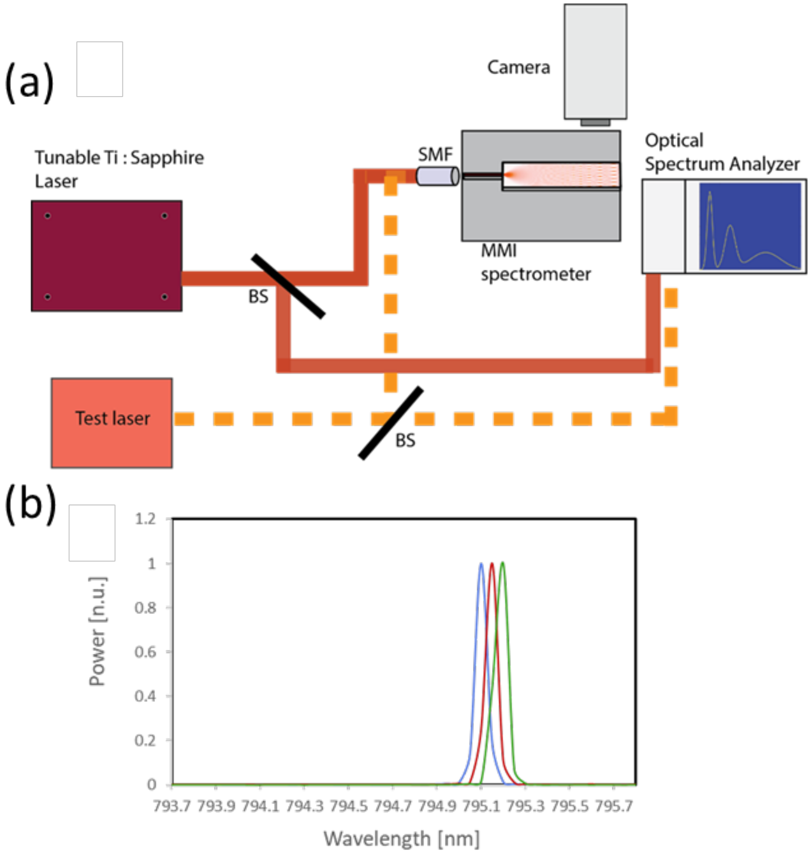

Fig 6.2 (a) Optical setup and experimental arrangement for NIR data acquisition. (b) Example narrowband, 0.05nm FWHM monochromatic wavelengths from the training laser at 0.05 nm intervals.

recorded image is in grayscale, i.e. the camera itself is not capable of differentiating different colors. To take the training images for the NIR wavelength experiment, a Ti:Sapphire cavity laser (Trestles 100M, Del Mar Photonics) is used to generate sweeping laser peaks between 793.8 and 795.6 nm in 0.05 nm steps by periodically tilting a Fabry-Perot etalon inside its cavity. The change in tilting angle and the etalon's finite free spectral range (FSR) generate the distribution of closely spaced laser peaks [271]. As seen from Fig. 6.2(b), the FWHM of each individual wavelength is 0.05 nm, ensuring some overlap between the training signals for continuous coverage of the entire bandwidth. A 532 nm solid state laser pumped the Ti: Sapphire cavity, and the wavelength tuning elements, i.e. the Fabry-Perot etalon and the birefringent Lyot filter (used for another experiment described in chapter 8) as shown in Fig. 6.3(a) were rotated by connecting to their tuning stepper motors using a custom-built Arduino circuit (Fig. 6.3(b)). The output monochromatic light is simultaneously fed into the MMI chip and an optical spectrum analyzer (Yokogawa AQ6374) to generate scatter images with corresponding reference spectrum labels. A synchronized routine of multiple scripts written in Python, C++, and LabVIEW controlled and communicated

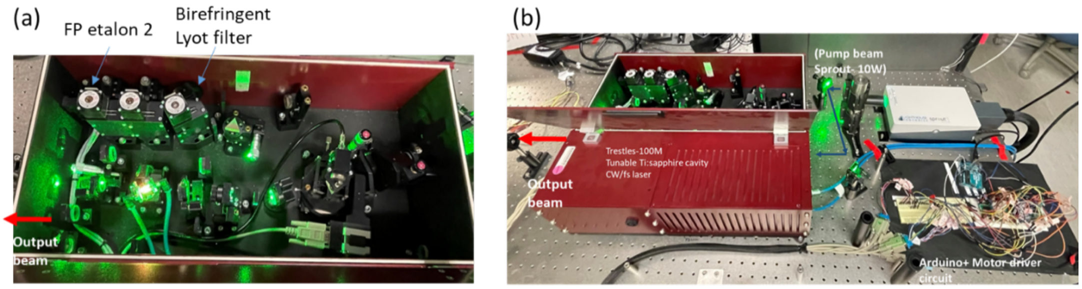

Fig 6.3 (a) A closer look inside the Trestle's tunable Ti:Sapphire cavity. (b) Crystal pumping mechanism and custom-built circuit to drive the etalon and filters inside the cavity.

among different instruments in each step. The test laser (Vescent Photonics D2-100-DBR) with a constant wavelength is also fed into the MMI chip and the OSA simultaneously using a similar optical scheme. Each wavelength was fiber-coupled ten times into the MMI chip to create slightly different mode excitation conditions for a total of 250 scatter images. A 952 μm x 95 μm (1200 x 120 pixels) area of the image near the end of the MMI section was selected as the input image region-of-interest (ROI) to train a CNN.

For the visible wavelength training data acquisition, a supercontinuum laser source (SuperK Extreme, NKT Photonics) was launched into a monochromator (Horiba iHR550), as shown in Fig. 6.4(a). Since the commercial monochromator was designed

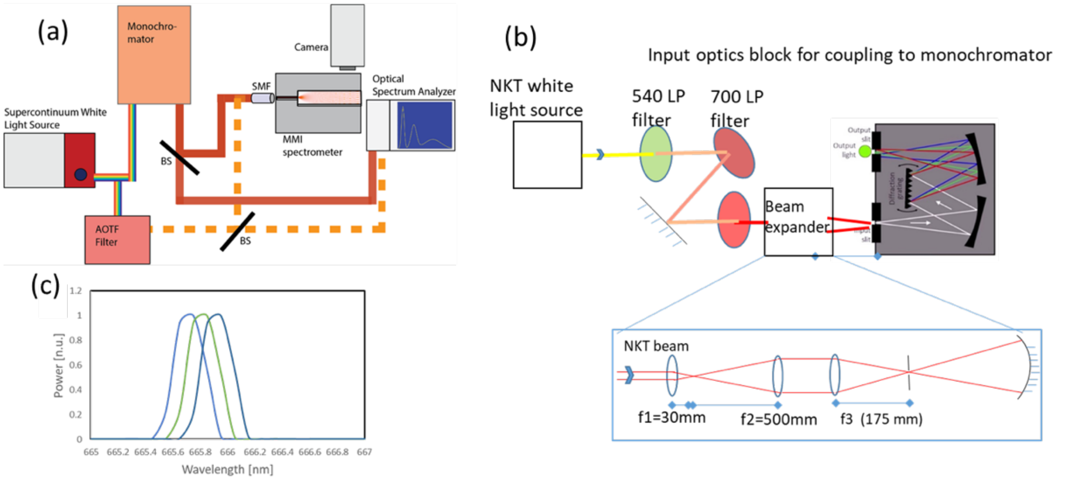

Fig 6.4 (a) Schematic of the optical setup for training the MMI spectrometer in the visible wavelength range using a broadband supercontinuum source, filtered by a linearly dispersive monochromator. Unlike the NIR wavelength arrangement, the external test source is the output of an acousto-optic tunable filter (AOTF), another wavelength tunable test source. (b)Breakdown of the custom-built input optics block for coupling the broadband white light source into a monochromator to get narrowband, tunable laser light. The inset shows the specifications of the Galilean beam expander used to match the beam size and divergence with the monochromator input slit. (c) Example narrowband, 0.3nm FWHM monochromatic wavelengths from the training source at 0.1 nm intervals.

to take input light from a single-mode fiber for efficient operation, a custom-built input block was used to pre-filter the broadband white light using a set of filters, followed by a beam expander setup to match the free-space beam's divergence to the NA of a single-mode fiber (Fig. 6.4(b)). The monochromator output generated 0.3 nm wide training peaks with a step size 0.1 nm in the range 665-675nm (Fig. 6.4(c)). This light was coupled into the MMI waveguide and the OSA in a similar fashion to the NIR light, generating 1000 MMI images. Then, the supercontinuum light was sent through an acousto-optic tunable filter (NKT SuperK Select) to create the external test source signal (Fig. 6.4(a)). This allowed us to generate test signals with a wider spectrum than the training beam at different wavelength points.

6.3. Narrowband peak prediction and broadband reconstruction in the NIR wavelengths

As discussed in the previous section, we created training images between 793.8 and 795.6 nm with 0.05 nm steps size in several wavelength groups. Then we created broadband spectra from linear combinations of these images with randomly generated amplitudes at each wavelength. This produced an additional 6,000 images. 90% of these images were used for training, while 10% of the images were withheld for testing the CNN prediction performance.

After the training was completed, we first tested the ability of the device to recognize narrowband spectra. To this end, the CNN was exposed to previously unseen images from the test set, and the predicted amplitudes at each of the possible wavelengths were determined. A representative result for a spectrum with a peak at 794.75 nm is shown in Fig. 6.5(a). The gray line represents the spectrum as measured with the OSA. It is virtually indistinguishable from the CNN analysis of the MMI scatter image (red line), showing excellent agreement of both the peak wavelength and the FWHM. We repeated this experiment at each of the 26 wavelengths in our test interval and found an excellent agreement in every case as seen in Fig. 6.5(b), where every CNN-determined wavelength peak location falls within a 0.05 nm band (blue area) of the "True" peak location determined by the OSA. Thus, we find a spectral resolution of 0.05 nm, and equivalently a resolving power of R=λ/Δλ=16,000 in this wavelength range. Resolution and bandwidth are limited by the setup, specifically the finite width

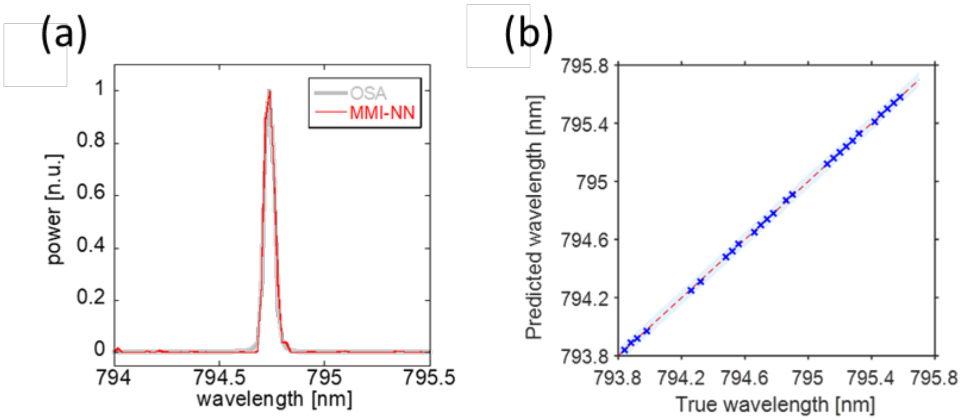

Fig 6.5 MMI spectrometer performance in the NIR wavelengths (a) Comparison of laser spectrum determined from optical spectrum analyzer (OSA, gray line) and neural network analysis of MMI scatter pattern (red line). (b) Reconstructed vs. true peak wavelength of tunable laser spectra, showing a spectral resolution of 0.05 nm as indicated by blue band.

of the training spectra and the tuning range of the laser. We note that, in the telecom wavelength range, this resolving power corresponds to a resolution of 0.1nm, well below the 0.8 nm (100 GHz) spacing between wavelength division multiplexing channels.

We then assessed the ability to analyze broad, continuous spectra. To this end, a test image was generated using a new, linear combination of the test spectra with randomly generated weights. Fig. 6.6(a) shows that the CNN was able to extract the spectrum from this single, composite scatter image with excellent qualitative agreement in recognizing the spectral features and confirming the 0.05 nm resolution with a

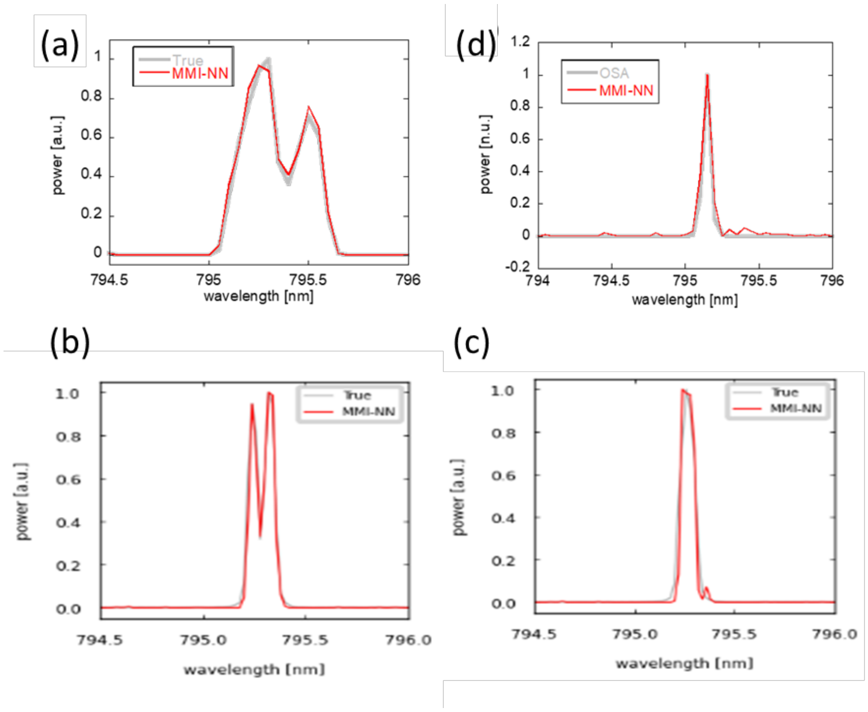

Fig 6.6 (a) Comparison of NN-reconstructed broadband NIR spectrum (red line) with broad spectrum composed of linear combination of single wavelength spectra with different weights (gray line). (b) NN-prediction of broadband signal with two narrow peaks separated by 0.1 nm. (c) Resultant of the addition of two narrowband peaks 0.05 nm apart (gray line) and the NN-prediction (red line) (d) NN-reconstruction (red line) of unseen DBR NIR laser line and OSA reference (gray line).

continuous spectrum. As shown in Fig 6.6(b), a broadband signal consisting of two narrow peaks spaced by 0.1 nm is also reconstructed by the CNN with high accuracy, and the two peaks are clearly resolved. As each of the constituent narrowband peaks used in the broadband spectra generation process has a FWHM (full width half maximum) width= 0.05 nm, an addition of two consecutive peaks spaced by 0.05 nm results in a wider peak, as indicated by the gray line in Fig. 6.6(c). This wider peak is also successfully reconstructed by the CNN model. Finally, we fed light from a different source than was used for generating the training images into the chip. Specifically, we used light from a distributed Bragg reflector (DBR) diode laser (Vescent Photonics). Again, the spectrum was first recorded with a conventional OSA (gray line in Fig. 6.6(d)). Both the peak wavelength at 795.2 nm and the width of the spectrum are identified correctly by the CNN algorithm.

6.4. Performance analysis in the visible wavelengths

With the high-resolution and broadband performance assessments of the MMI spectrometer in the NIR wavelength range determined, we repeated the characterizations in the visible wavelength range around 670 nm using the monochromator setup described in section 6.2 to generate training spectra with 0.1 nm resolution (laser steps). The CNN model trained with the visible wavelength dataset was first tested for the ability to recognize previously unseen narrowband spectra from the laser used for training. The network predicted the peak position and the shape of these spectra with high accuracy across the entire test range, as shown by representative

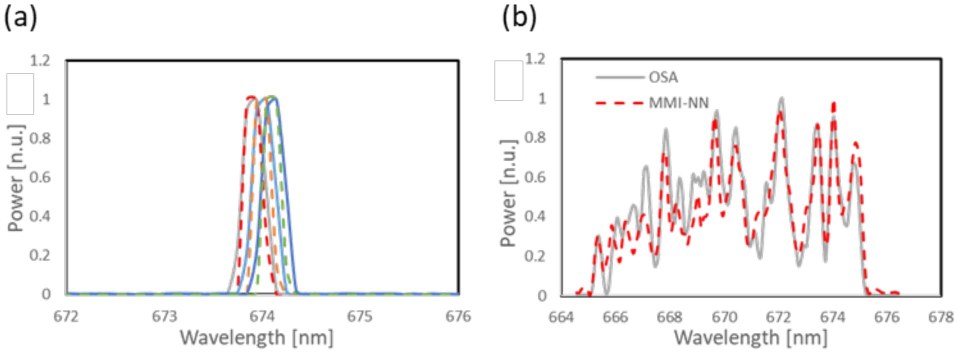

Fig 6.7 MMI spectrometer performance in the visible wavelengths (a) Comparison of laser spectra with peaks at 673.9, 674.0 and 674.1 nm from a commercial optical spectrum analyzer (solid lines) and reconstructed by a neural network from the MMI images (dashed lines). (b) Comparison of a CNN-reconstructed broadband spectrum (dashed line) composed of linear combination of the overlapping single wavelength spectra with different weights (solid line).

results (Fig. 6.7(a)). To assess the ability to analyze broad spectra, a broadband test image was next generated using a linear combination of the narrowband signals, similar to the NIR experiments but with more overlap between the subsequent peaks due to the linewidth of the original laser. The model was able to extract this spectrum with very good qualitative agreement in recognizing the peaks and valleys (Fig 6.7(b)).

Finally, test light from the external, broadband tunable AOTF source with wide, ~1.8 nm FWHM signals at different wavelength points was exposed to the model. Examples of spectrum prediction for this test source are presented in Figs. 6.8(a-b). The spectral shape is recognized with excellent fidelity in all cases. The fitted peak positions, the FWHM of the central peak, and the side lobes agreed well with their true values within the training step sizes limit. As shown in Fig. 6.8(c), the comparison between the Gaussian-fitted peak locations between the predicted and the true spectra across the

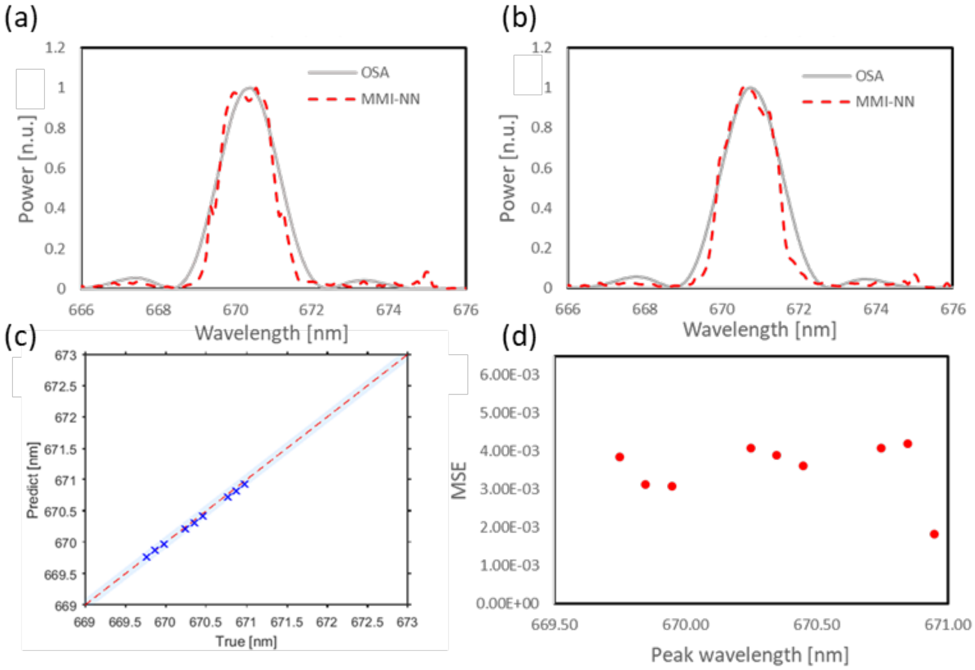

Fig 6.8 CNN performance on an external, unseen light source. (a-b) CNN - reconstructed wideband spectra (dashed lines) of the AOTF filter signals measured at 670.3 and 670.7 nm, respectively. (c) True vs CNN-predicted peak locations of the test signals taken with the external source. The dashed line represents the training range, while the shaded region stretches a region of 0.1nm on both sides, representing the training step sizes. (d) MSE errors of the test signals reconstruction by the CNN.

tested wavelengths show close match. The mean squared error (MSE) value for a prediction instance can be defined as:

$$MSE = \frac{1}{N}\sum_{\lambda}\left[I_{true}(\lambda) - I_{predict}(\lambda)\right]^2 \tag{6.3}$$

Here, $I_{true}(\lambda)$ and $I_{predict}(\lambda)$ are the true and CNN predicted spectral intensity vectors and N is the length of each vector. The MSE values for all the predicted spectrums from the external, broadband AOTF source are shown in Fig. 6.8(d) and are close to the network performance limit, i.e. observed MSE from a typical training and validation dataset (see chapter 7 for an example of MSE evolution for training and validation datasets).

Chapter 7: Spectral reconstruction using convolutional neural network (CNN)

For the MMI spectrometer data analysis and spectral reconstruction, we used a supervised machine-learning technique to predict the present spectrum in the input light. As briefly discussed in chapter 6, we first collect single wavelength images and then generate a huge dataset of various combinations of mixing these single-color images to train a NN model using this dataset. This enables training a model by using only a single wavelength-tunable light source and using it for single wavelength and broadband spectroscopy. In a recent work on a reconstructive spectrometer with multimode fiber [272], the researchers used a classification model to pick the single wavelength present, i.e., the network is trained to only pick a single class (peak wavelength) among all possible options. This is similar to many classic multi-class problems in neural network analysis [273]. Thus, this approach can only verify the presence of a single wavelength. We take a different approach and view the task of analyzing the continuous spectra consisting of different signal amplitudes over a given wavelength range as a regression problem. In regression problems, the "true output values" are important, and for a spectral analysis, this means the relative height of each data point in a spectrum.

More specifically, we use convolutional neural networks (CNNs), a special class of supervised learning technique to analyze the MMI images taken at different wavelengths. A CNN model applies multiple 2D filters to the image to extract local spatial features. Then these extracted features are mapped into a 1D array with spectral data points. Compared to a straightforward dense neural network (DNN), CNNs are better suited for high-dimensional image processing without losing information [274]. In our case, it also facilitates training over a large, augmented dataset using a finite number of monochromatic laser wavelength points for more generalized, robust performance. The CNN model is trained to predict an output spectral vector with continuous relative values of all data points from a given input image. By feeding randomly selected and weighted peaks as composite spectra into the CNN model during the training step, the model is exposed to several possible variations and combinations of broadband patterns [275]. Finally, as conceptually shown in Fig. 6.1 of the previous chapter, the CNN is tasked to reconstruct the spectrum of any light source coupled into the chip. In the following sections, we discuss nature and dimensions of the CNN's input and output as well as the hidden layers, followed by some considerations for hyper-parameters selection and the training process.

7.1. Different layers of the CNN

(a) Input: For the CNN analysis, the input (image) array has a dimensionality equal to the cropped MMI scatter image, a selected region of interest (ROI) of 1200x120 pixels. The size of the selected ROI is decided based on the computational capacity of the hardware. Choosing a small ROI can lack enough information for training a high-performance CNN model, while bigger ROIs require more processing power and storage space. Each pixel element has a normalized value between 0 and 1 (1 being the brightest pixel). Examples of the ROI patterns on the MMI waveguide excited at 0.1nm shifted wavelengths in the visible spectrum are shown in Fig. 7.1, showing distinct feature differences (a smaller 220x120 pixels ROI is chosen for a closer view). Another important attribute is that this model works with greyscale 2D image inputs, while

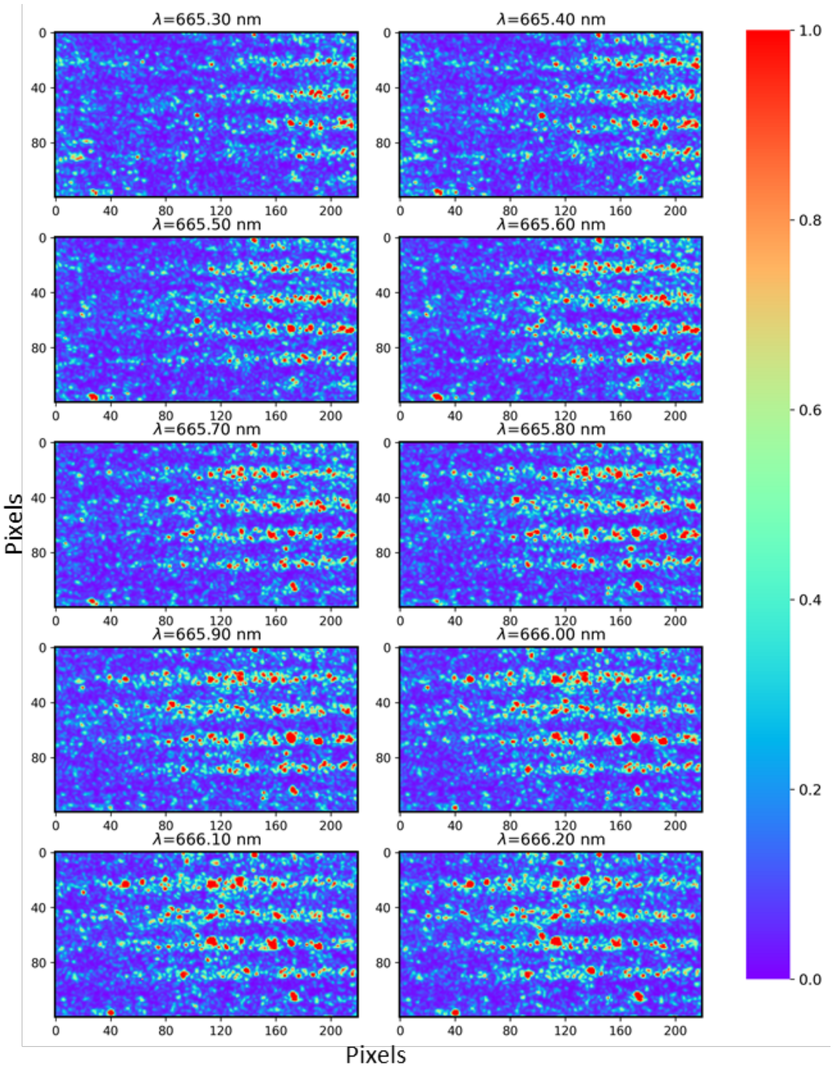

Fig 7.1 Top-down patterns from the MMI waveguide at different wavelengths. Monochromatic 2D MMI intensity patterns within a 220 x 120 pixels region of interest taken over a 1 nm bandwidth at 0.1 nm wavelength steps, showing the evolution of the pattern lines as well as their interaction with the nanoscale surface features.

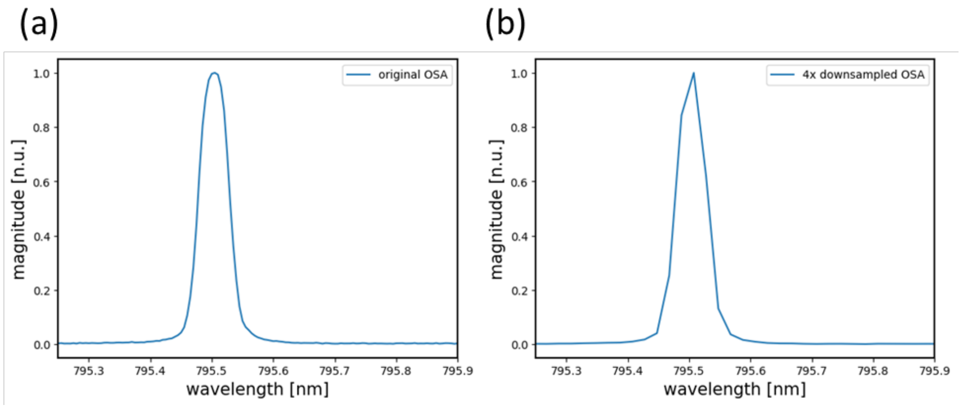

Fig 7.2 An initial NIR narrowband spectrum measured by the OSA with 0.005 nm sampling interval. (b) 4x downsampled spectrum (sampling interval=0.02 nm).

typical classification CNN models are usually designed for RGB images and have a 3D input matrix.

(b) Output: The training output vectors are originally collected using the commercial OSA. At the same time, the training images are captured with an original sampling interval of 0.005 nm. For the NIR wavelength experiment, we collected data points in the range 793.0-797.0 nm and reduced it to a smaller vector by downsampling by a factor of 4, as shown in Fig. 7.2(a-b). This ultimately results in an output shape of 200 points with 0.02 nm sampling interval. This final output dimension is set based on the resolution and bandwidth of the spectrometer, with the goal of reducing hardware workload without compromising the performance. The achievable step size from shifting the tunable laser, the original linewidth of the tunable laser, and the smallest linewidth the OSA can read are the most crucial limiting factors on the resolution (smallest peak separation the MMI spectrometer can distinguish). The last one also sets an upper limit on the sampling interval of the CNN output labels. Conversely, sweeping a large bandwidth using the training laser while keeping the same, fine sampling interval will increase the number of sampling points (length of the output vector). The visible wavelength output labels span the range 664.5-676.5 nm in 0.1nm interval. In principle, very high resolution over an increasingly larger bandwidth can be simultaneously achieved, if enough computing power is available.

(c) Hidden layers: For this study, we used a simple CNN framework with a single 2D convolutional layer followed by three fully connected (dense) layers. The convolutional layer scans through the ROI with small kernels (20x20 pixels) using 512 filters. As mentioned earlier, analyzing a bigger ROI requires a bigger memory space and processing unit, so we further reduced the processing load by using a relatively large stride (the number of pixels by which a filter moves across the input image during the convolution operation) size of 15x15 pixels for the convolutional layer. The tradeoff of this change is losing some fine-grain detail affecting the reconstruction accuracy, but negligible effect is observed in our scope of works. For the dense layers, the number of neurons in each layer depends on the sizes of its input and output. As a simple design rule of thumb, we set the output lengths in the dense layers at a proportional ratio (1:2:1) to the final layer output, i.e. the predicted spectrum.

Fig. 7.3 illustrates the CNN model used for the experiment in the NIR wavelength range. In total, 56,993,312 parameters are trained. The CNN model for the visible wavelength experiment is slightly smaller with 34,239,712 parameters, owing to a coarser output vector which is a reasonable choice due to the coarser step sizes from the visible light source.

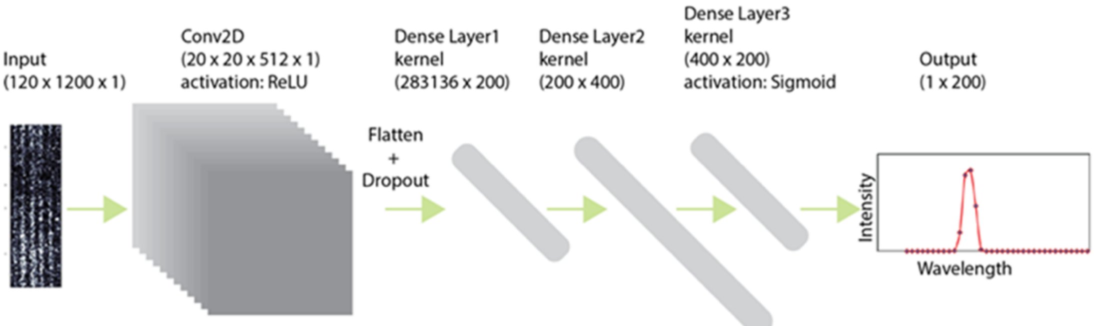

Fig 7.3 Convolutional neural network (CNN) architecture. 120x1200 pixels input image is fed into the network in a batch size of 50 images. The network starts with 512, 20 x 20 convolution kernels scanning over the image with strides= 15 x 15, followed by a rectified linear unit (ReLU) activation layer to generate a pool of features. Preceded by flattening of the convolution block output and a dropout process, the output length of the three dense layers depends on the final output length in the ratio 1:2:1, shown in this case shown for a 200 points long output spectrum. The Sigmoid activation in the final layer decodes the final output to be normalized into predicted 1D spectrums.

7.2. Hyper-parameters and the training process

(a) Activation functions: As shown in Fig. 7.3, we used a "Rectified Linear Unit" (ReLU) activation function for the 2D convolution layer, followed by linear activation functions for the next 2 hidden layers, and sigmoid activation function for the last layer nodes. The sigmoid activation function in the last layer is a unique implementation, since it is not very common in conventional classification problems. Since the spectral reconstruction is a regression problem and the predicted output (intensity value) at a data point is expected to be a bound, continuous, normalized number, we used the sigmoid activation function.

(b) Optimizer: In a neural network, a model is trained on a training dataset that accurately represents the test data on which model will be used. This training is an optimization process in which a loss value, or, more conventionally, a cost function has to be minimized. Depending on the type of data and output performance, different optimizers can be selected for an application. For training our particular CNN model, we utilized the Stochastic Gradient Descent (SGD) optimizer with a learning rate equal to 0.3 (another hyper-parameter that can speed up or slow down the training and can significantly impact the CNN performance), and a mini-batch size of 50.

(c) Loss function: This is the core performance monitor for the training and validation process of our CNN. In a typical classification problem, the loss function is a cross-entropy function defined as:

$$L = -\frac{1}{N}\sum_{i=0}^{N-1}\sum_{k=0}^{C} y_{i,k}\log\left(p_{i,k}\right) \tag{7.1}$$

Where $p_{i,k}$ is the probability value of sample i from the training dataset belonging to class k. In contrast, to reconstruct a continuous spectrum from an input image, we use the mean squared error (MSE) as the loss function L defined as:

$$L = -\frac{1}{N}\sum_{i=0}^{N-1}\left(y_{i,true} - y_{i,predict}\right)^2 \tag{7.2}$$

Here, $y_{i,true}$ and $y_{i,predict}$ are the true spectrum and the predicted network output, respectively for sample i from the training dataset. y is a normalized, 1-D array with $M = \frac{\lambda_{end}-\lambda_{start}}{\Delta\lambda} + 1$ number of data points, with $\Delta\lambda$ as the sampling interval of the downsampled OSA spectrum. Note that this loss function is the same performance metric MSE used for individual test cases in section 6.4, and will be used further in chapter 9.

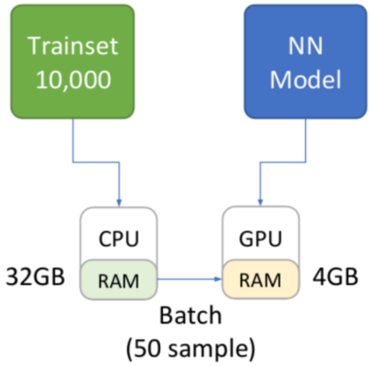

Fig 7.4 Loading of images in batches by the 32 GB RAM+CPU into the 4 GB GPU during the CNN training process (image courtesy: V. Ganjalizadeh).

(d) Early stopping: This early stop function (provided in TensorFlow library) helps to prevent overfitting of the NN model. Overfitting results in a less robust model and can cause noisy outputs. Once the training is completed, we store the model into the disk to load and use later on any given new (unseen) data.

(e) Batch size: By default, an optimizer in a NN tries to load the entire model parameters and the training dataset into the GPU memory to speed up the training processing. But, fitting the entirety of the massive training dataset simultaneously with the initial NN parameters into the GPU can be a heavy process, and can ultimately hog up the processing power. Fig. 7.4 shows how CPU loads the training dataset into the system memory (RAM) and feeds them in small batches (50 images used in our case) during the training into the GPU.

(f) Epochs: This is the number of passes of the entire training dataset across the CNN, i.e. the number of times every training example in the dataset has been seen by the CNN. For most cases, we used an epoch limit of 1000, by which the network converges well (very low, and similar loss values for the training and validation datasets). For a

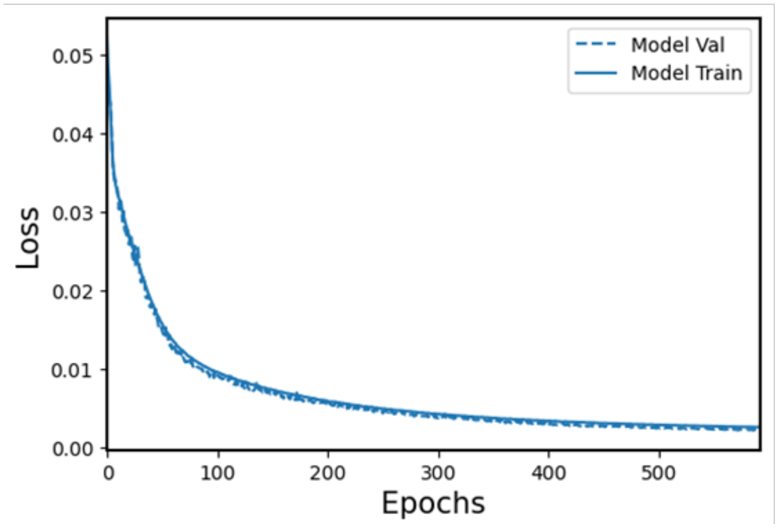

Fig 7.5 Training and validation dataset mean-squared errors (MSE) of the model as a function of the number of passes of the dataset (epochs) through the network. In this case, good convergence is reached in about 500 epochs, but the process can run longer if there are more variations and fluctuations in the data.

very clean dataset with very little image variations for the same wavelength, and larger laser steps, the CNN can actually stop before it reaches this limit.

Throughout the training process, the loss values for both the training and validation datasets exhibit similar trajectories and converge to comparable values by the end of the process, as seen in Fig. 7.5. The entire framework is implemented in Python using the TensorFlow machine learning library and is run on a desktop machine with NVIDIA P1000 4GB GPU.

Chapter 8: Novel applications of MMI spectrometer

Based on the performance parameters for the MMI spectrometer established in chapter 6, here we demonstrate the future potential of the MMI spectrometer for three novel application cases. The first demonstration involves a 4x4 spectrometer array. In this implementation, 4 MMI waveguide spectrometers on a single chip analyze light from four independent fiber-coupled sources simultaneously with uncompromised performance. Apart from the performance validation for an array waveguide chip, this also shows future design improvement opportunities, such as creating an ultra-compact spectrometer chip and the distributed use of a calibration laser source and the imaging sensor, as it will be clearer in the following discussion. Thus, the overall scalability of this approach becomes very evident.

The second application is the use of the device as an astrophotonic instrument. Sunlight captured by a telescope is introduced into a silicon-based spectrometer chip at the nanowatt power level, and the continuous, broadband spectrum is identified using a convolutional neural network. The spectral characteristics of sunlight and scattered skylight, along with their variations due to factors such as time of day, season, latitude, altitude, and atmospheric conditions, are crucial for climate monitoring and understanding their impact on various plant and animal species [276]. Depending on whether it is observed from the ground, the upper atmosphere, or the deep space, spectroscopic monitoring of the sun provides valuable information on the chemical composition of the sun, the routine or irregular solar events, and the atmospheric variations of the earth. However, such frequent and close monitoring can be an expensive endeavor with the currently commercially available bulky spectrographs. The MMI spectrometer can be a cheaper, simpler, more compact alternative for day-to-day high performance analysis necessary in the related applications.

The third application is based on our ongoing efforts to integrate the MMI spectrometer chip with the adaptive optics (AO) system of the 3 meter Shane Telescope at Lick Observatory, San Jose, CA. The ultimate goal is to combine the light collection capacity of this telescope with the MMI patterns on our compact chip for spectroscopic analysis of distant astronomical objects. Because the different combining elements of this endeavor (telescope-fiber coupling, fiber-chip coupling, camera efficiency etc.) are still being continuously improved, the successful "first light" into the MMI result is yet to be reported. Bu this chapter will try to highlight the early efforts and results on our astrophotonic instrumentation at Lick, and lay out the challenges and possible solutions for the next phase of the project.

8.1. MMI spectrometer array

In this section, we turn our focus toward a major advantage that the chip-scale photonic integration offers to open new avenues for applications. The planar and linear nature of the MMI waveguide architecture naturally suggests the addition of multiple waveguides to form highly compact spectrometer arrays. We demonstrate this concept with a 4x4 (4 inputs, 4 MMI sections) spectrometer array that is designed to interface with off-the-shelf photonic components. Fig. 8.1(a) illustrates the concept of coupling

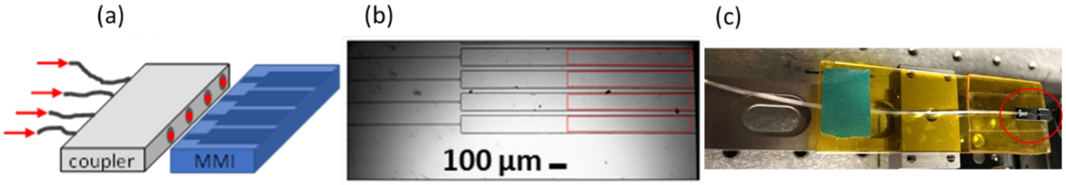

Fig 8.1 (a) Conceptual illustration of four independent signals fed into an MMI spectrometer array chip via commercial fiber coupler. (b) Microscope image of a 4x4 MMI spectrometer array. The red rectangles denote the image areas used for individual CNN training and testing. (c) Photograph of the commercial OzOptics fiber array chip (circled in red) on a glass slide.

a commercial 4x single mode fiber (SMF) coupler array (OzOptics SM fiber V-groove assembly) to the spectrometer chip. This fiber array is commonly used with planar lightwave circuit (PLC) splitters and wavelength division multiplexing (WDM) components in fiber-optic networks. Here, it is aligned with the 4x4 MMI spectrometer chip, and the four independent fibers are simultaneously excited with four laser signals (red arrows). The commercial fiber coupler terminates in four single-mode fibers that are arranged on an array of V-groove slots with 127.5 μm spacing on a silicon chip. Consequently, we designed and fabricated an arrayed MMI spectrometer chip in which four input waveguides have the same spacing, each leading to a separate MMI section. A photograph of the MMI waveguide group is shown in Fig. 8.1(b). Fig. 8.1(c) shows the fiber V-groove array chip (circled in red) sitting a custom-built platform using two glass slides. A more detailed description of the setup and experimental procedure is provided in the following section.

8.1.1. Data acquisition setup

For this arrayed spectrometer experiment, we used the Ti:Sapphire laser used for the NIR experiments. But this time, the peak wavelength was tuned by 1 nm steps over a larger bandwidth of 774-813 nm. This is achieved by rotating a birefringent Lyot filter inside the laser cavity and creating cavity resonances at discrete wavelengths [277]. Light is split into 5 separate paths using a series of beam splitters. The first four beams get coupled into each of the fiber in the V-groove array, and the other beam going into the OSA using a separate single mode fiber (Fig. 8.2(a)). The input power going into each MMI spectrometer was adjusted to be similar using optical attenuators. The actual light path and optical assembly for input coupling into the four arrayed fibers is shown in Fig. 8.2(b). An image of the coupling between the fiber V-groove array and the MMI spectrometer array is shown in Fig. 8.2(c). All four MMI sections were then simultaneously excited by four independent input signals, and a single camera image

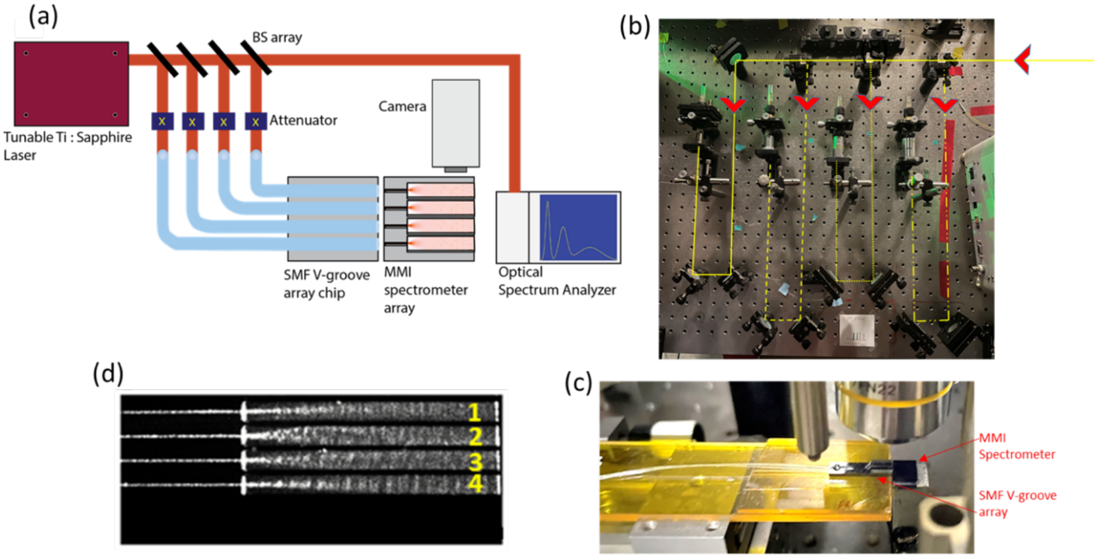

Fig 8.2 (a) Conceptual details of the optical setup to implement an arrayed spectrometer operation. To keep the pixel intensities similar among the spectrometers, the amount of input light in each fiber of the V-groove is regulated using an attenuator. This prevents the oversaturation/ under-saturation in any certain ROI on the MMI spectrometer arrays imaged in a single snap. (b-c) Coupling arrangements on the two sides of the commercial fiber V-groove array. (b) Optical assembly and light path for coupling into the four fanned-out branches of the single-mode fiber array. (c) The other end, i.e., the fiber chip is edge-coupled to a MMI spectrometer array. (d) Camera collected scattering image from all four MMI spectrometers.

was taken to record all four spectra in one image (Fig. 8.2(d)). A total of 1,120 training images were taken, which were then split into 4 different regions of interest (red boxes in Fig. 8.1(b)), each representing one of the four MMI spectrometers.

8.1.2. Performance analysis

The first thing to note in the example scatter image in Fig. 8.2(d) is that the scatter patterns slightly differ between the MMIs due to random variations in surface roughness and slight alignment differences, even though they are imaged with the same input light wavelength and have the same nominal waveguide dimensions. However, as each MMI spectrometer was trained individually over a region of interest (ROI) marked with red rectangles in Fig. 8.1(b), this pattern variation is not an issue for the current scheme. When separate CNN analysis was carried out for each waveguide with

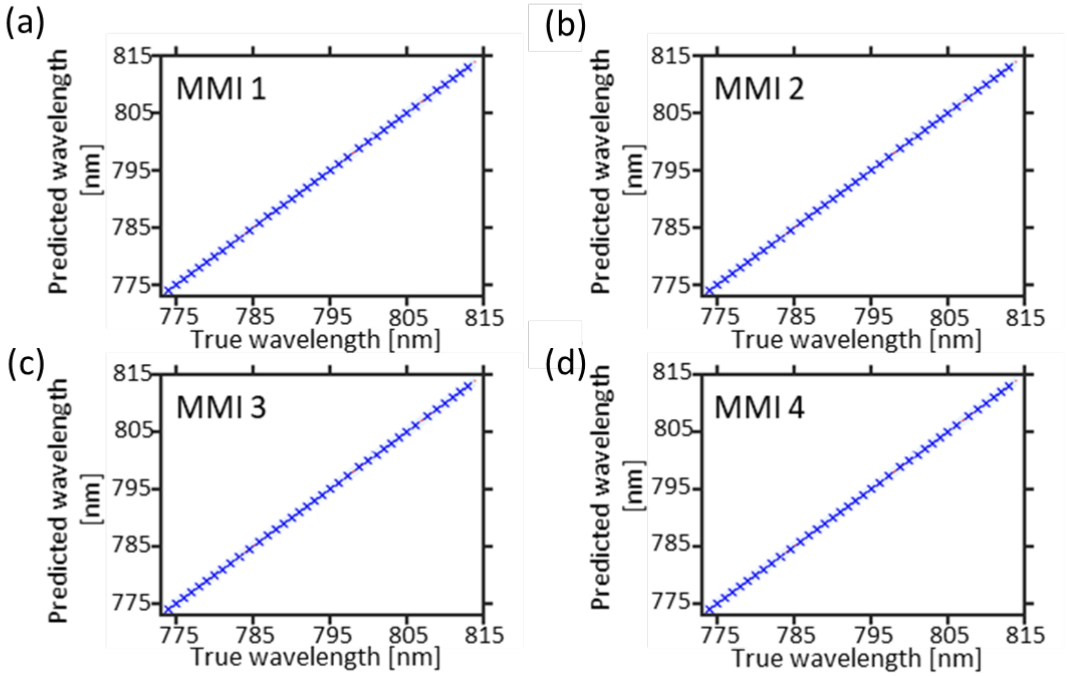

Fig 8.3 (a-d) Accuracy and resolution of the four spectrometers (marked as 1 to 4, respectively in Fig. 8.2(d)) after being individually trained by neural networks.

unseen images at different wavelengths similar to the experiments in chapter 6, all four MMI spectrometers showed the similar, uncompromised performance as seen in Figs. 8.3(a-d). Each was capable to correctly identify the peak wavelength of the input signal across a 40 nm bandwidth covered in 1 nm steps. These results show that expansion of the MMI spectrometer device into highly multiplexed arrays is straightforward as no additional fabrication step is required. Furthermore, as we will demonstrate in chapter 9, it is feasible to train the MMIs in an arrayed implementation with the same or different power levels, and, in a practical application, separate test sources at different power levels can have very similar prediction performances down to sub-nanowatt level without having to "equalize" the power level into each of the MMIs.

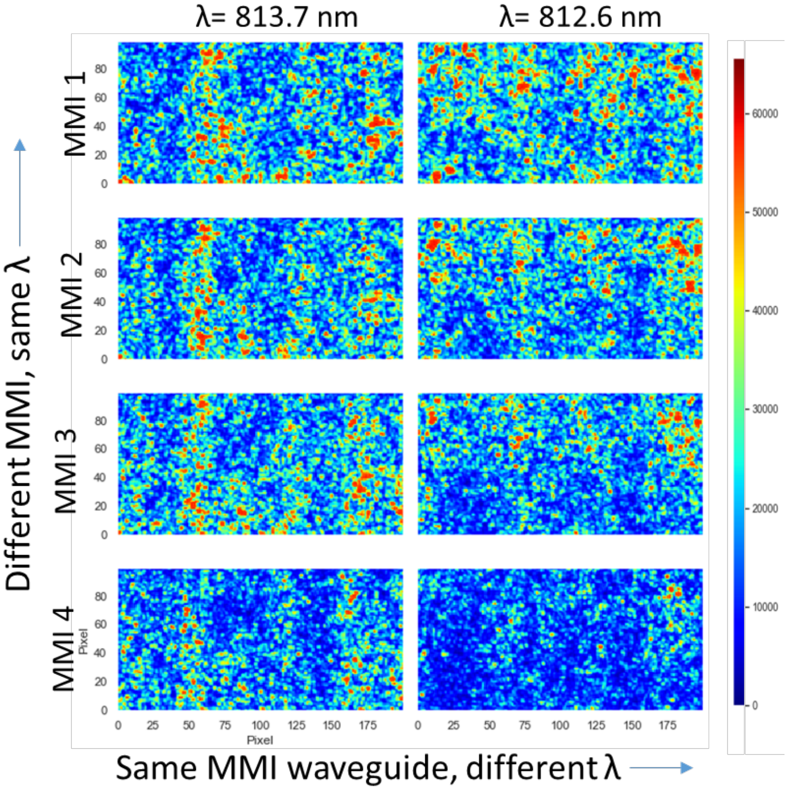

Fig 8.4 Comparison of MMI patterns among different waveguides for two example wavelengths.

The arrayed MMI waveguides, if fabricated under ideal conditions, is expected show the same, deterministic interference pattern for the same wavelength. This would mean that a CNN trained on any of these waveguides should also perform accurately on the datasets acquired from any of the other waveguides in the array. However, due to the randomness of the plasma etching processes and the input waveguides being slightly larger than perfectly single-mode conditions, the MMI patterns between the tested waveguides vary slightly, as illustrated in Fig. 8.4. As a result, our current efforts of training a CNN model on only one waveguide for as-is universal application on all the other waveguides did not show promising results. Some example case prediction cases are shown in Figs. 8.5(a-d), where the network trained on the image dataset from MMI4

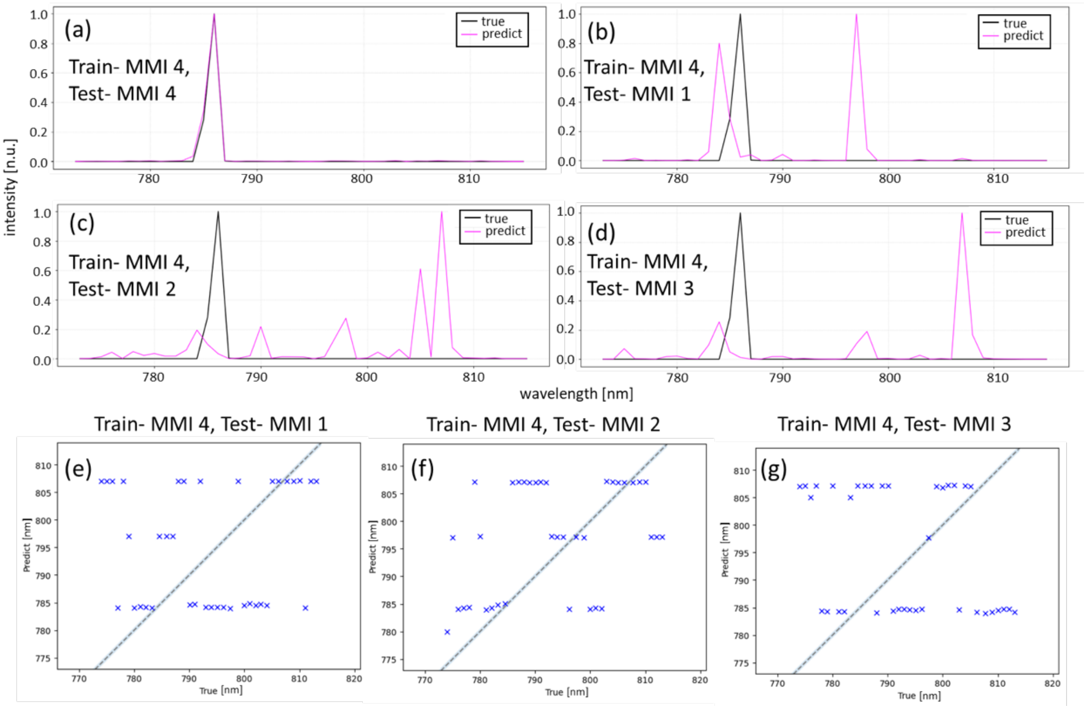

Fig 8.5 (a-d) Example performances of the CNN model trained on the dataset from MMI 4 on test images taken on MMI waveguides 4, 1, 2, and 3, respectively. (e-g) True peak locations of all the test wavelengths in the spectrometer range vs predicted peaks by the CNN model trained on MMI 4 based on test images from MMI 1, 2, and 3, respectively.

fails to reconstruct the correct spectrum from the test image dataset taken from the other waveguides. The true peak vs predicted peak locations for test samples across the entire training bandwidth for this approach are shown in Figs. 8.5(e-g), where the CNN model was trained on MMI4 and tested on MMIs 1, 2, and 3, respectively. Except a few cases, the network fails to recognize the location of the peaks, and the current performance is non-satisfactory. However, more advanced neural network training techniques, for example, transfer learning, can be employed. Using this approach, it is possible to train a starting CNN model on one MMI waveguide, freeze a few chosen core network layers, and train the rest of the layers with the dataset from another MMI waveguide to get a second CNN model [278]. This can significantly reduce the computational cost and power compared to training four completely separate CNN models.

The 4x4 MMI spectrometer array takes up a chip area of only 0.5 x 5 mm^2, and numerous implementations of this concept can be envisioned. Example applications could be feeding signals from different sources into an NxN array, or building 1xN arrays in which a single input signal is distributed into N spectrometer sections that could be lithographically integrated with active photonic components on a photonic integrated circuit (PIC) and functionalized for different purposes. For the device dimensions used in this experiment, N (the number of spectrometers on a chip) can be >750 across the diameter of a commercial 4-inch wafer. The training images for all waveguides were recorded simultaneously, thus significantly reducing the calibration data acquisition time. However, a CNN model had to be trained separately for each waveguide. In order to minimize training time and scale to large array sizes, the fabrication can be optimized to produce more uniform waveguides. With the help of more advanced image filtering and NN architecture, a single network can be used with an array of such high-quality waveguides to create a very compact, parallel analysis scheme.

8.2. Broadband sunlight spectral analysis using MMI spectrometer

In this and the next section, we illustrate the versatility of the MMI spectrometer and its potential for use in a wide range of research and technology applications, particularly in astronomical observations. The first of these is solar spectrum analysis from a ground-based observation, which plays a crucial role in various scientific and practical fields [279]. For example, on top of elemental analysis of the sun's atmosphere (hydrogen, helium, trace metals etc.), spectroscopy plays a crucial role in monitoring solar activities, e.g., sunspots [280], solar flares [281], and coronal mass ejections [282]. Another important application is studying the earth’s atmosphere. Sunlight passing through the earth's atmosphere gets absorbed and scattered by different atmospheric gases. By analyzing these changes in the solar spectrum, researchers can determine the concentration of gases like ozone, water vapor, oxygen, carbon dioxide, and different greenhouse gases [283]. These play important roles in understanding climate change and atmospheric pollution. Apart from that, solar spectroscopy is becoming increasingly important in many recent technological developments, e.g. solar cell optimization [284]. Currently, different specialized field spectroscopy instruments (spectroradiometers) appropriate for solar spectroscopy are offered by companies like Apogee Instruments [285], JETI [286] etc. using conventional technologies. We used our integrated MMI spectrometer to analyze a filtered out solar spectrum in the NIR wavelength range. In the following section, we discuss the experimental setup and the observations of this experiment.

8.2.1. Data acquisition setup

To establish a proof-of-principle demonstration of the suitability of our integrated MMI spectrometer for such applications, we set up a solar observation experiment as shown in Fig. 8.6(a). Sunlight collected with a small 72 mm telescope (Astro-Tech AT72ED)

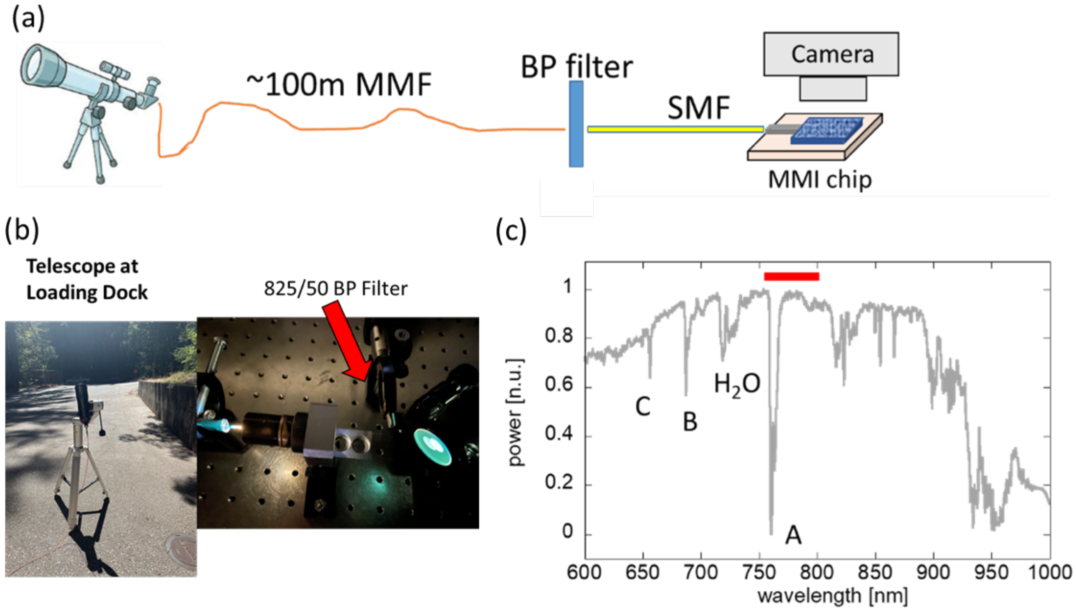

Fig 8.6 (a) Schematic view of the setup to analyze the solar spectrum on the MMI spectrometer chip. (b) Left panel: Collection of sunlight using the telescope and the multimode fiber. Right panel: Unfiltered sunlight flux output of the multimode fiber inside the dark lab room. The optical filter is temporarily removed to optimize the telescope-multimode fiber coupling. (c) Full solar spectrum recorded with OSA at the single mode fiber output (labels: Fraunhofer lines, red bar: spectral range selected by the bandpass filter in this experiment.)

was captured with a multimode fiber (MMF) with 200 μm core diameter placed in the focal plane of the instrument. Approximately 100 m of MMF was used to guide the sunlight to the MMI spectrometer lab setup (Fig. 8.6(b)) where it is recoupled into a single-mode fiber (SMF) both with and without a 50 nm bandpass (BP) filter centered at 775 nm. The SMF was then coupled into an OSA or the MMI chip for spectral analysis of the solar spectrum. The solar flux was imaged at the MMI at 10 seconds exposure time. The training dataset for the sunlight characterization experiment was created with the help of an in-lab quasi-monochromatic tunable light source (NKT SuperK Select) sweeping the range 752-802 nm in 1 nm steps, and imaged with the same exposure time. As mentioned in the previous section, this AOTF filter output has slightly wider peaks compared to the previously used Ti:Sapphire laser and so is better suited for approximating a broadband spectrum within the same range. Fig. 8.6(c) shows the OSA recording, showing characteristic Fraunhofer absorption lines in the solar spectrum [287]. The red bar shows the portion of the spectrum that is transmitted through the bandpass filter.

8.2.2. Detecting absorption dips in the solar spectrum

After the acquisition of the solar spectrum (Fig. 8.7(a)) and the training images, the CNN was trained in reconstructing a broad spectrum with ‘absorption dips. We created a training dataset by combining the sunlight MMI image with the ‘negative’ of the single-peak image. In the spectral domain, this amounts to the subtraction of laser spectra at different points to create a multi-dip resultant spectrum. Afterwards, the

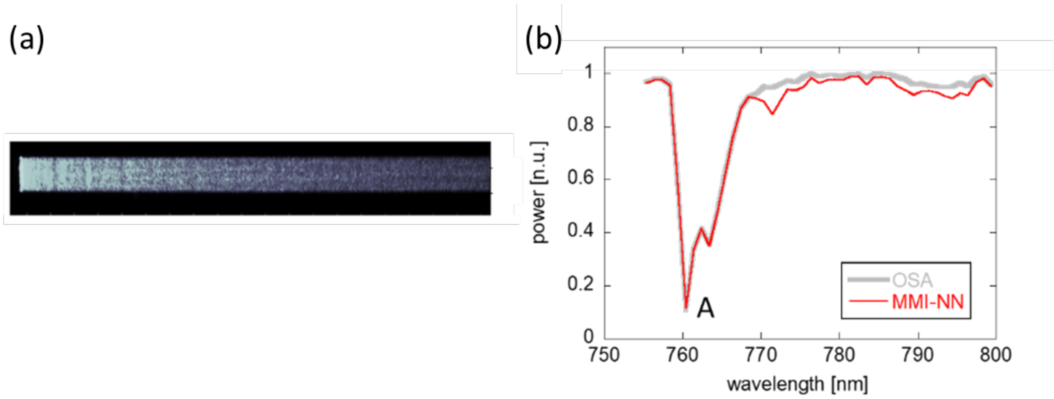

Fig 8.7 (a) MMI scatter pattern of sunlight recorded with 50 nm bandpass filter. (b) CNN-reconstructed solar spectrum (red line) and bandpass-filtered OSA reference spectrum (gray line) around the Fraunhofer A line.

network was exposed to an unseen scatter image of the pure sunlight spectrum shown in Fig. 8.7(b) (gray line), and the resulting spectrum (red line) reproduced the solar spectrum and the Fraunhofer A line (absorption from terrestrial oxygen) very well [288]. This solar analysis implementation shows that the MMI spectrometer has the potential for successful implementation into more challenging applications, for example, integration with larger telescopes for starlight for analysis [289], as discussed in more detail in the next section. This demonstrated capability of identifying spectra from remote sources can also be applied in numerous other scenarios, including environmental monitoring of pollutant gases [105] or the chemical analysis of aerosols [290].

8.3. Integration of MMI spectrometer into the Shane telescope

As discussed in Chapter 5, there is a pressing need for advancements in spectroscopic instrumentation in astronomical observations, or more specifically in ground-based telescopes. For example, multi-object spectrographs, such as DESI, Subaru's Prime Focus Spectrograph, and Keck-FOBOS are bringing multiplexing of up to 5000 fibers to 4-10m telescopes over the next decade. These instrumentation projects are expected to provide insights on cosmology and galaxy formation with multi-year campaigns to collect ~10^7 spectra [197]. The astronomy community has started to recognize the potential of photonic technology to solve the need for scalable, cheap spectroscopic instruments and other challenges as described in a recent astrophotonics roadmap [199]. Our MMI spectrometer provides a promising solution based on its resolving power $\lambda/\Delta\lambda$=16,000 and its multiplexing ability. Its current resolution is ideal for stellar studies [291], observations of very small galaxies (with 5-10 km/s dynamical speeds) as a probe of dark matter density profiles [292], and, optimized at somewhat lower resolution, for surveys of galaxies [196]. For the proof-of-concept astronomical observation with the MMI spectrometer, we have been working on its integration with

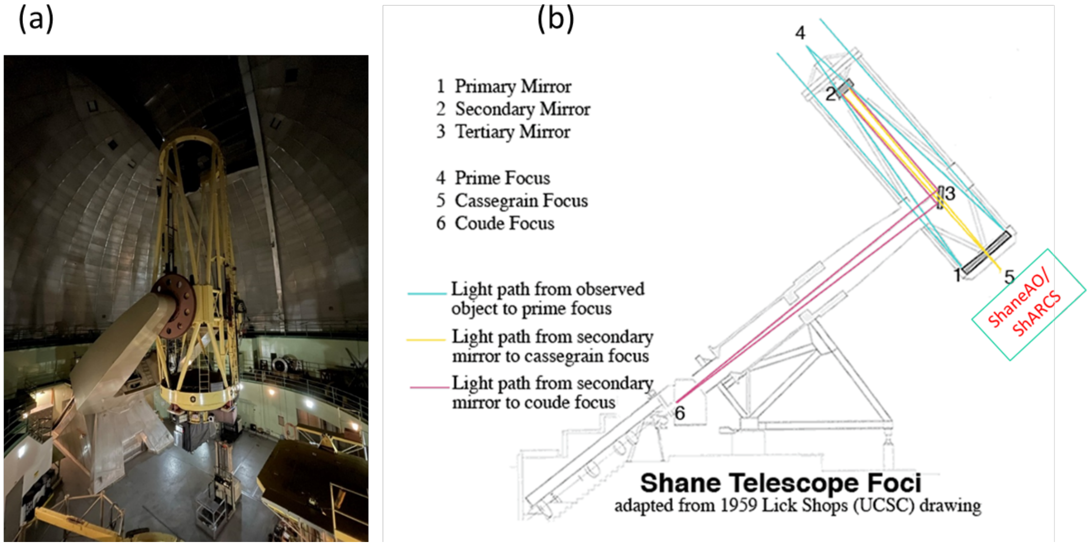

Fig 8.8 (a) The 3-meter Shane telescope (b) Simplified ray diagram inside the telescope, also showing the three focal planes where light can be collected, and the position of the adaptive optics (AO) system (adapted from lickobservatory.org).

the adaptive optics system at the 3 meter Shane reflecting telescope in San Jose, CA (Fig. 8.8(a)). In this section, we will describe the initial roadmap of this astrophotonic integration project, the strategy for efficient beam guiding from the telescope focal plane to the chip, and some of the early efforts at detecting starlight signal from the MMI.

As shown in Fig. 8.8(b), the telescope is constructed around a 3-meter primary mirror. Light can be focused at three different locations (foci) along the length of the telescope: prime focus, Cassegrain focus, and coudé focus. The Cassegrain focus is located at the bottom of the telescope, just below the primary mirror. Light entering from the top bounces off the primary mirror, and then reflects off a secondary concave mirror near the prime focus at the top to finally arrive at the Cassegrain focal plane. The Shane adaptive optics (AO) system (Fig. 8.9(a)) is located behind this position and compensates for the distortions due to atmospheric turbulence that causes stars to twinkle and blurs the images through the telescope. The AO system works by the use of a pair of MEMS based deformable mirrors as seen in Fig. 8.9(b) to perform rapid corrections to the image, and in the case of fiber collection, to shape the beam approximately to a Gaussian spot at the focal plane of the ShARCS spectrograph [293]. The ShARCS camera can take images with a number of near-infrared filters. Because of our current interest in the visible wavelengths. The optical assembly of the AO system, as shown with a simplified diagram in Fig. 8.9(c), creates an f/28.5 beam with ~10 mm spot size right at the entrance slit of the spectrograph. Our collaborators in the UCSC Astronomy Department have developed a photonic lantern injection unit (PLIU)

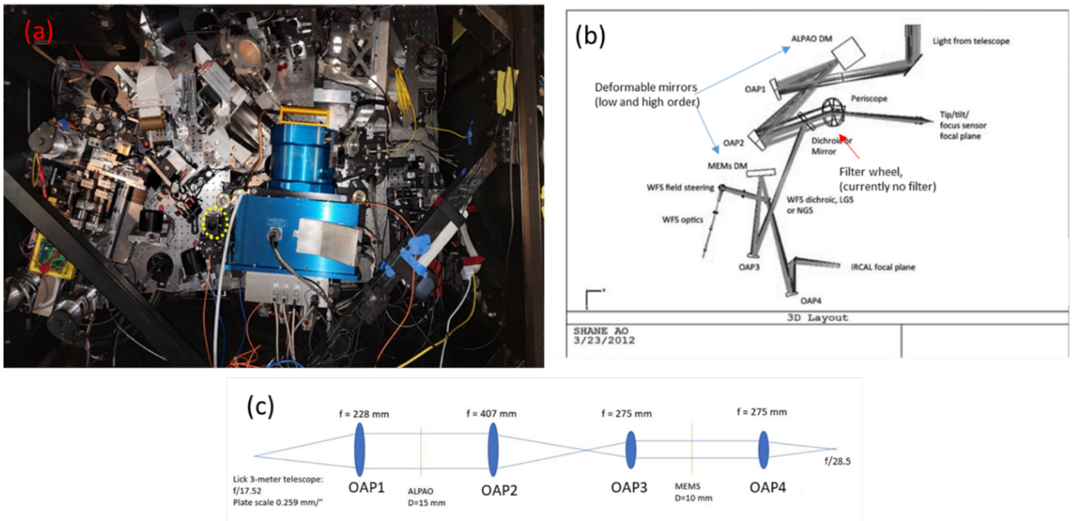

Fig 8.9 (a) Inside of the Shane AO system bench. The yellow circle indicates the entrance slit of the ShARCS spectrograph (blue box), where we pick off the light from focal plane to collect into a multimode fiber. (b) Optical design of the Shane AO system (adapted from [293]) (c) Simplified optical beam approximation of the AO system (image courtesy: M. DeMartino.)

as shown in Fig. 8.10(a) [217], a slightly modified version of which is used to couple light from this focal plane into a 200 μm multimode fiber (MMF). We have tested different coupling options between the MMF and the chip. An overview of the experimental setup used on the latest observation night at Lick on November 1st, 2023 is shown in Fig. 8.10(b), indicating the positions of our two modular boards on the AO system table, the MMF to single mode fiber (SMF) coupling board and the chip imaging microscope board. In Fig. 8.10(c), a close-up view of the lensed coupling between the MMF and the SMF is shown. This setup was measured to have an SMF throughput of 1.75% (ratio of power before the 40x objective and at the SMF output) at 633 nm light in the laboratory testbeds. For stable coupling between the SMF and the MMI chip during the telescope's movement, our group is exploring avenues such as gluing the SMF to the MMI chip and has seen some initial success.

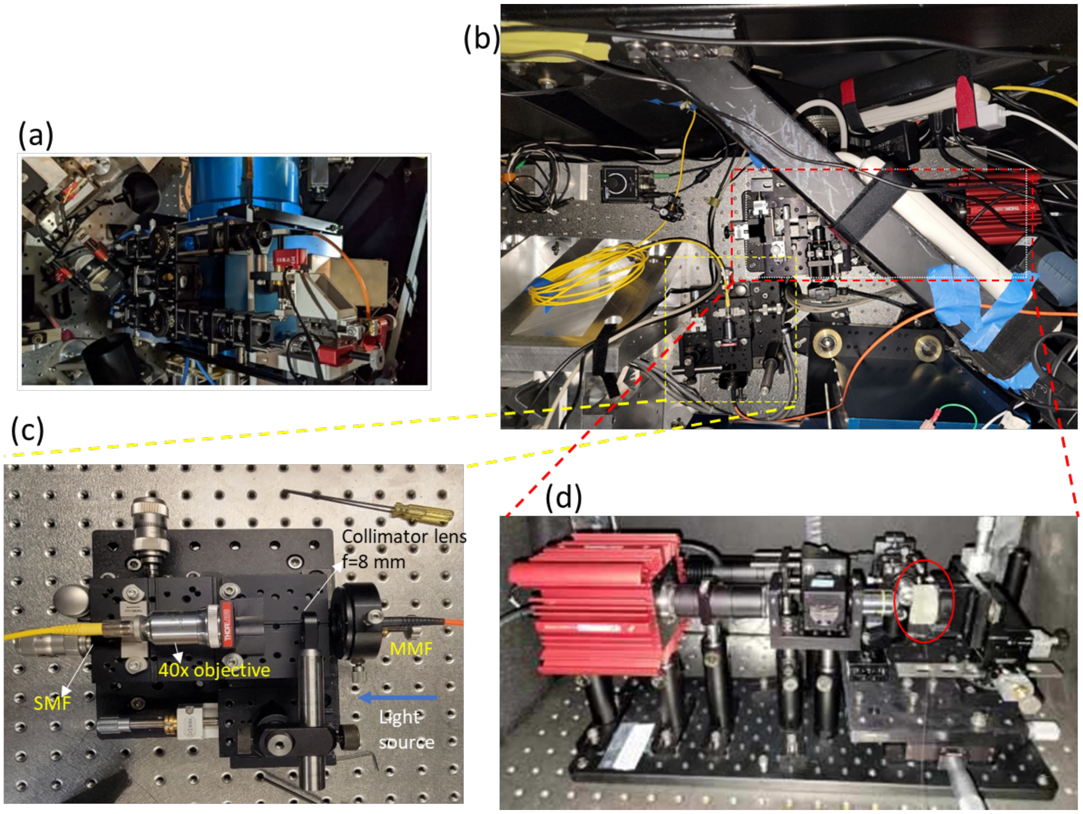

Fig 8.10 (a) The PLIU system to pick off light at the entrance slit of the IR spectrograph (adapted from [217]). (b) MMF to SMF fiber coupling board, and the MMI chip+ microscope board positioned within the AO system. (c) Close-up view of the MMF- to SMF coupling using focusing lenses. (d) The portable microscope and chip mount stage. The red circle shows the custom, 3D printed chip stage for permanent coupling with a fiber.

Astronomical observation is fundamentally a low-light application, while most traditional applications of integrated photonics involve laser sources with measureable power. In order to successfully couple light into the single mode fiber, we also tried to estimate the amount of power available at a telescope from a distant star. The photodetector sensor at our disposal (Thorlabs S130) can measure up to a finite resolution of 0.1 nW for monochromatic laser power. With this instrument, we measured power at the telescope focal plane from the calibration (broadband) white light source installed in the Shane AO system (a temporally stable artificial source comparable with the brightest stars) on two different occasions at different filter configurations. The measurements assume monochromatic light incident on the photodetector. In December 2022, we measured ~3 nW with a 900 nm long pass filter in the path. In March 2024, Z. Weber *et. al* measured 10.3 nW in the same location from the same source without any filter. Our initial estimate shows that the focal spot size at the Cassegrain focus is approximately ~10 mm. On a different experiment in September 2021, the power from Jupiter at the Coude focus (no filter) was measured to be 80 nW, but the practical problem of Jupiter is tracking such a fast moving object in the sky with this telescope. As discussed in chapter 9, an MMI spectrometer was able to detect monochromatic peaks (although with elevated noise) at a test light power level of -65 dBm (0.3 nW) delivered by a single mode fiber in the visible wavelengths range, with a 30 sec exposure time. This means in theory, approximately 3% of the available power (10.3 nW) from the white light source at the focal plane needs to be coupled into the single mode fiber to see a useful MMI pattern (ignoring the finite bandwidth of single mode operation of the fiber). Since this measured power is coming from an extremely broadband spectrum, the power spectral density (power/wavelength) will be pretty low for the minimum (3%) coupling case in practice, and the adjusted coupling efficiency will need to be higher than this theoretical value.

The microscope setup to image the MMI waveguide in a top-down view (Fig. 8.10(d)) follows similar architecture as the Andor camera acquisition setup described in chapter 6 with a few key differences. First, the CMOS camera here (Kiralux CC895MU, Thorlabs) has different noise properties and exposure limit than the lab camera. It also

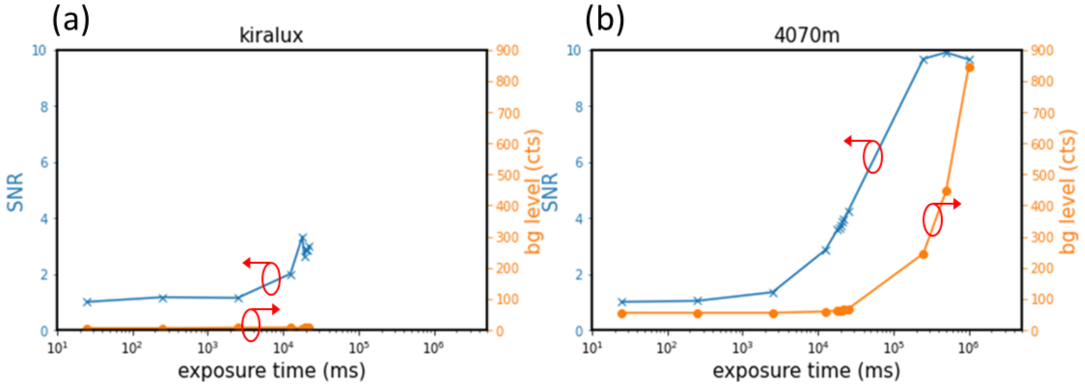

Fig 8.11 (a-b) SNR and background level comparison for 7 nW input power level between an (a) actively cooled camera and (b) camera with no active cooling.

has different bit depth (12 bits), pixel size, and spectral responsivity, which will need to be accounted for in an imaging experiment. Finally, the chip is mounted vertically with respect to the AO bench due to space constraints on the telescope. Also, active cooling of the camera plays an important role in the background noise in the images. For the Lick setup, we have characterized the noise and SNR for two different cameras with (Kiralux) and without (Thorlabs 4070M CCD) cooling for varying exposure times (Figs. 8.11(a-b)) with an input laser power of 7 nW at 690 nm wavelength. As expected, the actively cooled camera has much lower background level compared to the other camera. For this power level, the SNR starts to become greater than 1 at exposure times larger ~10 seconds. Our preliminary estimates show that the power level at the focal plane of the Shane AO is approximately sub-nanowatts level for some of the brightest stars in the sky, which means an improvement in the MMF-SMF coupling, and minimum exposure times > 10 seconds will be ideal for an MMI image acquisition with starlight input. Besides, a few image post-processing improvements can also improve the quality of these images, e.g., binning of multiple images to increase the signal strength [294], and downstream CNN analysis with background subtracted images.

Keeping in mind the relevance of spectrometer operation for low input powers in astronomical observations, in chapter 9, we demonstrate the accuracy of spectral prediction of the MMI spectrometer using CNN framework for sub-nanowatts input power levels tested in the lab. We hope that, in near future, the optimized telescope to chip coupling will enable the successful first acquisition of starlight induced MMI pattern into the spectrometer device.

Chapter 9: Performance optimization of multi-mode interference (MMI) waveguide spectrometer

In chapters 4 and 5, we discussed the basic idea and different implementations of reconstructive, integrated spectrometers that emerged over the past decade, thanks to the advancements in fabrication and optical fiber technologies. On the data processing side, many of these promising implementations involve detecting the wavelength-sensitive light response of a photonic microstructure (e.g. heterojunction current [295], or disordered speckle pattern imaging [15]), developing a calibration matrix, and computationally reconstructing a test spectrum using matrix inversion and advanced optimization [16]. On the computational side, imaging spectrometers like these face challenges in both spectrometer calibration and low light sensitivity. During the calibration process, it is prone to pixel-randomness within the individual images obtained for each input wavelength [296]. The error in the calibration matrix due to such noise can then be exacerbated by subsequent ill-conditioned matrix inversion [171]. Another important aspect to consider for any spectrometer is the device sensitivity, i.e. its performance in a low-light environment, where a detector collecting the image is pushed to its noise limits. Such applications include astronomical observations [297][198], Raman spectroscopy [298], and FRET spectroscopy [299]. Imaging applications such as these face specific challenges in terms of low signal-to-noise ratio in the images [12], stray light [300], and shot noise [296], leading to long integration times for the images. High-quality, expensive camera sensors with active cooling are often required to achieve good signal quality with minimal detector dark noise. Moreover, to minimize the calibration time, it is desirable to calibrate the device response in the presence of sufficient, known input signal power, but still get a robust response at low-light levels.

In chapter 5, we demonstrated the proof-of-concept and established the performance parameters of an MMI waveguide-based integrated spectrometer by combining multi-mode waveguide propagation with top surface scattering. The spectral reconstruction from these images is implemented using convolutional neural network (CNN)-based analysis as discussed in chapter 6. In chapter 7, we also demonstrated its potential for astronomy applications with the analysis of part of the solar spectrum and our astrophotonic instrumentation efforts at Lick observatory. Here, we report a systematic study of the signal enhancement from the MMI spectrometer waveguide by roughening the top surface to enhance scattering from the waveguide. The roughening process increases the inherent signal-to-noise ratio (SNR) of the images captured from the top without increasing the camera exposure time. This effectively increases the detection limit in the low light regime, as discussed in section 9.3. Moreover, the selective etching of a partial length of an MMI waveguide means both the smooth and rough sections can be imaged at different light levels without over-saturating or under-saturating the camera, thus enabling a larger dynamic range of operation than a single type of MMI surface could support. In section 9.4, we study the performance change of our neural network based spectral reconstruction algorithm for gradually diminishing levels of light in the unknown test signal, followed by the investigation of the spectrometer performance dependence on the placement location of the etch start position on the MMI waveguides. The experiments show that low-light sensitivity is maximized by imaging roughened sections with strongly varying spatial MMI patterns. We also measured the change in the brightness of images taken from MMI waveguides with different etch start lengths, enabling us to quantify the scattering loss coefficient of the roughened section.

9.1. Surface etching of the MMI waveguide

The propagation in an MMI spectrometer can be described in terms of the interference effect of the propagating modes inside a wide waveguide, as discussed in chapter 6. Furthermore, the interference pattern interacts with the inherent surface roughness of the planar waveguide to generate out-of-plane scattering, which is imaged at different wavelengths from the top view using an imaging setup. Essentially, top-view light scattering due to waveguide surface irregularity plays a crucial role in the detected signal's strength at the camera for a given input power level. This scattering

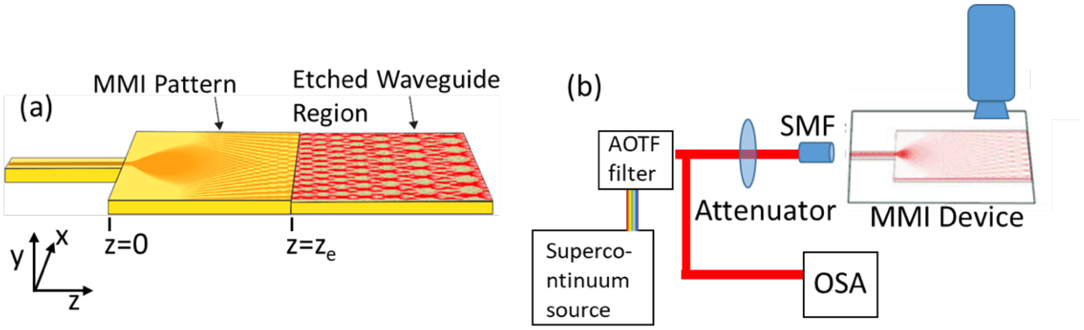

Fig 9.1 (a) Working principle of the etched MMI waveguide spectrometer. Light propagation inside the MMI creates a wavelength-dependent interference pattern, a part of which is scattered from the top surface. This scattering signal can be enhanced by slightly etching part of the MMI waveguide's top surface. (b) Modified data acquisition setup for low light testing.

enhancement is accomplished by roughening of selective areas of the top waveguide surface after the fabrication of the original smooth waveguide. The roughening process uses plasma etching to create a non-uniform (“nano-grass”) layer, which in turn increases the signal-to-noise ratio (SNR) of the images captured by a camera positioned over the waveguide, thus effectively increasing the limit of detection in the low light regime. Fig. 9.1(a) illustrates the concept of enhancing the scattering signal from an MMI waveguide for monochromatic light propagation.

The optical setup used for the detection of the spectrometer’s level sensitivity (lowest input light it can operate at) detection is slightly different from the setups used in the previous chapters and is illustrated in Fig. 9.1(b). A monochromatic, visible-range, tunable light source is created using a combination of a supercontinuum white light source (NKT SuperK Extreme) and an acousto-optic tunable filter (NKT SuperK Select). This light is simultaneously fed into the MMI chip and an OSA using two different single-mode fibers. A variable attenuator is placed in the path of the MMI coupling to control the amount of input light to the device. Using a microscope setup, the MMI pattern is imaged from the top view with the same sCMOS sensor (Andor Zyla). A synchronization script written in Python controlled and communicated among all the instruments in each wavelength step.

9.2. Surface characterization of smooth and rough sections

To enhance the out-of-plane scattering from the MMI waveguide, we induced surface roughness to the top surface of the waveguide starting at a certain MMI waveguide length $z = z_e$, as illustrated in Fig. 9.1(a). The lithography steps for the surface roughening have been already described in chapter 6. Briefly speaking, after the fabrication of the original SU-8 waveguide, a length-varying etch mask for the plasma etching step is created with a combination of an aluminum film layer and an AZ photoresist layer, both of which are removed in the final processing step. Scanning electron microscopy (SEM) images of the smooth and the rough top surfaces on an MMI waveguide are shown in Fig. 9.2(a) and Fig. 9.2(b), respectively. The cross-sectional facet view of an etched MMI waveguide is also shown in Fig. 9.2(c). Because of the distortion induced by the dielectric material charging effect in SEM [301], it is difficult to zoom in and get an accurate estimate of the roughness topology of the top surface in this image.

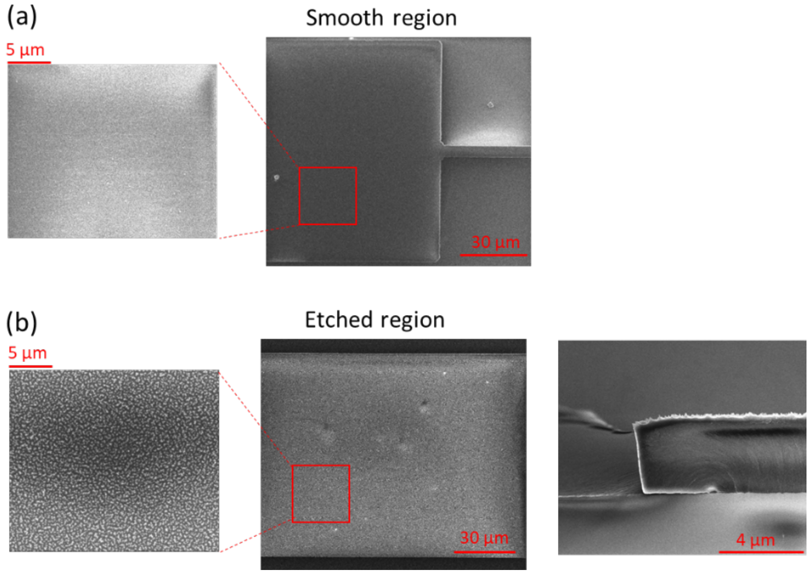

Fig 9.2 Top-down scanning electron microscope images of the unetched (a) and etched (b) regions on the MMI waveguide. (c) Facet view of an etched MMI waveguide, showing the “grass-like” features at the top surface. (SEM courtesy: T. Yuzvinsky.)

For this purpose, i.e., to quantify the surface roughness induced by the plasma etching, high-resolution atomic force microscopy (AFM) scans of the MMI waveguide top surface were performed on both smooth and plasma-etched sections. Fig. 9.3(a) shows the results of scanning over randomly selected 500 nm x 500 nm regions at a scan rate of 1 Hz. The plasma-etched surface clearly contains more uneven features than the smooth counterpart. The root-mean-square (RMS) roughness of the selected regions over the smooth and etched surfaces was calculated to be 0.847 nm and 33.56 nm, respectively, i.e., a ~39x enhancement in the surface roughness. The individual nano-grass features in the region reached a maximum height of 250.3 nm, a number significantly larger than the tallest feature in the smooth region (6.5 nm). The line scan profiles across the center of the scanned regions (y=250 nm) are shown in Fig. 9.3(b). The nano-grass features in the etched region have average lateral FWHM widths in the

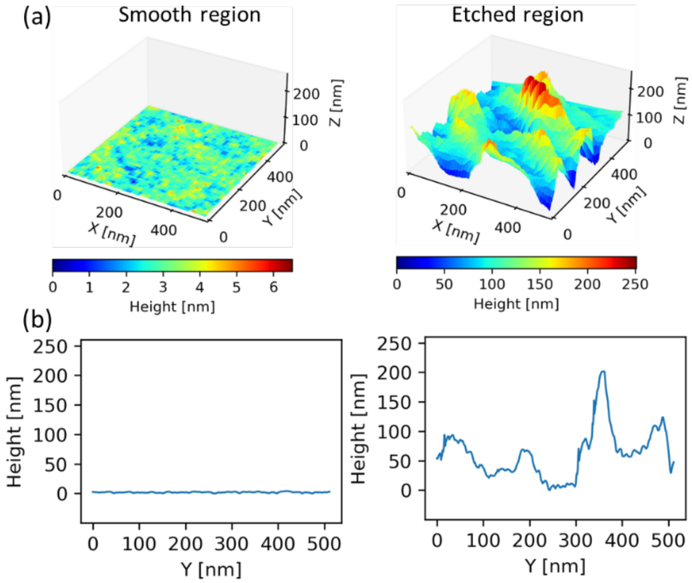

Fig 9.3 (a) Atomic force microscopy (AFM) scans of a 0.25 μm^2 area in the smooth and (left) etched (right) regions on the top surface. (b) Sample line-scan profiles from the AFM characterizations. (AFM courtesy: T. Yuzvinsky.)

order of ~30 nm, in contrast to the almost flat-line-looking profile of the smooth surface. It is important to note that the features observed in this scan depend on the settings of the plasma etching step, such as the power level used, the oxygen flow rate, and the etch time.

9.3. Enhancement of detection limit by plasma etching

To demonstrate the enhancement of out-of-plane scattering of the MMI pattern from the plasma etched region on the spectrometer performance, we coupled -30 dBm (1 µW) of input light at 670 nm wavelength to the MMI spectrometer waveguide and simultaneously imaged the smooth and etched regions with the 16 bits camera at 30

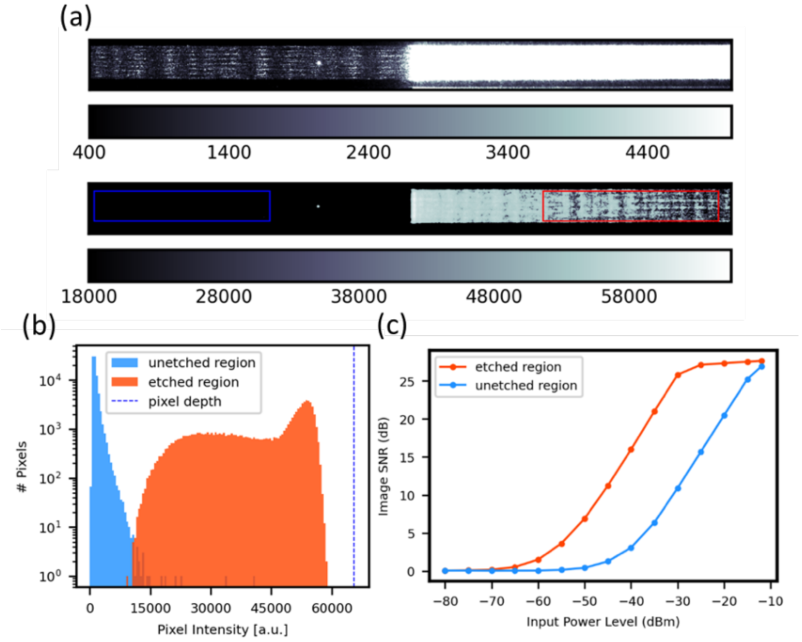

Fig 9.4 (a) MMI patterns imaged from the top at -30dBm input power. Top- weak, but visible signal from the unetched (left-half) region, plotted with a lower colorbar. Bottom- Strong signal pattern from the same image, same input power but from the etched (right-half) region, plotted at a higher colorbar. (b) Intensity distributions of the pixels inside the ROIs in the two regions. The broken line represents the well-depth of the pixels. (c) SNR comparison of the un-etched and etched regions at different power levels of the input light.

seconds exposure time, as shown in Fig. 9.4(a). Here, the same monochrome image is plotted on scales with low and high colorbar limits to display the interference patterns in the smooth and etched regions, respectively. From the images, it is clear that the modal interference pattern transfers into and propagates through the etched waveguide structure with enhanced scattering through the top surface. The enhancement in signal can be quantified by selecting two 555x80 μm in size regions-of-interest (ROI) picked from these images, marked with blue and red boxes in the lower panel of Fig. 9.4(a). The pixel distributions of the ROIs are plotted in Fig. 9.4(b). The pixels from the etched region ROI clearly form a high-contrast, bright image, contrary to the smooth region ROI with many "close-to-background" level pixels. The image signal-to-noise ratio of the smooth and etched regions were also calculated, which can be defined as:

$$\text{SNR (dB)} = 10\ \log \frac{\langle I(x) \rangle}{\sigma_{Noise}} \tag{9.1}$$

Here, $\langle I(x) \rangle$ is the average signal intensity of all pixels in the ROI for a 30 seconds exposure, and σ_{Noise} is the root mean square (RMS) value of the pixel values taken from a dark frame with the same exposure time, representing the noise floor pixel value of the sensor [302][303]. The SNR of the images from both the smooth and etched region at different power levels within the range -12 dBm (63 μW) to -80 dBm (0.01 nW) are plotted in Fig. 9.4(c). It is clear that the etched region consistently gives higher signal compared to the smooth region for the same input light level. In the linear part of the two curves (input levels= -30 to -45 dBm), for the same input light, the etched region generates an average ~13.6 dB higher SNR compared to the smooth region.

Importantly, the etched region reaches a lower limit-of-detection (-65 dBm, P= 310 pW) compared to the smooth region (-50 dBm). This is particularly relevant for the low-light imaging spectroscopy applications discussed earlier. It is important to note that the smooth region images are equally relevant for spectrometer operation for high input power scenarios, where pixels in an etched region image slowly start to approach the pixel capacity (oversaturation). The operable dynamic range of such a hybrid (combination of smooth and etched sections) MMI spectrometer is increased to (-12-(-65)) dBm = 53 dB compared to a single type of MMI. In comparison, the etched region alone operates over a dynamic range of (-20-(-65)) dBm = 45 dB before too many pixels get undersaturated or oversaturated. The performance of this hybrid scheme can be further stretched down to lower input power levels with more sophisticated cameras with a lower noise-floor and longer integration time.

9.4. Effect of etch start position on spectrometer performance

To investigate the effect of the etching location of the MMI top surface on the performance of the MMI spectrometer, our collaborators at BYU fabricated eight kinds of MMI waveguides on the same chip. Here, all spectrometers have an MMI waveguide section with a total length of 20 mm, but the distance of the plasma-etched region start from the beginning of the MMI waveguide (z_e in Fig. 9.1(a)) starts at 2 mm for the first waveguide and 16 mm for the final waveguide, with z_e increasing at 2 mm increments for the six intermediate waveguides. In the following sections, the difference in low light performance in terms of spectrum prediction accuracy and brightness change is investigated between these waveguides.

9.4.1. Etch start position vs low-light spectrometer prediction

As the MMI pattern for a given wavelength propagates along the length of the waveguide, the density of features in the image changes at different lengths of the waveguide. The MMI waveguides of interest here have a total length of 20 mm, but the Andor camera used in these studies has a finite field of view of ~2mm along that dimension, which is common for most high resolution cameras. As a result, the selection of location on the MMI pattern to image will likely have effects on the performance of the MMI spectrometer. To test this, we considered the spectral reconstruction performance of three separate MMI waveguide spectrometers sitting side-by-side on the same device, and the plasma-etched region starts at distances z_e = 2, 10, and 16 mm from the start of the MMI waveguide, respectively. For a particular

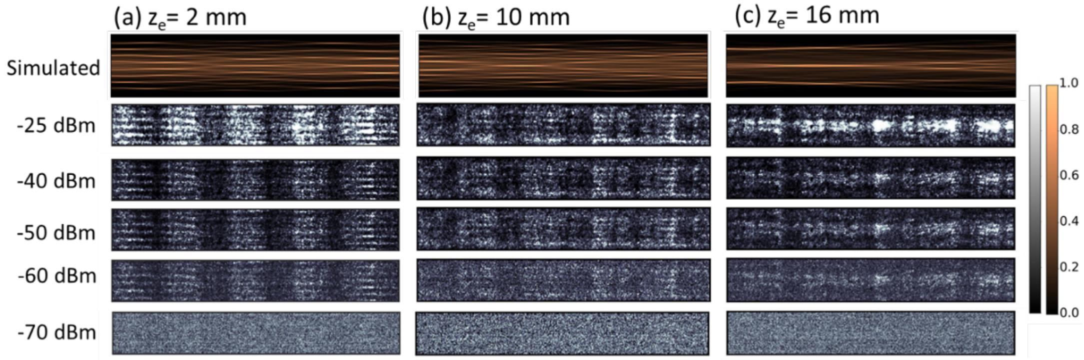

Fig 9.5 Simulated interference patterns vs actual images taken over a 555 µm x 80 µm etched area positioned at MMI lengths (a) z = 3 mm (b) z =11 mm, (c) z = 17 mm. In each case, the image is taken close to the etch start position on each waveguide. In each column, the evolution of each pattern for lower input light levels is also shown.

wavelength, all three waveguides show almost the same overall interference pattern when imaged at the same location. However, to work with differing amounts of interference pattern features in our CNN based spectrometer scheme, we acquired a large image dataset from each waveguide at the start of its etched region with a shorter, 1 second exposure time, and selected a 555 µm x 80 µm ROI located 1mm away from the etch start position for analysis.

The ROIs with distinct patterns for 670 nm input light from the three waveguides are shown in Figs. 9.5(a-c). In each case, the top image shows the simulated MMI interference pattern at the same propagation distance from the beginning of the MMI waveguide. The initial 2D waveguide modes were calculated using finite difference method (FDM) in FIMMWAVE (Photon Design Inc.), followed by their propagation calculation using eigenmode expansion in FIMMPROP (Photon Design Inc.) This is followed by the real interference pattern images for diminishing levels of input power with the same exposure settings. In all cases, we observe good qualitative agreement between the measured and simulated patterns. The initially distinct, high-contrast MMI patterns become increasingly noisier for lower levels of input power. The patterns completely disappear at -70 dBm input power, as also evident from Fig. 9.4(c). The other thing to note is the difference in the amount of structure in the MMI patterns from the three regions due to the length-dependent phase relationship of the propagating modes. The MMI images in Fig. 9.5(a) (captured at a distance z=3 mm from the beginning of the MMI) contain the most amount of high-contrast pattern features, while those in Fig. 9.5(c) captured at length z=17 mm contain the fewest bright features.

For each of the spectrometer waveguides, we acquired multiple training images with 1 second exposure for monochromatic input wavelengths in the wavelength range 620-670 nm at 1 nm steps with -25 dBm input power and simultaneously recorded the corresponding spectra with a 0.2 nm sampling interval. Based on the three independent training datasets acquired from the three spectrometers, we trained three different convolutional neural network (CNN) models with the same architecture. To test the prediction performance of each CNN model on unknown low input light, we also

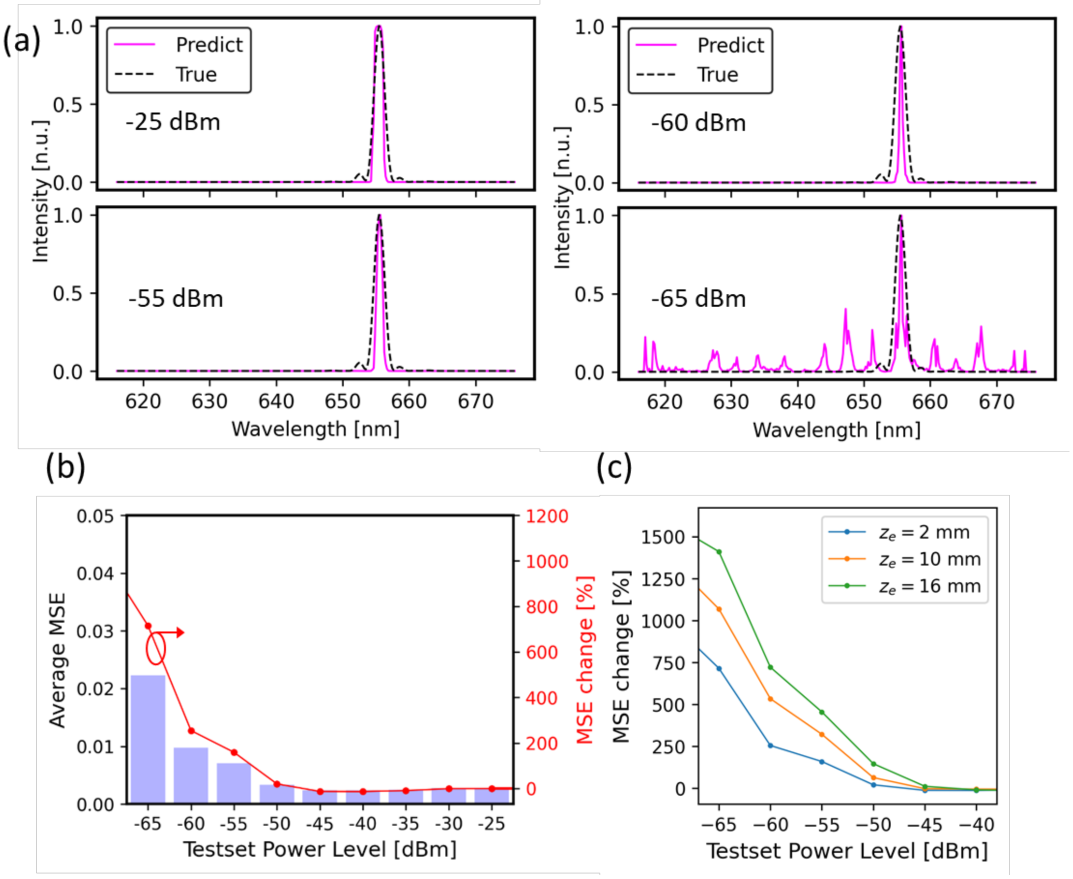

Fig 9.6 (a) Example spectral reconstruction of test signals at different power levels from the MMI waveguide etched at length z_e=2 mm. (b) Reconstruction mean squared error (MSE) vs. input power level (bar plot) for MMI waveguide images at length z_e=2 mm; also shown is the change (%) in the MSE values for these powerlevels (line). (c) change (%) in MSE vs power level for all MMI waveguide images taken at different lengths.

acquired test images at each wavelength for gradually diminishing power levels from -25 dBm to -65 dBm with the same exposure time. Fig. 9.6(a) shows example spectrum predictions of a monochromatic input signal with peak at 655 nm at different power levels by a CNN model trained with the image dataset acquired from MMI waveguide etched at z_e = 2 mm. The CNN predicted spectra closely follow the true spectra of the light for decreasing light levels down to -60 dBm. The noise in the spectral prediction increases due to very low image SNR at -65 dBm, but the CNN model is still able to find the peak of the spectra.

Moreover, the difference between the predicted and the true spectrum among the different MMI spectrometers decreases with the feature density in the MMI patterns in Fig. 9.5. To quantify this difference, we calculated the mean squared error (MSE) between each true and corresponding predicted spectral vector, already introduced in chapter 6 and defined as:

$$\mathrm{MSE} = \frac{1}{N}\sum_{\lambda}\left[I_{true}(\lambda) - I_{predict}(\lambda)\right]^2 \qquad (9.2)$$

Here, $I_{true}(\lambda)$ and $I_{predict}(\lambda)$ are the true and CNN predicted spectral intensity vectors and N is the vector length. We calculated the average MSE across all the monochromatic test images for all wavelengths at a particular power level, and calculated the changes in this average MSE relative to its value obtained from the test images taken at the training power level (-25 dBm). Fig. 9.6(b) shows the gradual increase in average MSE for diminishing power levels for the first MMI spectrometer (etch starts at z_e= 2 mm) with a bar plot. It also shows the percent change in average

MSE value for the same spectrometer (red line), which starts to notably increase at -55 dBm input power. This percent change in the average MSE for diminishing power levels is compared for all the three spectrometers tested, as shown in Fig. 9.6(c). As evident, the performance of the three MMI waveguides start to significantly differ at the low input light levels starting at -55 dBm. The MMI spectrometer trained with the most amount of available feature information (etch starts at z_e= 2 mm) makes the most robust prediction at all light levels, and the opposite is true for the MMI spectrometer with the least amount of information (etch starts at z_e= 16 mm). It is important to note that it is possible to improve the low-light performance of all devices with more extensive data analysis. However, this comes at the price of more computational cost for a larger model and an increasing amount of training data.

9.4.2. Etch start position vs top-scattering quantification

As light travels through the smooth and the subsequent etched section in an MMI waveguide, light scattered from each of these sections results in length-dependent propagation loss, which is collected as signals for the top-imaged MMI spectrometer operation. An important factor to consider is the change in the top-scattered signal brightness. To investigate this, we considered eight MMI spectrometers on the same device with the same total waveguide length as before. Across the spectrometers, the etching on the MMI waveguide started at z_e= 2 mm on the first device and at z_e= 16 mm on the last device, with the etch start position increasing by 2 mm in the intermediate MMIs. This time, all the MMIs were all imaged at the same distance z =

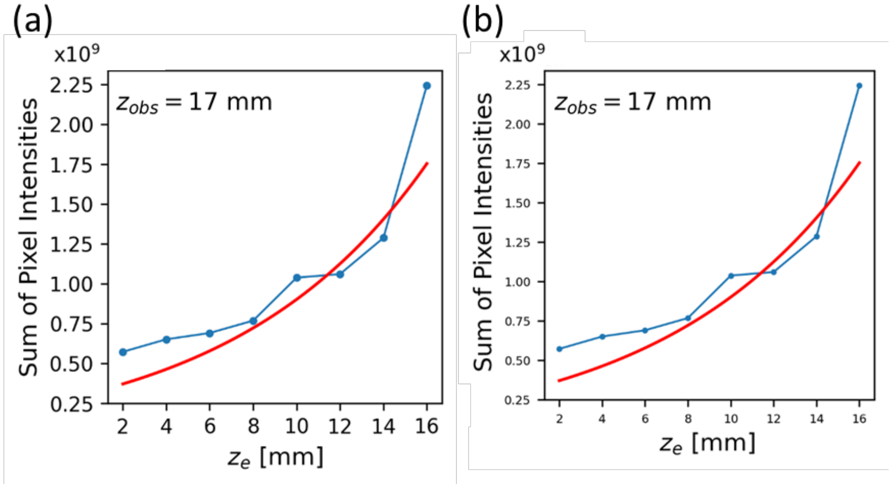

Fig 9.7 (a) Scattered power (sum of image pixels) vs etch start position (blue line with markers) from the MMI sections imaged at the same length and the single exponential model fit described by equation 9.3 (red line). (b) Double exponential fit by taking into account the scatterings from both smooth and etched waveguide sections (red line).

17 mm from the beginning of the MMI waveguide with the same input light level of -25 dBm. We then summed the pixel intensities for each of these images and plotted this value as a function of the etch start position. Fig. 9.7(a) shows that the image brightness at the same MMI location increases exponentially for waveguides with late etch start.

From this data, the scattering coefficient related to the waveguide scattering loss from the etched MMI section can be approximated by treating the image brightness as a representative measure of the top scattered power. First, we assume negligible scattering from the smooth MMI section and calculated the scattering coefficient of the etched section α_{etch} by fitting the sum of image pixel intensities I_{out} with a simple exponential model:

$$I_{out} = I'_{in}. K_1. e^{-\alpha_{etch} \cdot z_{obs}} \tag{9.3}$$

Here, I_{out} is the representative of scattered power at an observation distance z_{obs} from the etch start, I'_{in} is the image intensity (representative of input power) at the beginning of the etched section, and K_1 is the coupling coefficient between the smooth and the etched MMI sections. From this model, α_{etch} is calculated as 1.109 cm^{-1}, and the corresponding fit with equation (9.3) to the data in Fig. 9.7(a) shows good agreement. We then used this value of α_{etch} to calculate the value of α_{smooth}, the scattering coefficient of the smooth MMI waveguide section. This is done by performing a double-exponential curve fit for the pixel sums as:

$$I_{out} = I_{in}.K_2.e^{-\alpha_{smooth} \cdot z_e}.e^{-\alpha_{etch} \cdot z_{etch}} \tag{9.4}$$

Where I_{in} represents the input power to the smooth section (in image intensity units), K_2 is the coupling coefficient between the single-mode and the MMI waveguide, and z_e represents the length of the smooth MMI sections before the etched section starts on each waveguide. Upon plugging in the previous value of α_{etch}, α_{smooth} is calculated to be 0.272 cm^{-1}. This double-exponential fit is also shown in Fig. 9.7(b). Based on these calculations, α_{etch} is much larger than its counterpart α_{smooth}, and is the dominant loss factor responsible for the intensity change in the images. However, the single-exponential fit (equation 9.3) and the double-exponential fit (equation 9.4) plotted in Figs. 9.7(a) and 9.7(b), respectively looks very similar. As α_{etch} is already very well-approximated with a single exponential model to best fit the data, the subsequent double-exponential model contributes very little to improve the curve fit, and hence, this approach of estimating α_{smooth} is not very reliable.

As demonstrated in this chapter, out-of-plane scattering from an MMI pattern can be maximized by plasma-etching a desired portion of the top waveguide surface. This technique can enhance the signal-to-noise ratio for low input light levels while also improving the low light performance of an MMI spectrometer. The feature density and brightness, and in turn, the choice of distance at which to image the scatter pattern is also important for low input light conditions. These results will be important in various critical low light applications, such as the Lick telescope astrophotonic instrumentation efforts described in chapter 8.

Chapter 10: Summary and future works

In conclusion, both top-down excitation based optofluidic biosensors and the MMI spectrometers show promising prospects for the future. The proof-of concept top-down excitation based biosensors show that it is possible to develop a commercial fiber-free, compactly packaged standalone optofluidic scheme using low-cost laser diodes and optical assemblies. On the other hand, the integration of photonic components and advanced learning models open new application avenues for high-performance spectroscopy on a chip.

The first part of the works described here introduced two innovative free-space, top-down excitation techniques for ARROW optofluidic platforms, addressing the limitations of traditional waveguide-based methods. The first approach used an aluminum film with etched slits to enable multi-spot illumination on a liquid core ARROW (LC-ARROW) waveguide, and the other one utilized a patterned Y-splitter waveguide to create multiple confined excitation spots. Both methods eliminate the need for precise alignment associated with single-mode fibers, offering greater flexibility and simplified fabrication requirements. Both the top-down techniques perform comparably to the conventional MMI waveguide-based multisport excitation methods. In particular, the slit-based excitation demonstrates multiplexing capabilities combined with spatially encoding ability. This feature holds significant promise for applications in diagnostics, such as pathogen screening from mixed samples.

One obvious direction for future improvement is the further optimization of the free-space excitation optical assembly for a wider range of biomolecule sensing and more complex bioassays. The chip architecture for these schemes can also be further optimized, since unlike MMI waveguides none of the waveguide dimensions depends on the excitation wavelength. Future work could focus on integrating these methods into fully autonomous lab-on-chip devices for real-time pathogen detection and diagnostics in remote or resource-limited environments. Another exciting possibility lies in enhancing the multiplexing capability of ARROW platforms. By refining the spatial encoding of excitation patterns, it may be possible to achieve higher than 2x multiplexing, allowing for the simultaneous detection of multiple targets in more complex biological samples.

The second part introduced an integrated spectrometer scheme based on multi-mode interference (MMI) waveguides and convolutional neural network (CNN) based analysis for spectral reconstruction. The spectrometer achieved high resolution (0.05 nm) and resolving power (16,000), as observed by testing its capability in both the near-IR and visible wavelength ranges. Accurate spectral reconstructions for narrowband and broadband signals were also accomplished. The relaxed fabrication tolerance and versatile design options of the MMI spectrometer allow integration into various application schemes, as demonstrated by a 4x4 arrayed spectrometer implementation, analysis of the solar spectrum and planned integration into a large 3-meter telescope. Further performance enhancement of the MMI spectrometer in the low light regime was achieved through surface roughening via plasma etching. The etching increased the out-of-plane scattering, thereby increasing the limit of low light level detection. The study also explored optimizing etch start length over the MMI waveguide for more accurate low-light predictions.

Looking ahead, the findings of the works involving the MMI spectrometer pave the way for numerous research and development opportunities. From a high-level perspective, the possible future research directions could be categorized into three groups: improvement on the device's performance, involvement of more advanced machine learning algorithms and image processing techniques, and integration into novel applications. Further refining the surface roughening techniques can achieve higher levels of top scattering, enhancing the signal-to-noise ratios in low-light conditions, which is critical for many sensitive applications. The choice of photoresist as a waveguide material in these works established the framework and core performances of the MMI spectrometer; several other common waveguide materials such as SiO_2, TiO_2 can perform promisingly well while offering more environmental and thermal stability.

Future research in image processing and data analysis for MMI spectrometers could focus on optimizing the current neural network model to improve spectral reconstruction accuracy, particularly in low-light or noisy environments. Application of more advanced, application-specific deep learning models with advanced techniques, such as Generative Adversarial Networks, Vision Transformers etc. can lead to other spectrometer frameworks with more generalized, robust performance. The future application prospects of the chip-scale spectrometer are very exciting. A telescope-integrated, low-light enhanced MMI spectrometer be a used for high-resolution spectral analysis of distant stars, exoplanets, and galaxies with minimal on-site resource requirements. The compact design make them ideal for integration into a large ground telescope but also different space missions like the James Webb space telescope, or the International Space Station where space is an even more expensive resource. Another application opportunity can be integration into lab-on-chip systems for on-chip fluorescence or Raman spectroscopy, thus circumventing the need for external, expensive spectroscopy analysis tools. All in all, the ideas discussed in this work will hopefully lead the way to transformative applications across various disciplines.

Bibliography

[1] K. Tao *et al.*, “The biological and clinical significance of emerging SARS-CoV-2 variants,” *Nat. Rev. Genet.*, vol. 22, no. 12, pp. 757–773, Dec. 2021.

[2] S. Yang and R. E. Rothman, “PCR-based diagnostics for infectious diseases: uses, limitations, and future applications in acute-care settings,” *Lancet Infect. Dis.*, vol. 4, no. 6, pp. 337–348, Jun. 2004.

[3] M. F. Clark, R. M. Lister, and M. Bar-Joseph, “ELISA techniques,” in *Methods in Enzymology*, Academic Press, 1986, pp. 742–766.

[4] L. Kricka, “Clinical applications of chemiluminescence,” *Anal. Chim. Acta*, vol. 500, no. 1–2, pp. 279–286, Dec. 2003.

[5] X. Fan and I. M. White, “Optofluidic microsystems for chemical and biological analysis,” *Nat. Photonics*, vol. 5, no. 10, pp. 591–597, 2011.

[6] P. Minzioni *et al.*, “Roadmap for optofluidics,” *J. Opt.*, vol. 19, no. 9, p. 093003, Sep. 2017.

[7] H. Schmidt and A. R. Hawkins, “The photonic integration of non-solid media using optofluidics,” *Nat. Photonics*, vol. 5, no. 10, pp. 598–604, Oct. 2011.

[8] D. Ozcelik *et al.*, “Optofluidic wavelength division multiplexing for single-virus detection,” *Proc. Natl. Acad. Sci.*, vol. 112, no. 42, pp. 12933–12937, 2015.

[9] A. Stambaugh, J. W. Parks, M. A. Stott, G. G. Meena, A. R. Hawkins, and H. Schmidt, “Optofluidic multiplex detection of single SARS-CoV-2 and influenza A antigens using a novel bright fluorescent probe assay,” *Proc. Natl. Acad. Sci.*, vol. 118, no. 20, p. e2103480118, May 2021.

[10] Z. Yang, T. Albrow-Owen, W. Cai, and T. Hasan, “Miniaturization of optical spectrometers,” *Science*, vol. 371, no. 6528, p. eabe0722, 2021.

[11] J. Bland-Hawthorn, “Astrophotonics: the future of astronomical instrumentation,” in *CLEO*, 2015.

[12] A. Li *et al.*, “Advances in cost-effective integrated spectrometers,” *Light Sci. Appl.*, vol. 11, no. 1, p. 174, Jun. 2022.

[13] L. Zhang, J. Chen, C. Ma, W. Li, Z. Qi, and N. Xue, “Research Progress on On-Chip Fourier Transform Spectrometer,” *Laser Photon. Rev.*, vol. 15, no. 9, p. 2100016, Sep. 2021.

[14] X. Gan, N. Pervez, I. Kymissis, F. Hatami, and D. Englund, “A high-resolution spectrometer based on a compact planar two dimensional photonic crystal cavity array,” *Appl. Phys. Lett.*, vol. 100, no. 23, p. 231104, Jun. 2012.

[15] B. Redding, S. F. Liew, R. Sarma, and H. Cao, “Compact spectrometer based on a disordered photonic chip,” *Nat. Photonics*, vol. 7, no. 9, pp. 746–751, 2013.

[16] B. Redding, M. ALam, M. Seifert, and H. Cao, “High-resolution and broadband all-fiber spectrometers,” *Optica*, vol. 1, no. 3, pp. 175–180, 2014.

[17] L. Chrostowski and M. Hochberg, *Silicon Photonics Design*. Cambridge University Press, 2015.

[18] A. R. Hawkins and H. Schmidt, Eds., *Handbook of Optofluidics*, 1st ed. CRC Press, 2010.

[19] T. Kitoh and K. Kawano, *Introduction to Optical Waveguide Analysis: Solving Maxwell’s Equation and the Schrodinger Equation*, 1st ed. New York: Wiley,

2001.

[20] P. Yeh, *Optical Waves in Layered Media*, 2nd ed. New York: Wiley, 2005.

[21] S. O. Kasap, *Optoelectronics and Photonics: principles and practices*, 2nd ed. Prentice Hall, 2001.

[22] A. Yariv and P. Yeh, *Optical Waves in Crystals: Propagation and Control of Laser Radiation*, 1st ed. New York: Wiley, 1984.

[23] O. Lazcka, F. J. Del Campo, and F. X. Muñoz, "Pathogen detection: A perspective of traditional methods and biosensors," *Biosens. Bioelectron.*, vol. 22, no. 7, pp. 1205–1217, Feb. 2007.

[24] A. Jagannath, H. Cong, J. Hassan, G. Gonzalez, M. D. Gilchrist, and N. Zhang, "Pathogen detection on microfluidic platforms: Recent advances, challenges, and prospects," *Biosens. Bioelectron. X*, vol. 10, p. 100134, May 2022.

[25] P. Rajapaksha, A. Elbourne, S. Gangadoo, R. Brown, D. Cozzolino, and J. Chapman, "A review of methods for the detection of pathogenic microorganisms," *Analyst*, vol. 144, no. 2, pp. 396–411, 2019.

[26] Buddhisha Udugama *et al.*, "Diagnosing COVID-19: The Disease and Tools for Detection," *ACS Nano*, vol. 14, no. 4, pp. 3822–3835, 2020.

[27] Y. C. Lim, A. Z. Kouzani, and W. Duan, "Lab-on-a-chip: a component view," *Microsyst. Technol.*, vol. 16, no. 12, pp. 1995–2015, Dec. 2010.

[28] H. Zhu, Z. Fohlerová, J. Pekárek, E. Basova, and P. Neužil, "Recent advances in lab-on-a-chip technologies for viral diagnosis," *Biosens. Bioelectron.*, vol. 153, p. 112041, Apr. 2020.

[29] P. S. Dittrich and A. Manz, “Lab-on-a-chip: microfluidics in drug discovery,” *Nat. Rev. Drug Discov.*, vol. 5, no. 3, pp. 210–218, Mar. 2006.

[30] C. D. Chin *et al.*, “Microfluidics-based diagnostics of infectious diseases in the developing world,” *Nat. Med.*, vol. 17, no. 8, pp. 1015–1019, Aug. 2011.

[31] N. Cohen *et al.*, “Microsphere based continuous-flow immunoassay in a microfluidic device for determination of clinically relevant insulin levels,” *Microchim. Acta*, vol. 184, no. 3, pp. 835–841, Mar. 2017.

[32] M. T. Guo, A. Rotem, J. A. Heyman, and D. A. Weitz, “Droplet microfluidics for high-throughput biological assays,” *Lab Chip*, vol. 12, no. 12, p. 2146, 2012.

[33] V. Chokkalingam, B. Weidenhof, M. Krämer, W. F. Maier, S. Herminghaus, and R. Seemann, “Optimized droplet-based microfluidics scheme for sol–gel reactions,” *Lab Chip*, vol. 10, no. 13, p. 1700, 2010.

[34] K. J. Land, Ed., *Paper-based Diagnostics: Current status and future applications*. Springer, 2018.

[35] R. Burger, L. Amato, and A. Boisen, “Detection methods for centrifugal microfluidic platforms,” *Biosens. Bioelectron.*, vol. 76, pp. 54–67, Feb. 2016.

[36] A. F. Gavela, D. G. García, J. C. Ramirez, and L. M. Lechuga, “Last advances in silicon-based optical biosensors,” *Sensors (Basel)*, vol. 16, no. 3, pp. 1–15, 2016.

[37] J. Flueckiger *et al.*, “Sub-wavelength grating for enhanced ring resonator biosensor,” *Opt. Express*, vol. 24, no. 14, p. 15672, Jul. 2016.

[38] D. Yan, L. Qiu, M. Xue, Z. Meng, and Y. Wang, “A flexible surface-enhanced

Raman substrates based on cellulose photonic crystal/Ag-nanoparticles composite," *Mater. Des.*, vol. 165, p. 107601, 2019.

[39] J. R. Anderson *et al.*, "Fabrication of Topologically Complex Three-Dimensional Microfluidic Systems in PDMS by Rapid Prototyping," *Anal. Chem.*, vol. 72, no. 14, pp. 3158–3164, Jul. 2000.

[40] J. W. Parks and H. Schmidt, "Flexible optofluidic waveguide platform with multi-dimensional reconfigurability," *Sci. Rep.*, vol. 6, no. 1, p. 33008, Sep. 2016.

[41] T. Sano, H. Zhang, R. Losakul, and H. Schmidt, "All-in-One Optofluidic Chip for Molecular Biosensing Assays," *Biosensors*, vol. 12, no. 7, p. 501, Jul. 2022.

[42] D. Psaltis, S. R. Quake, and C. Yang, "Developing optofluidic technology through the fusion of microfluidics and optics," *Nature*, vol. 442, no. 7101, pp. 381–386, Jul. 2006.

[43] H. Schmidt and A. R. Hawkins, "Single molecule analysis with planar optofluidics," in *Advanced Photonics Structures for Biological and Chemical Detection*, Springer, 2009, pp. 487–512.

[44] A. Stambaugh, J. W. Parks, M. A. Stott, G. G. Meena, A. R. Hawkins, and H. Schmidt, "Optofluidic multiplex detection of single SARS-CoV-2 and influenza A antigens using a novel bright fluorescent probe assay," *Proc. Natl. Acad. Sci.*, vol. 118, no. 20, May 2021.

[45] G. G. Meena, A. M. Stambaugh, V. Ganjalizadeh, M. A. Stott, A. R. Hawkins, and H. Schmidt, "Ultrasensitive detection of SARS-CoV-2 RNA and antigen

using single-molecule optofluidic chip," *APL Photonics*, vol. 6, no. 6, Jun. 2021.

[46] T. Sano, J. Black, S. Mitchell, H. Zhang, and H. Schmidt, "Pneumatically tunable optofluidic DFB dye laser using corrugated sidewalls," *Opt. Lett.*, vol. 45, no. 21, p. 5978, Nov. 2020.

[47] H. Schmidt and A. R. Hawkins, "Optofluidic waveguides: I. Concepts and implementations," *Microfluid. Nanofluidics*, vol. 4, no. 1–2, pp. 3–16, Jan. 2008.

[48] K. J. Rowland, S. Afshar, A. Stolyarov, Y. Fink, and T. M. Monro, "Bragg waveguides with low-index liquid cores," *Opt. Express*, vol. 20, no. 1, p. 48, Jan. 2012.

[49] J. Park, D.-E. Kang, B. Paulson, T. Nazari, and K. Oh, "Liquid core photonic crystal fiber with low-refractive-index liquids for optofluidic applications," *Opt. Express*, vol. 22, no. 14, p. 17320, Jul. 2014.

[50] D. Yin, H. Schmidt, J. P. Barber, and A. R. Hawkins, "Integrated ARROW waveguides with hollow cores," *Opt. Express*, vol. 12, no. 12, p. 2710, 2004.

[51] M. A. Duguay, Y. Kokubun, T. L. Koch, and L. Pfeiffer, "Antiresonant reflecting optical waveguides in SiO2-Si multilayer structures," *Appl. Phys. Lett.*, vol. 49, no. 1, pp. 13–15, 1986.

[52] D. Yin, E. J. Lunt, M. I. Rudenko, D. W. Deamer, A. R. Hawkins, and H. Schmidt, "Planar optofluidic chip for single particle detection, manipulation, and analysis," *Lab Chip*, vol. 7, no. 9, p. 1171, 2007.

[53] D. Ozcelik *et al.*, "Dual-core optofluidic chip for independent particle detection and tunable spectral filtering," *Lab Chip*, vol. 12, no. 19, p. 3728, 2012.

[54] G. G. Meena *et al.*, "3× multiplexed detection of antibiotic resistant plasmids with single molecule sensitivity," *Lab Chip*, vol. 20, no. 20, pp. 3763–3771, 2020.

[55] J. L. Archambault, R. J. Black, S. Lacroix, and J. Bures, "Loss Calculations for Antiresonant Waveguides," *J. Light. Technol.*, vol. 11, no. 3, pp. 416–423, 1993.

[56] D. Ozcelik, "OPTOFLUIDIC DEVICES FOR BIOMOLECULE SENSING AND MULTIPLEXING," 2016.

[57] D. Yin, J. P. Barber, A. R. Hawkins, and H. Schmidt, "Highly efficient fluorescence detection in picoliter volume liquid-core waveguides," *Appl. Phys. Lett.*, vol. 87, no. 21, Nov. 2005.

[58] J. R. Lakowicz, "Principles of Fluorescence Correlation Spectroscopy," in *Principles of fluorescence spectroscopy*, 3rd ed., Springer, pp. 798–799.

[59] P. Van Zant, *Microchip Fabrication: A Practical Guide to Semiconductor Processing*, 6th ed. New York: McGraw-Hill, 2000.

[60] E. J. Lunt, B. Wu, J. M. Keeley, P. Measor, H. Schmidt, and A. R. Hawkins, "Hollow ARROW Waveguides on Self-Aligned Pedestals for Improved Geometry and Transmission," *IEEE Photonics Technol. Lett.*, vol. 22, no. 15, pp. 1147–1149, Aug. 2010.

[61] T. Wall, J. Mcmurray, G. Meena, V. Ganjalizadeh, H. Schmidt, and A. R. Hawkins, "Optofluidic Lab-on-a-Chip Fluorescence Sensor Using Integrated Buried ARROW (bARROW) Waveguides," *Micromachines*, vol. 8, pp. 252–260, 2017.

[62] T. Wall *et al.*, “Mitigating Water Absorption in Waveguides Made from Unannealed PECVD SiO2,” *IEEE Photonics Technol. Lett.*, vol. 29, no. 10, pp. 806–809, 2017.

[63] D. Ozcelik *et al.*, “Signal-to-noise enhancement in optical detection of single viruses with multispot excitation,” *IEEE J. Sel. Top. Quantum Electron.*, vol. 22, no. 4, pp. 6–11, 2016.

[64] T. Uematsu, Y. Ishizaka, Y. Kawaguchi, K. Saitoh, and M. Koshiba, “Design of a Compact Two-Mode Multi/Demultiplexer Consisting of Multimode Interference Waveguides and a Wavelength-Insensitive Phase Shifter for Mode-Division Multiplexing Transmission,” *J. Light. Technol.*, vol. 30, no. 15, pp. 2421–2426, Aug. 2012.

[65] Y. Li, C. Li, C. Li, B. Cheng, and C. Xue, “Compact two-mode (de)multiplexer based on symmetric Y-junction and Multimode interference waveguides,” *Opt. Express*, vol. 22, no. 5, p. 5781, Mar. 2014.

[66] L. B. Soldano and E. C. M. Pennings, “Optical multi-mode interference devices based on self-imaging: principles and applications,” *J. Light. Technol.*, vol. 13, no. 4, pp. 615–627, Apr. 1995.

[67] V. Ganjalizadeh, G. G. Meena, T. A. Wall, M. A. Stott, A. R. Hawkins, and H. Schmidt, “Fast custom wavelet analysis technique for single molecule detection and identification,” *Nat. Commun.*, vol. 13, no. 1, p. 1035, Feb. 2022.

[68] G. G. Meena, “Multiplexed Biosensors for Pathogen Detection,” 2021.

[69] G. G. Meena *et al.*, “7X multiplexed, optofluidic detection of nucleic acids for

antibiotic-resistance bacterial screening," *Opt. Express*, vol. 28, no. 22, p. 33019, Oct. 2020.

[70] D. Ozcelik *et al.*, "Scalable Spatial-Spectral Multiplexing of Single-Virus Detection Using Multimode Interference Waveguides," *Sci. Rep.*, vol. 7, no. 1, pp. 1–8, 2017.

[71] H. Cai, M. A. Stott, D. Ozcelik, J. W. Parks, A. R. Hawkins, and H. Schmidt, "On-chip wavelength multiplexed detection of cancer DNA biomarkers in blood," *Biomicrofluidics*, vol. 10, no. 6, 2016.

[72] A. Stambaugh, J. W. Parks, M. A. Stott, G. G. Meena, A. R. Hawkins, and H. Schmidt, "Optofluidic detection of Zika nucleic acid and protein biomarkers using multimode interference multiplexing," *Biomed. Opt. Express*, vol. 9, no. 8, p. 3725, Aug. 2018.

[73] M. J. N. Sampad, M. N. Amin, A. R. Hawkins, and H. Schmidt, "FPGA Integrated Optofluidic Biosensor for Real-Time Single Biomarker Analysis," *IEEE Photonics J.*, vol. 14, no. 1, pp. 1–6, Feb. 2022.

[74] V. Ganjalizadeh, G. G. Meena, M. A. Stott, A. R. Hawkins, and H. Schmidt, "Machine learning at the edge for AI-enabled multiplexed pathogen detection," *Sci. Rep.*, vol. 13, no. 1, p. 4744, Mar. 2023.

[75] Y. S. Huh, A. J. Chung, and D. Erickson, "Surface enhanced Raman spectroscopy and its application to molecular and cellular analysis," *Microfluid. Nanofluidics*, vol. 6, no. 3, pp. 285–297, Mar. 2009.

[76] X. X. Han, R. S. Rodriguez, C. L. Haynes, Y. Ozaki, and B. Zhao, "Surface-

enhanced Raman spectroscopy," *Nat. Rev. Methods Prim.*, vol. 1, no. 1, p. 87, Jan. 2022.

[77] H. Wang, Z. Xue, Y. Wu, J. Gilmore, L. Wang, and L. Fabris, "Rapid SERS Quantification of Trace Fentanyl Laced in Recreational Drugs with a Portable Raman Module," *Anal. Chem.*, vol. 93, no. 27, pp. 9373–9382, Jul. 2021.

[78] K. Kneipp, H. Kneipp, I. Itzkan, R. R. Dasari, and M. S. Feld, "Surface-enhanced Raman scattering and biophysics," *J. Phys. Condens. Matter*, vol. 14, no. 18, p. 202, May 2002.

[79] S. Nie and S. R. Emory, "Probing Single Molecules and Single Nanoparticles by Surface-Enhanced Raman Scattering," *Science (80-.).*, vol. 275, no. 5303, pp. 1102–1106, Feb. 1997.

[80] P. Measor *et al.*, "On-chip surface-enhanced Raman scattering detection using integrated liquid-core waveguides," *Appl. Phys. Lett.*, vol. 90, no. 21, May 2007.

[81] H. Schmidt, Dongliang Yin, J. P. Barber, and A. R. Hawkins, "Hollow-core waveguides and 2-D waveguide arrays for integrated optics of gases and liquids," *IEEE J. Sel. Top. Quantum Electron.*, vol. 11, no. 2, pp. 519–527, Mar. 2005.

[82] R. Marchetti *et al.*, "High-efficiency grating-couplers: Demonstration of a new design strategy," *Sci. Rep.*, vol. 7, no. 1, pp. 1–8, 2017.

[83] M. A. Stott *et al.*, "Optimized ARROW-Based MMI Waveguides for High Fidelity Excitation Patterns for Optofluidic Multiplexing," *IEEE J. Quantum Electron.*, vol. 54, no. 3, pp. 1–7, 2018.

[84] A. Sánchez-Postigo *et al.*, "Breaking the Coupling Efficiency–Bandwidth Trade-Off in Surface Grating Couplers Using Zero-Order Radiation," *Laser Photon. Rev.*, vol. 15, no. 6, Jun. 2021.

[85] N. Fabri-Faja *et al.*, "Early sepsis diagnosis via protein and miRNA biomarkers using a novel point-of-care photonic biosensor," *Anal. Chim. Acta*, vol. 1077, pp. 232–242, 2019.

[86] P. Kiesel, M. Bassler, M. Beck, and N. Johnson, "Spatially modulated fluorescence emission from moving particles," *Appl. Phys. Lett.*, vol. 94, no. 4, 2009.

[87] J. Martini, M. I. Recht, M. Huck, M. W. Bern, N. M. Johnson, and P. Kiesel, "Time encoded multicolor fluorescence detection in a microfluidic flow cytometer," *Lab Chip*, vol. 12, no. 23, pp. 5057–5062, 2012.

[88] N. Meidinger *et al.*, "Frame store PN-CCD detector for the ROSITA mission," in *Proc. SPIE 4851, X-Ray and Gamma-Ray Telescopes and Instruments for Astronomy*, 2003, vol. 4851, p. 1040.

[89] G. G. Meena, J. G. Wright, A. R. Hawkins, and H. Schmidt, "Greatly Enhanced Single Particle Fluorescence Detection Using High Refractive Index Liquid-Core Waveguides," *IEEE J. Sel. Top. Quantum Electron.*, vol. 27, no. 5, pp. 1–7, Sep. 2021.

[90] I. Newton, *Opticks: or, A Treatise of the Reflexions, Inflexions and Colours of Light*, 4th ed. Dover Publications, 1730.

[91] J. C. D. Brand, *Lines of Light: The Sources of Dispersive Spectroscopy*. Gordon

& Breach Publications, 1995.

[92] D. Kleppner, “The Master of Dispersion,” *Phys. Today*, vol. 58, no. 11, pp. 10–11, Nov. 2005.

[93] M. Mayor and D. Queloz, “A Jupiter-mass companion to a solar-type star,” *Nature*, vol. 378, no. 6555, pp. 355–359, Nov. 1995.

[94] B. Godard, E. Falgarone, M. Gerin, P. Hily-Blant, and M. De Luca, “Molecular absorption lines toward star-forming regions: a comparative study of HCO + , HNC, HCN, and CN,” *Astron. Astrophys.*, vol. 520, p. A20, Sep. 2010.

[95] S. Weiss, “Fluorescence Spectroscopy of Single Biomolecules,” *Science (80-.).*, vol. 283, no. 5408, pp. 1676–1683, Mar. 1999.

[96] A. Downes and A. Elfick, “Raman Spectroscopy and Related Techniques in Biomedicine,” *Sensors*, vol. 10, no. 3, pp. 1871–1889, Mar. 2010.

[97] W. Mäntele and E. Deniz, “UV–VIS absorption spectroscopy: Lambert-Beer reloaded,” *Spectrochim. Acta Part A Mol. Biomol. Spectrosc.*, vol. 173, pp. 965–968, Feb. 2017.

[98] L. Whitmore and B. A. Wallace, “Protein secondary structure analyses from circular dichroism spectroscopy: Methods and reference databases,” *Biopolymers*, vol. 89, no. 5, pp. 392–400, May 2008.

[99] J. Seo *et al.*, “PICASSO allows ultra-multiplexed fluorescence imaging of spatially overlapping proteins without reference spectra measurements,” *Nat. Commun.*, vol. 13, no. 1, p. 2475, May 2022.

[100] G. K. Geiss *et al.*, “Direct multiplexed measurement of gene expression with

color-coded probe pairs," *Nat. Biotechnol.*, vol. 26, no. 3, pp. 317–325, Mar. 2008.

[101] Y. Xiong *et al.*, "Photonic crystal enhanced fluorescence emission and blinking suppression for single quantum dot digital resolution biosensing," *Nat. Commun.*, vol. 13, no. 1, p. 4647, Aug. 2022.

[102] S. A. Khan, S. B. Khan, L. U. Khan, A. Farooq, K. Akhtar, and A. M. Asiri, "Fourier Transform Infrared Spectroscopy: Fundamentals and Application in Functional Groups and Nanomaterials Characterization," in *Handbook of Materials Characterization*, Cham: Springer International Publishing, 2018, pp. 317–344.

[103] L. Rolinger, M. Rüdt, and J. Hubbuch, "A critical review of recent trends, and a future perspective of optical spectroscopy as PAT in biopharmaceutical downstream processing," *Anal. Bioanal. Chem.*, vol. 412, no. 9, pp. 2047–2064, Apr. 2020.

[104] N. Heigl *et al.*, "Near Infrared Spectroscopy for Polymer Research, Quality Control and Reaction Monitoring," *J. Near Infrared Spectrosc.*, vol. 15, no. 5, pp. 269–282, Oct. 2007.

[105] M. A. Butt, G. S. Voronkov, E. P. Grakhova, R. V. Kutluyarov, N. L. Kazanskiy, and S. N. Khonina, "Environmental Monitoring: A Comprehensive Review on Optical Waveguide and Fiber-Based Sensors," *Biosensors*, vol. 12, no. 11, p. 1038, Nov. 2022.

[106] V. Cortés, J. Blasco, N. Aleixos, S. Cubero, and P. Talens, "Monitoring

strategies for quality control of agricultural products using visible and near-infrared spectroscopy: A review," *Trends Food Sci. Technol.*, vol. 85, pp. 138–148, Mar. 2019.

[107] K. B. Beć, J. Grabska, and C. W. Huck, "Miniaturized NIR Spectroscopy in Food Analysis and Quality Control: Promises, Challenges, and Perspectives," *Foods*, vol. 11, no. 10, p. 1465, May 2022.

[108] C. A. F. de Oliveira Penido, M. T. T. Pacheco, I. K. Lednev, and L. Silveira, "Raman spectroscopy in forensic analysis: identification of cocaine and other illegal drugs of abuse," *J. Raman Spectrosc.*, vol. 47, no. 1, pp. 28–38, Jan. 2016.

[109] B. Huang *et al.*, "Non-covalent interactions in electrochemical reactions and implications in clean energy applications," *Phys. Chem. Chem. Phys.*, vol. 20, no. 23, pp. 15680–15686, 2018.

[110] J. T. McWhirter and A. J. Sievers, "Time-Resolved Spectroscopy with Fourier Transform Spectrometers: Maintaining the Fellgett Advantage," *Appl. Spectrosc.*, vol. 45, no. 9, pp. 1391–1394, 1991.

[111] A. B. Shafer, L. R. Megill, and L. Droppleman, "Optimization of the Czerny–Turner Spectrometer," *J. Opt. Soc. Am.*, vol. 54, no. 7, p. 879, Jul. 1964.

[112] E. G. Loewen, "Differences Gratings Ruled and Holographic," in *Applied Optics and Optical Engineering, Volume 9*, R. R. Shannon and J. C. Wyant, Eds. New York: Academic Press, 1983.

[113] J. Gao, P. Chen, L. Wu, B. Yu, and L. Qian, "A review on fabrication of blazed gratings," *J. Phys. D. Appl. Phys.*, vol. 54, no. 31, p. 313001, Aug. 2021.

[114] L. D. Keller, D. T. Jaffe, O. A. Ershov, T. Benedict, and U. U. Graf, "Fabrication and testing of chemically micromachined silicon echelle gratings," *Appl. Opt.*, vol. 39, no. 7, p. 1094, Mar. 2000.

[115] J. M. Tsui, C. Thompson, V. Mehta, J. M. Roth, V. I. Smirnov, and L. B. Glebov, "Coupled-wave analysis of apodized volume gratings," *Opt. Express*, vol. 12, no. 26, p. 6642, 2004.

[116] M. Totzeck, "Interferometry," in *Springer Handbook of Lasers and Optics*, Berlin, Heidelberg: Springer Berlin Heidelberg, 2012, pp. 1255–1283.

[117] B. C. Smith, *Fundamentals of Fourier Transform Infrared Spectroscopy*, 2nd ed. Boca Raton: CRC Press, 2011.

[118] J. W. Cooley and J. W. Tukey, "An Algorithm for the Machine Calculation of Complex Fourier Series," *Math. Comput.*, vol. 19, no. 90, p. 297, Apr. 1965.

[119] N. Corporation, "Technical Note: Introduction to FTIR Spectroscopy." [Online]. Available: https://www.newport.com/n/introduction-to-ftir-spectroscopy.

[120] E. Lai, "Converting analog to digital signals and vice versa," in *Practical Digital Signal Processing*, Elsevier, 2003, pp. 14–49.

[121] J. T. Daly, E. A. Johnson, W. A. Bodkin, W. A. Stevenson, and D. A. White, "Recent advances in miniaturization of infrared spectrometers," in *SPIE Symposium on integrated optoelectronics*, 2000, pp. 70–87.

[122] S. Traut and H. P. Herzig, "Holographically recorded gratings on microlenses for a miniaturized spectrometer array," *Opt. Eng.*, vol. 39, no. 1, p. 290, Jan. 2000.

[123] Z. Yang *et al.*, “Single-nanowire spectrometers,” *Science (80-.).*, vol. 365, no. 6457, pp. 1017–1020, Sep. 2019.

[124] M. C. M. M. Souza, A. Grieco, N. C. Frateschi, and Y. Fainman, “Fourier transform spectrometer on silicon with thermo-optic non-linearity and dispersion correction,” *Nat. Commun.*, vol. 9, no. 1, p. 665, Feb. 2018.

[125] J. Bao and M. G. Bawendi, “A colloidal quantum dot spectrometer,” *Nature*, vol. 523, no. 7558, pp. 67–70, Jul. 2015.

[126] R. F. Wolffenbuttel, “State-of-the-Art in Integrated Optical Microspectrometers,” *IEEE Trans. Instrum. Meas.*, vol. 53, no. 1, pp. 197–202, Feb. 2004.

[127] T. A. Kwa and R. F. Wolffenbuttel, “Integrated grating/detector array fabricated in silicon using micromachining techniques,” *Sensors Actuators A Phys.*, vol. 31, no. 1–3, pp. 259–266, Mar. 1992.

[128] P. Gatkine, S. Veilleux, Y. Hu, J. Bland-Hawthorn, and M. Dagenais, “Arrayed waveguide grating spectrometers for astronomical applications: new results,” *Opt. Express*, vol. 25, no. 15, p. 17918, 2017.

[129] G. Calafiore *et al.*, “Holographic planar lightwave circuit for on-chip spectroscopy,” *Light Sci. Appl.*, vol. 3, no. 9, 2014.

[130] R. F. Wolffenbuttel, “MEMS-based optical mini- and microspectrometers for the visible and infrared spectral range,” *J. Micromechanics Microengineering*, vol. 15, no. 7, pp. S145–S152, Jul. 2005.

[131] “Mini-spectrometer micro series C12666MA | Hamamatsu Photonics.”

[Online]. Available: https://www.hamamatsu.com/jp/en/product/optical-sensors/spectrometers/mini-spectrometer/C12666MA.html?nfxsid=Cj0KCQjw2ou2BhCCARIsANAwM2FgffhNjRdJ9IZpBXfkrzoDmouhOwumfw30x0gtdmX3shb5rZlIkkQaAkuOEALw_wcB&gad_source=1&gbraid=0AAAAADsz0KeSdW8HxlTWz8z1ZtcfEh9x. [Accessed: 19-Aug-2024].

[132] S. Xie, Y. Meng, J. Bland-Hawthorn, S. Veilleux, and M. Dagenais, “Silicon Nitride/Silicon Dioxide Echelle Grating Spectrometer for Operation Near 1.55 μm,” *IEEE Photonics J.*, vol. 10, no. 6, pp. 1–7, Dec. 2018.

[133] K. Ma, K. Chen, N. Zhu, L. Liu, and S. He, “High-resolution compact on-chip spectrometer based on an echelle grating with densely packed waveguide array,” *IEEE Photonics J.*, vol. 11, no. 1, pp. 1–7, 2019.

[134] Jian-Jun He, B. Lamontagne, A. Delage, L. Erickson, M. Davies, and E. S. Koteles, “Monolithic integrated wavelength demultiplexer based on a waveguide Rowland circle grating in InGaAsP/lnP,” *J. Light. Technol.*, vol. 16, no. 4, pp. 631–638, Apr. 1998.

[135] A. Y. Zhu *et al.*, “Ultra-compact visible chiral spectrometer with meta-lenses,” *APL Photonics*, vol. 2, no. 3, Mar. 2017.

[136] C. Yang, K. Shi, P. Edwards, and Z. Liu, “Demonstration of a PDMS based hybrid grating and Fresnel lens (G-Fresnel) device,” *Opt. Express*, vol. 18, no. 23, p. 23529, Nov. 2010.

[137] J. Brouckaert, W. Bogaerts, S. Selvaraja, P. Dumon, R. Baets, and D. Van

Thourhout, “Planar Concave Grating Demultiplexer With High Reflective Bragg Reflector Facets,” *IEEE Photonics Technol. Lett.*, vol. 20, no. 4, pp. 309–311, Feb. 2008.

[138] B. Momeni, M. Askari, E. Shah Hosseini, A. Atabaki, and A. Adibi, “An on-chip silicon grating spectrometer using a photonic crystal reflector,” *J. Opt.*, vol. 12, no. 3, p. 035501, Mar. 2010.

[139] D. S. Goldman, P. L. White, and N. C. Anheier, “Miniaturized spectrometer employing planar waveguides and grating couplers for chemical analysis,” *Appl. Opt.*, vol. 29, no. 31, p. 4583, Nov. 1990.

[140] “Arrayed waveguide grating.” [Online]. Available: https://en.wikipedia.org/wiki/Arrayed_waveguide_grating.

[141] P. Gatkine *et al.*, “Development of high-resolution arrayed waveguide grating spectrometers for astronomical applications: first results,” in *SPIE Astronomical Telescopes + Instrumentation, 2016, Edinburgh, United Kingdom*, 2016, vol. 9912, no. July 2016, p. 991271.

[142] P. Munoz, D. Pastor, and J. Capmany, “Modeling and Design of Arrayed Waveguide Gratings,” *J. Light. Technol.*, vol. 20, no. 4, pp. 661–674, 2002.

[143] A. Stoll, Z. Zhang, R. Haynes, and M. Roth, “High-Resolution Arrayed-Waveguide-Gratings in Astronomy: Design and Fabrication Challenges,” *Photonics*, vol. 4, no. 2, p. 30, Apr. 2017.

[144] J. Zou *et al.*, “Silicon-Based Arrayed waveguide gratings for WDM and spectroscopic analysis applications,” *Opt. Laser Technol.*, vol. 147, p. 107656,

Mar. 2022.

[145] A. Stoll, K. Madhav, and M. Roth, "Performance limits of astronomical arrayed waveguide gratings on a silica platform," *Opt. Express*, vol. 28, no. 26, p. 39354, Dec. 2020.

[146] C. Sun *et al.*, "Broadband and High-Resolution Integrated Spectrometer Based on a Tunable FSR-Free Optical Filter Array," *ACS Photonics*, vol. 9, no. 9, pp. 2973–2980, Sep. 2022.

[147] A. Li and W. Bogaerts, "Experimental demonstration of a single silicon ring resonator with an ultra-wide FSR and tuning range," *Opt. Lett.*, vol. 42, no. 23, p. 4986, Dec. 2017.

[148] Z. Shi, L. Fang, and C. Zhou, "Dispersive element based on grating and tunable Fabry–Perot filter in miniature spectrometer," *Appl. Opt.*, vol. 53, no. 1, p. 76, Jan. 2014.

[149] X. Gan, N. Pervez, I. Kymissis, F. Hatami, and D. Englund, "A high-resolution spectrometer based on a compact planar two dimensional photonic crystal cavity array," *Appl. Phys. Lett.*, vol. 100, no. 23, Jun. 2012.

[150] A. L. Glebov, O. Mokhun, A. Rapaport, S. Vergnole, V. Smirnov, and L. B. Glebov, "Volume Bragg gratings as ultra-narrow and multiband optical filters," 2012, p. 84280C.

[151] Y. Zhao *et al.*, "Tailoring the spectral response of liquid waveguide diagnostic platforms," *J. Biophotonics*, vol. 5, no. 8–9, pp. 703–711, Aug. 2012.

[152] H. Zhang, X. L. Wang, J. I. Soos, and J. A. Crisp, "Design of a miniature solid

state NIR spectrometer," 1995, p. 376.

[153] N. Gat, "Imaging spectroscopy using tunable filters: A review," in *SPIE Aerosense*, 2000, pp. 50–64.

[154] S. Zheng *et al.*, "A Single-Chip Integrated Spectrometer via Tunable Microring Resonator Array," *IEEE Photonics J.*, vol. 11, no. 5, pp. 1–9, Oct. 2019.

[155] J. P. Carmo, R. P. Rocha, M. Bartek, G. de Graaf, R. F. Wolffenbuttel, and J. H. Correia, "A review of visible-range Fabry–Perot microspectrometers in silicon for the industry," *Opt. Laser Technol.*, vol. 44, no. 7, pp. 2312–2320, Oct. 2012.

[156] O. Manzardo, H. P. Herzig, C. R. Marxer, and N. F. de Rooij, "Miniaturized time-scanning Fourier transform spectrometer based on silicon technology," *Opt. Lett.*, vol. 24, no. 23, pp. 1705–1707, 1999.

[157] D. Bruneau, "Mach–Zehnder interferometer as a spectral analyzer for molecular Doppler wind lidar," *Appl. Opt.*, vol. 40, no. 3, pp. 391–399, Jan. 2001.

[158] A. V. Velasco *et al.*, "High-resolution Fourier-transform spectrometer chip with microphotonic silicon spiral waveguides," *Opt. Lett.*, vol. 38, no. 5, p. 706, Mar. 2013.

[159] M. Florjańczyk, P. Cheben, S. Janz, A. Scott, B. Solheim, and D.-X. Xu, "Multiaperture planar waveguide spectrometer formed by arrayed Mach-Zehnder interferometers.," *Opt. Express*, vol. 15, no. 26, pp. 18176–89, Dec. 2007.

[160] H. Podmore *et al.*, "Demonstration of a compressive-sensing Fourier-transform on-chip spectrometer.," *Opt. Lett.*, vol. 42, no. 7, pp. 1440–1443, Apr. 2017.

[161] M. C. M. M. Souza, A. Grieco, N. C. Frateschi, and Y. Fainman, "Fourier transform spectrometer on silicon with thermo-optic non-linearity and dispersion correction.," *Nat. Commun.*, vol. 9, no. 1, p. 665, Feb. 2018.

[162] S. N. Zheng *et al.*, "Microring resonator-assisted Fourier transform spectrometer with enhanced resolution and large bandwidth in single chip solution.," *Nat. Commun.*, vol. 10, no. 1, p. 2349, May 2019.

[163] K. Wang, J. Li, D. F. Lu, and Z. M. Qi, "Algorithmic Enhancement of Spectral Resolution of a Lithium Niobate (LiNbO3) Waveguide-Based Miniature Fourier Transform Spectrometer," *Appl. Spectrosc.*, vol. 70, no. 10, pp. 1685–1691, Jul. 2016.

[164] X. Wang *et al.*, "Fast and low energy-consumption integrated Fourier-transform spectrometer based on thin-film lithium niobate," *Nanophotonics*, no. 5, Aug. 2024.

[165] D. M. Kita *et al.*, "High-performance and scalable on-chip digital Fourier transform spectroscopy.," *Nat. Commun.*, vol. 9, no. 1, p. 4405, Oct. 2018.

[166] E. Le Coarer *et al.*, "Wavelength-scale stationary-wave integrated Fourier-transform spectrometry," *Nat. Photonics*, vol. 1, pp. 473–478, 2007.

[167] J. Loridat *et al.*, "All Integrated Lithium Niobate Standing Wave Fourier Transform Electro-Optic Spectrometer," *J. Light. Technol.*, vol. 36, no. 20, pp. 4900–4907, Oct. 2018.

[168] X. Chen, P. Huang, N. Wang, Y. Zhu, and J. Zhang, "Dual Tunable MZIs Stationary-Wave Integrated Fourier Transform Spectrum Detection," *Sensors*,

vol. 21, no. 7, p. 2352, Mar. 2021.

[169] B. Redding and H. Cao, “Using a multimode fiber as a high-resolution, low-loss spectrometer,” *Opt. Lett.*, vol. 37, no. 16, pp. 3384–3386, 2012.

[170] D. L. Donoho, “Compressed sensing,” *IEEE Trans. Inf. Theory*, vol. 52, no. 4, pp. 1289–1306, 2006.

[171] Q. Hang, B. Ung, I. Syed, N. Guo, and M. Skorobogatiy, “Photonic bandgap fiber bundle spectrometer,” *Appl. Opt.*, vol. 49, no. 25, p. 4791, Sep. 2010.

[172] B. Redding, S. M. Popoff, and H. Cao, “All-fiber spectrometer based on speckle pattern reconstruction,” *Opt. Express*, vol. 21, no. 5, p. 6584, 2013.

[173] Z. Xu, Z. Wang, M. E. Sullivan, D. J. Brady, S. H. Foulger, and A. Adibi, “Multimodal multiplex spectroscopy using photonic crystals,” *Opt. Express*, vol. 11, no. 18, pp. 2126–2133, 2003.

[174] S. F. Liew, B. Redding, M. A. Choma, H. D. Tagare, and H. Cao, “Broadband multimode fiber spectrometer,” *Opt. Lett.*, vol. 41, no. 9, pp. 162–163, 2016.

[175] Q. Cen, S. Pian, X. Liu, Y. Tang, X. He, and Y. Ma, “Microtaper leaky-mode spectrometer with picometer resolution,” *eLight*, vol. 3, no. 1, 2023.

[176] N. H. Wan, F. Meng, T. Schroder, R. J. Shiue, E. H. Chen, and D. Englund, “High-resolution optical spectroscopy using multimode interference in a compact tapered fibre,” *Nat. Commun.*, vol. 6, pp. 1–6, 2015.

[177] G. D. Bruce, L. O’Donnell, M. Chen, and K. Dholakia, “Overcoming the speckle correlation limit to achieve a fiber wavemeter with attometer resolution,” *Opt. Lett.*, vol. 44, no. 6, pp. 1367–1370, 2019.

[178] M. Piels and D. Zibar, “Compact silicon multimode waveguide spectrometer with enhanced bandwidth,” *Sci. Rep.*, vol. 7, pp. 1–7, 2017.

[179] B. Redding, S. Fatt Liew, Y. Bromberg, R. Sarma, and H. Cao, “Evanescently coupled multimode spiral spectrometer,” *Optica*, vol. 3, no. 9, p. 956, 2016.

[180] T. Yang *et al.*, “Miniature spectrometer based on diffraction in a dispersive hole array,” *Opt. Lett.*, vol. 40, no. 13, pp. 3217–3220, 2015.

[181] C. Yao, K. Xu, W. Zhang, M. Chen, Q. Cheng, and R. Penty, “Integrated reconstructive spectrometer with programmable photonic circuits,” *Nat. Commun.*, vol. 14, no. 1, pp. 1–10, 2023.

[182] Z. Zhang, Y. Li, Y. Wang, Z. Yu, X. Sun, and H. K. Tsang, “Compact High Resolution Speckle Spectrometer by Using Linear Coherent Integrated Network on Silicon Nitride Platform at 776 nm,” *Laser Photon. Rev.*, vol. 15, no. 11, p. 210039, 2021.

[183] Z. Yang *et al.*, “Single-nanowire spectrometers.,” *Science*, vol. 365, no. 6457, pp. 1017–1020, Sep. 2019.

[184] H. H. Yoon *et al.*, “Miniaturized spectrometers with a tunable van der Waals junction,” *Science (80-.).*, vol. 378, no. 6617, pp. 296–299, 2022.

[185] Y. Liu *et al.*, “Ultra-sensitive and plasmon-tunable graphene photodetectors for micro-spectrometry,” *Nanoscale*, vol. 10, no. 42, pp. 20013–20019, 2018.

[186] S. Xing *et al.*, “Miniaturized VIS-NIR Spectrometers Based on Narrowband and Tunable Transmission Cavity Organic Photodetectors with Ultrahigh Specific Detectivity above 1014 Jones,” *Adv. Mater.*, vol. 33, no. 44, p. 2102967, 2021.

[187] J. Kulakowski and B. D’Humières, “Miniature, micro and chip-size spectrometers: technologies, market trends and customers’ needs,” 2020.

[188] A. J. Das, A. Wahi, I. Kothari, and R. Raskar, “Ultra-portable, wireless smartphone spectrometer for rapid, non-destructive testing of fruit ripeness,” *Sci. Rep.*, vol. 6, no. 1, p. 32504, Sep. 2016.

[189] F. Ahmed, “Smartphone Spectroscopy Takes the Lab to the People,” *Photonics Spectra*, Sep-2018.

[190] “Real-Time, Non-Invasive Biomarker Sensing on the Wrist,” 2021.

[191] I. Michael, “Miniature and durable spectrometer for wearable applications,” *Spectroscopy europe world*, Dec-2022.

[192] M. S. Marley and T. D. Robinson, “On the Cool Side: Modeling the Atmospheres of Brown Dwarfs and Giant Planets,” *Annu. Rev. Astron. Astrophys.*, vol. 53, no. 1, pp. 279–323, Aug. 2015.

[193] M. Moresco, R. Jimenez, A. Cimatti, and L. Pozzetti, “Constraining the expansion rate of the Universe using low-redshift ellipticals as cosmic chronometers,” *J. Cosmol. Astropart. Phys.*, vol. 2011, no. 03, pp. 045–045, Mar. 2011.

[194] M. G. Hauser and E. Dwek, “The Cosmic Infrared Background: Measurements and Implications,” *Annu. Rev. Astron. Astrophys.*, vol. 39, no. 1, pp. 249–307, Sep. 2001.

[195] M. Mayor, C. Lovis, and N. C. Santos, “Doppler spectroscopy as a path to the detection of Earth-like planets,” *Nature*, vol. 513, no. 7518, pp. 328–335, Sep.

2014.

[196] A. Aghamousa *et al.*, “The DESI Experiment Part I: Science,Targeting, and Survey Design,” Oct. 2016.

[197] K. Bundy *et al.*, “The Keck-FOBOS spectroscopic facility: conceptual design,” in *Ground-based and Airborne Instrumentation for Astronomy VIII*, 2020, p. 242.

[198] David J. Schlegel *et al.*, “The MegaMapper: A Stage-5 Spectroscopic Instrument Concept for the Study of Inflation and Dark Energy,” *ArXiv*, 2022.

[199] N. Jovanovic *et al.*, “2023 Astrophotonics Roadmap: pathways to realizing multi-functional integrated astrophotonic instruments,” *J. Phys. Photonics*, vol. 5, no. 4, p. 042501, Oct. 2023.

[200] N. Cvetojevic *et al.*, “First starlight spectrum captured using an integrated photonic micro-spectrograph,” *Astron. Astrophys.*, vol. 544, p. L1, Aug. 2012.

[201] N. Cvetojevic *et al.*, “Modal noise in an integrated photonic lantern fed diffraction-limited spectrograph,” *Opt. Express*, vol. 25, no. 21, p. 25546, 2017.

[202] K. Madhav *et al.*, “PAWS and POCO: NIR Astrophotonic Instruments for Astronomy,” *Astron. Nachrichten*, vol. 344, no. 8–9, Oct. 2023.

[203] N. Cvetojevic, J. S. Lawrence, S. C. Ellis, J. Bland-Hawthorn, R. Haynes, and A. Horton, “Characterization and on-sky demonstration of an integrated photonic spectrograph for astronomy,” *Opt. Express*, vol. 17, no. 21, p. 18643, Oct. 2009.

[204] P. M. Vreeswijk *et al.*, “Low-resolution VLT spectroscopy of GRBs 991216,

011211 and 021211," *Astron. Astrophys.*, vol. 447, no. 1, pp. 145–156, Feb. 2006.

[205] R. Salvaterra, "High redshift Gamma-Ray Bursts," *J. High Energy Astrophys.*, vol. 7, pp. 35–43, Sep. 2015.

[206] V. Gopinath *et al.*, "Arrayed waveguide grating based photonic spectrograph for the astronomical J band," in *Ground-based and Airborne Instrumentation for Astronomy X*, 2024, p. 396.

[207] R. J. Harris and J. R. Allington-Smith, "Applications of Integrated Photonic Spectrographs in astronomy," *Mon. Not. R. Astron. Soc.*, vol. 428, no. 4, pp. 3139–3150, Feb. 2013.

[208] G. J. Hill *et al.*, "VIRUS: status and performance of the massively replicated fiber integral field spectrograph for the upgraded Hobby-Eberly Telescope," in *Ground-based and Airborne Instrumentation for Astronomy VII*, 2018, p. 56.

[209] T. Hu, X. Zhang, M. Zhang, and X. Yan, "A high-resolution miniaturized ultraviolet spectrometer based on arrayed waveguide grating and microring cascade structures," *Opt. Commun.*, vol. 482, p. 126591, Mar. 2021.

[210] J. Lawrence, J. Bland-Hawthorn, N. Cvetojevic, R. Haynes, and N. Jovanovic, "Miniature astronomical spectrographs using arrayed-waveguide gratings: capabilities and limitations," in *SPIE Astronomical Telescopes + Instrumentation*, 2010, p. 77394I.

[211] S. G. Leon-Saval, T. A. Birks, J. Bland-Hawthorn, and M. Englund, "Multimode fiber devices with single-mode performance," *Opt. Lett.*, vol. 30, no. 19, p. 2545,

Oct. 2005.

[212] N. Jovanovic *et al.*, “Integrated photonic building blocks for next-generation astronomical instrumentation I: the multimode waveguide,” *Opt. Express*, vol. 20, no. 15, p. 17029, Jul. 2012.

[213] S. G. Leon-Saval, A. Argyros, and J. Bland-Hawthorn, “Photonic lanterns: a study of light propagation in multimode to single-mode converters,” *Opt. Express*, vol. 18, no. 8, p. 8430, Apr. 2010.

[214] J. Bland-Hawthorn, M. Englund, and G. Edvell, “New approach to atmospheric OH suppression using an aperiodic fibre Bragg grating,” *Opt. Express*, vol. 12, no. 24, p. 5902, 2004.

[215] J. Bland-Hawthorn *et al.*, “A complex multi-notch astronomical filter to suppress the bright infrared sky,” *Nat. Commun.*, vol. 2, no. 1, p. 581, Dec. 2011.

[216] T. A. Birks, B. J. Mangan, A. Díez, J. L. Cruz, and D. F. Murphy, “‘Photonic lantern’ spectral filters in multi-core fibre,” *Opt. Express*, vol. 20, no. 13, p. 13996, 2012.

[217] M. Demartino *et al.*, “An astrophotonics platform for Lick Observatory: testing Adaptive Mode Extraction with photonic lanterns,” in *Advances in Optical and Mechanical Technologies for Telescopes and Instrumentation V*, 2022, p. 114.

[218] J. Bland-Hawthorn *et al.*, “PIMMS: photonic integrated multimode microspectrograph,” in *Proc. SPIE*, 2010, vol. 7735, p. 77350N.

[219] G. Douglass, F. Dreisow, S. Gross, and M. J. Withford, “Femtosecond laser written arrayed waveguide gratings with integrated photonic lanterns,” *Opt.*

Express, vol. 26, no. 2, p. 1497, 2018.

[220] P. Gatkine, S. Veilleux, and M. Dagenais, “Astrophotonic Spectrographs,” *Appl. Sci.*, vol. 9, no. 2, p. 290, Jan. 2019.

[221] A. Endo *et al.*, “First light demonstration of the integrated superconducting spectrometer,” *Nat. Astron.*, vol. 3, no. 11, pp. 989–996, Aug. 2019.

[222] A. Taniguchi *et al.*, “DESHIMA 2.0: Development of an Integrated Superconducting Spectrometer for Science-Grade Astronomical Observations,” *J. Low Temp. Phys.*, vol. 209, no. 3–4, pp. 278–286, Nov. 2022.

[223] J. Tepper *et al.*, “Ultrafast laser inscription in ZBLAN integrated optics chips for mid-IR beam combination in astronomical interferometry,” *Opt. Express*, vol. 25, no. 17, p. 20642, Aug. 2017.

[224] B. R. M. Norris, J. Wei, C. H. Betters, A. Wong, and S. G. Leon-Saval, “An all-photonic focal-plane wavefront sensor,” *Nat. Commun.*, vol. 11, no. 1, p. 5335, Oct. 2020.

[225] H. Ahn, H. Song, D.-M. Shin, K. Kim, and J. Choi, “Emerging optical spectroscopy techniques for biomedical applications—A brief review of recent progress,” *Appl. Spectrosc. Rev.*, vol. 53, no. 2–4, pp. 264–278, Apr. 2018.

[226] D. R. Parachalil *et al.*, “Analysis of bodily fluids using vibrational spectroscopy: a direct comparison of Raman scattering and infrared absorption techniques for the case of glucose in blood serum,” *Analyst*, vol. 144, no. 10, pp. 3334–3346, 2019.

[227] K. B. Beć, J. Grabska, H. W. Siesler, and C. W. Huck, “Handheld near-infrared

spectrometers: Where are we heading?," *NIR news*, vol. 31, no. 3–4, pp. 28–35, Jun. 2020.

[228] S. Yao, C. Ball, G. Miyagusuku-Cruzado, M. M. Giusti, D. P. Aykas, and L. E. Rodriguez-Saona, "A novel handheld FT-NIR spectroscopic approach for real-time screening of major cannabinoids content in hemp," *Talanta*, vol. 247, p. 123559, Sep. 2022.

[229] E. Samiei, M. Tabrizian, and M. Hoorfar, "A review of digital microfluidics as portable platforms for lab-on a-chip applications," *Lab Chip*, vol. 16, no. 13, pp. 2376–2396, 2016.

[230] Á. Ríos, M. Zougagh, and M. Avila, "Miniaturization through lab-on-a-chip: Utopia or reality for routine laboratories? A review," *Anal. Chim. Acta*, vol. 740, pp. 1–11, Aug. 2012.

[231] H. Bi, A. C. Fernandes, S. Cardoso, and P. Freitas, "Interference-blind microfluidic sensor for ascorbic acid determination by UV/vis spectroscopy," *Sensors Actuators B Chem.*, vol. 224, pp. 668–675, Mar. 2016.

[232] D. De Coster *et al.*, "Free-Form Optics Enhanced Confocal Raman Spectroscopy for Optofluidic Lab-on-Chips," *IEEE J. Sel. Top. Quantum Electron.*, vol. 21, no. 4, pp. 79–86, Jul. 2015.

[233] H. Ryan, A. Smith, and M. Utz, "Structural shimming for high-resolution nuclear magnetic resonance spectroscopy in lab-on-a-chip devices," *Lab Chip*, vol. 14, no. 10, pp. 1678–1685, 2014.

[234] Y. Uludag *et al.*, "An integrated lab-on-a-chip-based electrochemical biosensor

for rapid and sensitive detection of cancer biomarkers," *Anal. Bioanal. Chem.*, vol. 408, no. 27, pp. 7775–7783, Nov. 2016.

[235] C. F. Bohren and D. R. Huffman, *Absorption and scattering of light by small particles*. John Wiley & Sons, 2008.

[236] I. M. White, J. Gohring, and X. Fan, "SERS-based detection in an optofluidic ring resonator platform," *Opt. Express*, vol. 15, no. 25, p. 17433, 2007.

[237] A. Lamberti *et al.*, "Ultrasensitive Ag-coated TiO 2 nanotube arrays for flexible SERS-based optofluidic devices," *J. Mater. Chem. C*, vol. 3, no. 26, pp. 6868–6875, 2015.

[238] J. J. S. Rickard, V. Di-Pietro, D. J. Smith, D. J. Davies, A. Belli, and P. G. Oppenheimer, "Rapid optofluidic detection of biomarkers for traumatic brain injury via surface-enhanced Raman spectroscopy," *Nat. Biomed. Eng.*, vol. 4, no. 6, pp. 610–623, Feb. 2020.

[239] I. Rodríguez-Ruiz, T. N. Ackermann, X. Muñoz-Berbel, and A. Llobera, "Photonic Lab-on-a-Chip: Integration of Optical Spectroscopy in Microfluidic Systems," *Anal. Chem.*, vol. 88, no. 13, pp. 6630–6637, Jul. 2016.

[240] G. Persichetti, I. A. Grimaldi, G. Testa, and R. Bernini, "Multifunctional optofluidic lab-on-chip platform for Raman and fluorescence spectroscopic microfluidic analysis," *Lab Chip*, vol. 17, no. 15, pp. 2631–2639, 2017.

[241] J. Kim *et al.*, "The Optofluidic Light Cage – On-Chip Integrated Spectroscopy Using an Antiresonance Hollow Core Waveguide," *Anal. Chem.*, vol. 93, no. 2, pp. 752–760, Jan. 2021.

[242] M. Brückner, K. Becker, J. Popp, and T. Frosch, "Fiber array based hyperspectral Raman imaging for chemical selective analysis of malaria-infected red blood cells," *Anal. Chim. Acta*, vol. 894, pp. 76–84, Sep. 2015.

[243] H. A. Bechtel, E. A. Muller, R. L. Olmon, M. C. Martin, and M. B. Raschke, "Ultrabroadband infrared nanospectroscopic imaging," *Proc. Natl. Acad. Sci.*, vol. 111, no. 20, pp. 7191–7196, May 2014.

[244] K. D. Heylman *et al.*, "Optical microresonators as single-particle absorption spectrometers," *Nat. Photonics*, vol. 10, no. 12, pp. 788–795, Dec. 2016.

[245] R. Singh, D. Ma, L. Kimerling, A. M. Agarwal, and B. W. Anthony, "Chemical Characterization of Aerosol Particles Using On-Chip Photonic Cavity Enhanced Spectroscopy," *ACS Sensors*, vol. 4, no. 3, pp. 571–577, Mar. 2019.

[246] N. Maccaferri, G. Barbillon, A. N. Koya, G. Lu, G. P. Acuna, and D. Garoli, "Recent advances in plasmonic nanocavities for single-molecule spectroscopy," *Nanoscale Adv.*, vol. 3, no. 3, pp. 633–642, 2021.

[247] R. B. Jaculbia *et al.*, "Single-molecule resonance Raman effect in a plasmonic nanocavity," *Nat. Nanotechnol.*, vol. 15, no. 2, pp. 105–110, Feb. 2020.

[248] C.-Y. Li *et al.*, "Real-time detection of single-molecule reaction by plasmon-enhanced spectroscopy," *Sci. Adv.*, vol. 6, no. 24, Jun. 2020.

[249] A. Barulin, J.-B. Claude, S. Patra, N. Bonod, and J. Wenger, "Deep Ultraviolet Plasmonic Enhancement of Single Protein Autofluorescence in Zero-Mode Waveguides," *Nano Lett.*, vol. 19, no. 10, pp. 7434–7442, Oct. 2019.

[250] K. Schär, R. Haus, J. Heland, and A. Haak, "Measurements of Atmospheric

Trace Gases by Emission and Absorption Spectroscopy with FTIR," *Berichte der Bunsengesellschaft für Phys. Chemie*, vol. 99, no. 3, pp. 405–411, Mar. 1995.

[251] M. De Biasio, T. Arnold, and R. Leitner, "UAV based Multi-spectral Imaging System for Environmental Monitoring," *teme*, vol. 78, no. 11, pp. 503–507, Nov. 2011.

[252] F. J. Fortes, J. Moros, P. Lucena, L. M. Cabalín, and J. J. Laserna, "Laser-Induced Breakdown Spectroscopy," *Anal. Chem.*, vol. 85, no. 2, pp. 640–669, Jan. 2013.

[253] X. Chu and G. C. Papen, "Resonance Fluorescence Lidar for Measurements of the Middle and Upper Atmosphere," in *Laser Remtoe Sensing*, 1st ed., CRC Press, 2005.

[254] I. E. Gordon *et al.*, "The HITRAN2020 molecular spectroscopic database," *J. Quant. Spectrosc. Radiat. Transf.*, vol. 277, p. 107949, Jan. 2022.

[255] A. Hänsel and M. J. R. Heck, "Opportunities for photonic integrated circuits in optical gas sensors," *J. Phys. Photonics*, vol. 2, no. 1, p. 012002, Jan. 2020.

[256] A. Hänsel and M. J. R. Heck, "Feasibility of Telecom-Wavelength Photonic Integrated Circuits for Gas Sensors," *Sensors*, vol. 18, no. 9, p. 2870, Aug. 2018.

[257] N. Picqué and T. W. Hänsch, "Frequency comb spectroscopy," *Nat. Photonics*, vol. 13, no. 3, pp. 146–157, Mar. 2019.

[258] M. J. Thorpe, D. Balslev-Clausen, M. S. Kirchner, and J. Ye, "Cavity-enhanced optical frequency comb spectroscopy: application to human breath analysis,"

Opt. Express, vol. 16, no. 4, p. 2387, 2008.

[259] L. Nielsen, E. A. J. M. Bente, E. den Haan, and M. J. R. Heck, "Theoretical and Experimental Investigation of Unidirectionality in an Integrated Semiconductor Ring Mode-Locked Laser With Two Saturable Absorbers," *IEEE J. Quantum Electron.*, vol. 54, no. 5, pp. 1–10, Oct. 2018.

[260] S. Alberti, A. Datta, and J. Jágerská, "Integrated Nanophotonic Waveguide-Based Devices for IR and Raman Gas Spectroscopy," *Sensors*, vol. 21, no. 21, p. 7224, Oct. 2021.

[261] P. Su *et al.*, "Monolithic on-chip mid-IR methane gas sensor with waveguide-integrated detector," *Appl. Phys. Lett.*, vol. 114, no. 5, Feb. 2019.

[262] D. S. Baer, J. B. Paul, M. Gupta, and A. O'Keefe, "Sensitive absorption measurements in the near-infrared region using off-axis integrated-cavity-output spectroscopy," *Appl. Phys. B Lasers Opt.*, vol. 75, no. 2–3, pp. 261–265, Sep. 2002.

[263] T. Hu *et al.*, "Silicon photonic platforms for mid-infrared applications [Invited]," *Photonics Res.*, vol. 5, no. 5, p. 417, Oct. 2017.

[264] B. Wu, J. F. Hulbert, E. J. Lunt, K. Hurd, A. R. Hawkins, and H. Schmidt, "Slow light on a chip via atomic quantum state control," *Nat. Photonics*, vol. 4, no. 11, pp. 776–779, Nov. 2010.

[265] D. Mengu, A. Tabassum, M. Jarrahi, and A. Ozcan, "Snapshot multispectral imaging using a diffractive optical network," *Light Sci. Appl.*, vol. 12, no. 1, p. 86, Apr. 2023.

[266] S. Mansha *et al.*, “High resolution multispectral spatial light modulators based on tunable Fabry-Perot nanocavities,” *Light Sci. Appl.*, vol. 11, no. 1, p. 141, May 2022.

[267] Z. Wang *et al.*, “Single-shot on-chip spectral sensors based on photonic crystal slabs,” *Nat. Commun.*, vol. 10, no. 1, p. 1020, Mar. 2019.

[268] I. Zegaar, A. Hocini, D. Khedrouche, H. Ben salah, and H. Bahri, “Plasmonic stop-band filter based on an MIM waveguide coupled with cavity resonators,” *J. Phys. Conf. Ser.*, vol. 2240, no. 1, p. 012025, Mar. 2022.

[269] B. H. Chen *et al.*, “GaN Metalens for Pixel-Level Full-Color Routing at Visible Light,” *Nano Lett.*, vol. 17, no. 10, pp. 6345–6352, Oct. 2017.

[270] G. G. Meena, A. M. Stambaugh, V. Ganjalizadeh, M. A. Stott, A. R. Hawkins, and H. Schmidt, “Ultrasensitive detection of SARS-CoV-2 RNA and antigen using single-molecule optofluidic chip,” *APL Photonics*, vol. 6, no. 6, 2021.

[271] X. L. Zhang, L. Li, J. H. Cui, Y. L. Ju, and Y. Z. Wang, “Single longitudinal mode and continuously tunable frequency Tm,Ho:YLF laser with two solid etalons,” *Laser Phys. Lett.*, vol. 7, no. 3, pp. 194–197, Mar. 2010.

[272] F. Feng *et al.*, “AI-assisted spectrometer based on multi-mode optical fiber speckle patterns,” *Opt. Commun.*, vol. 522, p. 128675, Nov. 2022.

[273] G. Ou and Y. L. Murphey, “Multi-class pattern classification using neural networks,” *Pattern Recognit.*, vol. 40, no. 1, pp. 4–18, Jan. 2007.

[274] A. Krizhevsky, I. Sutskever, and G. E. Hinton, “ImageNet classification with deep convolutional neural networks,” in *Advances in Neural Information*

Processing Systems 25, 2012, pp. 1097–1105.

[275] C. Shorten and T. M. Khoshgoftaar, “A survey on Image Data Augmentation for Deep Learning,” *J. Big Data*, vol. 6, no. 1, p. 60, Dec. 2019.

[276] D. M. Gates, “Spectral distribution of solar radiation at the earth’s surface,” *Science (80-.).*, vol. 151, no. 3710, pp. 523–529, Feb. 1966.

[277] B. Lyot, “Optical apparatus with wide field using interference of polarized light,” in *C. R. Acad. Sci.*, 1933, p. 1593.

[278] A. Geron, *Hands-On Machine Learning with Scikit-Learn, Keras, & TensorFlow*. O’Reilly, 2022.

[279] W. Livingston, L. Wallace, O. R. White, and M. S. Giampapa, “Sun-as-a-Star Spectrum Variations 1974–2006,” *Astrophys. J.*, vol. 657, no. 2, pp. 1137–1149, Mar. 2007.

[280] A. Tritschler, R. Schlichenmaier, and L. R. Bellot Rubio, “Two-dimensional spectroscopy of a sunspot,” *Astron. Astrophys.*, vol. 415, no. 2, pp. 717–729, Feb. 2004.

[281] R. O. Milligan, “Extreme Ultra-Violet Spectroscopy of the Lower Solar Atmosphere During Solar Flares (Invited Review),” *Sol. Phys.*, vol. 290, no. 12, pp. 3399–3423, Dec. 2015.

[282] R. A. Harrison and M. Lyons, “A spectroscopic study of coronal dimming associated with a coronal mass ejection,” *Astron. Astrophys.*, vol. 358, pp. 1097–1108, 2000.

[283] A. Butz, S. Guerlet, O. P. Hasekamp, A. Kuze, and H. Suto, “Using ocean-glint

scattered sunlight as a diagnostic tool for satellite remote sensing of greenhouse gases," *Atmos. Meas. Tech.*, vol. 6, no. 9, pp. 2509–2520, Sep. 2013.

[284] K. Pydzińska and M. Ziółek, "Solar cells sensitized with near-infrared absorbing dye: Problems with sunlight conversion efficiency revealed in ultrafast laser spectroscopy studies," *Dye. Pigment.*, vol. 122, pp. 272–279, Nov. 2015.

[285] "Spectroradiometers," *Apogee Instruments*. [Online]. Available: https://www.apogeeinstruments.com/spectroradiometers/.

[286] "Spectroradiometer," *JETI Technische Instrumente GmbH*. [Online]. Available: https://www.jeti.com/Products/Spectroradiometer/Overview.

[287] M. Meroni *et al.*, "Characterization of fine resolution field spectrometers using solar Fraunhofer lines and atmospheric absorption features," *Appl. Opt.*, vol. 49, no. 15, p. 2858, May 2010.

[288] Liangyun Liu, Yongjiang Zhang, Jihua Wang, and Chunjiang Zhao, "Detecting solar-induced chlorophyll fluorescence from field radiance spectra based on the Fraunhofer line principle," *IEEE Trans. Geosci. Remote Sens.*, vol. 43, no. 4, pp. 827–832, Apr. 2005.

[289] A. J. Bechter, J. Crass, J. Tesch, J. R. Crepp, and E. B. Bechter, "Characterization of Single-mode Fiber Coupling at the Large Binocular Telescope," *Publ. Astron. Soc. Pacific*, vol. 132, no. 1007, p. 015001, Jan. 2020.

[290] J. E. Carranza, B. T. Fisher, G. D. Yoder, and D. W. Hahn, "On-line analysis of ambient air aerosols using laser-induced breakdown spectroscopy," *Spectrochim. Acta Part B At. Spectrosc.*, vol. 56, no. 6, pp. 851–864, Jun. 2001.

[291] R. S. de Jong *et al.*, “4MOST: Project overview and information for the First Call for Proposals,” Mar. 2019.

[292] J. D. Simon *et al.*, “Testing the Nature of Dark Matter with Extremely Large Telescopes,” Mar. 2019.

[293] R. Kupke *et al.*, “ShaneAO: an enhanced adaptive optics and IR imaging system for the Lick Observatory 3-meter telescope,” in *SPIE Astronomical Telescopes + Instrumentation*, 2012, pp. 84473G-84473G–7.

[294] K.-P. Schröder and H. Lüthen, “Astrophotography,” in *Handbook of Practical Astronomy*, Berlin, Heidelberg: Springer Berlin Heidelberg, 2009, pp. 133–173.

[295] H. H. Yoon *et al.*, “Miniaturized spectrometers with a tunable van der Waals junction,” *Science (80-.).*, vol. 378, no. 6617, pp. 296–299, 2022.

[296] B. Redding, S. M. Popoff, Y. Bromberg, M. A. Choma, and H. Cao, “Noise analysis of spectrometers based on speckle pattern reconstruction,” *Appl. Opt.*, vol. 53, no. 3, pp. 410–417, Jan. 2014.

[297] T. Greffe *et al.*, “Characterization of low light performance of a complementary metal-oxide semiconductor sensor for ultraviolet astronomical applications,” *J. Astron. Telesc. Instruments, Syst.*, vol. 8, no. 02, Apr. 2022.

[298] D. W. Shipp, F. Sinjab, and I. Notingher, “Raman spectroscopy: techniques and applications in the life sciences,” *Adv. Opt. Photonics*, vol. 9, no. 2, p. 315, Jun. 2017.

[299] E. M. Obeng, E. C. Dullah, M. K. Danquah, C. Budiman, and C. M. Ongkudon, “FRET spectroscopy—towards effective biomolecular probing,” *Anal. Methods*,

vol. 8, no. 27, pp. 5323–5337, 2016.

[300] L. Hong and K. Sengupta, “Fully Integrated Optical Spectrometer in Visible and Near-IR in CMOS,” *IEEE Trans. Biomed. Circuits Syst.*, vol. 11, no. 6, pp. 1176–1191, Dec. 2017.

[301] M. T. Postek and A. E. Vladár, “Does your SEM really tell the truth? How would you know? Part 4: Charging and its mitigation,” in *Proc. SPIE Int. Soc. Opt. Eng.*, 2015, p. 963605.

[302] V. A. Magnotta and L. Friedman, “Measurement of Signal-to-Noise and Contrast-to-Noise in the fBIRN Multicenter Imaging Study,” *J. Digit. Imaging*, vol. 19, no. 2, pp. 140–147, Jun. 2006.

[303] D. J. Schroeder, *Astronomical Optics*, 2nd ed. Academic Press, 1999.